Tomography of the alpine arc using noise correlations & waveform modelling

Yang Lu

Communauté
UNIVERSITÉ Grenoble Alpes

THÈSE

Pour obtenir le grade de

DOCTEUR DE LA COMMUNAUTÉ UNIVERSITÉ GRENOBLE ALPES

Spécialité : Terre Solide (CETSOL)

Arrêté ministériel : 25 mai 2016

Présentée par

Yang LU

Thèse dirigée par **Anne PAUL**, Directrice de Recherches, CNRS
et codirigée par **Laurent STEHLY**, chercheur, UGA

préparée au sein du **Laboratoire Institut des Sciences de la Terre**
dans **l'École Doctorale Terre, Univers, Environnement**

Tomographie de l'arc alpin à partir de corrélations de bruit & modélisation de la propagation des ondes.

Tomography of the alpine arc using noise correlations & waveform modelling

Thèse soutenue publiquement le **12 février 2019**,
devant le jury composé de :

Madame ANNE PAUL
DIRECTRICE DE RECHERCHE, CNRS DELEGATION ALPES, Directeur de thèse
Monsieur STEPHANE OPERTO
DIRECTEUR DE RECHERCHE, CNRS DELEGATION COTE D'AZUR, Rapporteur
Monsieur FREDERIK TILMANN
PROFESSEUR, UNIVERSITE LIBRE DE BERLIN, Rapporteur
Monsieur ERIC DEBAYLE
DIRECTEUR DE RECHERCHE, CNRS DELEGATION RHONE AUVERGNE, Examinateur
Monsieur LIANG ZHAO
PROFESSEUR, ACADEMIE CHINOISE DES SCIENCES - PEKIN, Examinateur
Monsieur MICHEL CAMPILLO
PROFESSEUR, UNIVERSITE GRENOBLE ALPES, Président

Remerciements

First and foremost, I would like to express my sincere gratitude to my two advisors Anne Paul and Laurent Stehly for their invaluable support, never-ending patience and encouragement. I appreciate their suggestions, comments, and corrections on every aspect of this study. The freedom they give me makes working with them is such a great pleasure.

My sincere gratitude also goes to the committee members, Stéphane Operto, Frederik Tilmann, Michel Campillo, Eric Debayle, and Liang Zhao, for their careful reading of the thesis and valuable suggestions.

I also deeply appreciate Romain Brossier, Lapo Boschi and Thomas Bodin for their great help during our research collaborations. Romain Brossier taught me how to perform seismic waveform simulation and inversion. Lapo Boschi shared his expertise and code for the 2-D traveltime inversion. Thomas Bodin gave me great advice on the probabilistic inversion of surface wave dispersion. My appreciation also goes to the Seiscope consortium for providing the full waveform inversion code.

I also very much appreciate the AlpArray-FR project, not only allowing me to access the data of the AlpArray(Z3) network, but also providing me the funding for communication and conferences.

I also would like to thank my colleagues at ISTerre who gave me much help : Helle Pedersen, Pierre Boué, Ludovic Moreau, Stephane Guillot, Ludovic Metivier, Jean Virieux, Olivier Coutant, Anne Barnoud, Weiguang He, Irnaka Theodosius Marwan.

My deepest thanks go to my partner Qingyu Wang for her unfailing love and support. She is my constant source of strength that helps me to keep things in perspective.

Résumé

Le but de cette thèse a été de construire un modèle haute résolution de la vitesse des ondes S au sein la croûte et du manteau supérieur de l'arc alpin et de l'Europe, à partir de corrélations de bruit. Dans ce cadre, nous avons construit plusieurs modèles tomographiques à partir d'un jeu de donnée composé de quatre années de bruit ambiant enregistré par 1293 stations réparties à travers l'Europe. Nous avons tout d'abord réalisé une tomographie par corrélation de bruit "classique". Des mesures de vitesse de groupe des ondes de Rayleigh entre 5 et 150s de période ont été inversées pour construire des cartes de vitesse de groupe. Elles ont été inversées avec une approche bayésienne afin d'établir un modèle probabiliste de la vitesse des onde S et d'évaluer la probabilité d'avoir une interface en chaque point du modèle. Ceci a permis d'établir un modèle tomographique haute résolution de l'ensemble de l'Europe en bon accord avec des études antérieures ciblées sur des zones spécifiques.

La forte densité de station au niveau de l'arc alpin nous a permis d'établir des cartes de vitesse de phase avec la méthode Eikonal entre 7 et 25s de période. Celles-ci sont en accord avec les cartes de vitesse de groupe précédemment établies. De plus nous avons pu avec cette méthode étudier l'anisotropie de la croûte à l'échelle des Alpes.

Nous avons continué à affiner notre modèle de la lithosphère alpine en réalisant une tomographie basée sur l'équation d'onde ("wave equation tomography", WET) s'appuyant sur des simulations numériques de la propagation des ondes elastiques en 3D. Nous avons ainsi itérativement amélioré le modèle en minimisant la différence de vitesse de phase des ondes de Rayleigh mesurée sur des corrélations observées et simulées numériquement entre 10 et 55s de période. Le modèle final a été obtenu après 15 itérations avec une réduction de la fonction coût de $\sim$65%. Au sein de la croûte et à l'interface croûte/manteau, ce modèle présente de nouvelles structures et des contrastes de vitesse plus importants. Ceci illustre que cette approche permet d'améliorer significativement les modèles tomographiques obtenus par corrélations de bruit.

Abstract

The primary goal of the thesis is to build high-resolution shear-wave velocity models of the Alpine crust and uppermost mantle using ambient noise based tomography. In this framework, we performed a series of tomographic applications using a large cross-correlation dataset computed from 4 years of noise recorded at 1293 broadband seismic stations across Europe.

We first applied a 'classical' ambient noise group velocity tomography. Rayleigh wave group velocity measurements in the period band 5-150 s were inverted to construct group velocity maps. With a Bayesian 1-D depth inversion approach, we determined both the shear-wave velocity and probability of interfaces at each cell of the model. This has allowed to finally establish a high-resolution model of the European crust and uppermost mantle in good agreement with previous localized geophysical studies.

Taking advantage of the dense seismic array in the Alpine region, we performed ambient noise Eikonal tomography using Rayleigh wave phase velocity measurements in the period band 7-25 s. With this method, we were able to study the anisotropy of the Alpine crust.

We refined the shear wave velocity model of the Alpine crust and uppermost mantle using wave-equation tomography (WET) based on the numerical simulation of 3-D elastic wave propagation. We iteratively improved the initial model by minimizing the phase traveltime differences between the observed and synthetic Rayleigh waves in the period band 10-55 s. We obtained the final model after 15 iterations with a reduction of total misfit $\sim$65%. At crustal and Moho depths, the final model displays several new features and much stronger velocity contrasts, which indicate that this approach can significantly improve the model obtained by classical ambient noise tomography.

Table des matières

Chapitre 1

Introduction

Sommaire

1.1 Thesis objectives

The Alps, formed by the interaction of the Adriatic and European plates, is the foremost region in geological and geophysical research. Unlike large mountain belts such as the Himalayas or the Andes, the lithospheric structure of the Alps and the adjacent Apennines display strong and quick changes both across and along strike, and the interpretation of underlying geodynamic processes remains under debate. In particular, tomographic studies about the upper mantle lead to considerable controversy over the geometry and origin of slabs (Lippitsch, 2003; Piromallo and Faccenna, 2004; Spakman and Wortel, 2004; Zhao et al., 2016).

The first step towards a better understanding of the geodynamic processes of the Alps is to build an accurate crustal and uppermost mantle model, as well as the Moho interface. The crustal structure of the Alpine belt has mainly been probed along seismic transects using either controlled sources (EGT, ECORS-CROP, NFP-20, Transalp) or earthquake data (Transalp, Cifalps, EASI). The gaps between these transects were filled using potential field data such as Bouguer anomaly modeling in 3-D, albeit at a much lower vertical resolution.

Ambient noise tomography has proved to be a robust imaging tool (at local scale : e.g. Brenguier et al. (2007); Picozzi et al. (2009), at regional scale : e.g. Bensen et al. (2009); Stehly et al. (2009), at global scale : e.g. Nishida et al. (2009); Haned et al. (2016)). It is based on the retrieval of the Green's function from the cross-correlation of ambient seismic noise, overcoming the limitation of the availability of earthquake

observations in traditional earthquake-based tomography. Since cross-correlations are rich in high frequency content (<20 s), the ambient noise tomography is in particular appropriate for crustal imaging. The most typical ambient noise tomography makes use of the vertical component of Rayleigh waves reconstructed from cross-correlations. The measured Rayleigh wave group or phase velocities are inverted to constrain shear-wave velocity model using the two-step surface wave inversion approach. Using this approach, Stehly et al. (2009) and Molinari et al. (2015) obtained 3-D shear wave velocity models and Moho depth maps of the Alpine region.

The increase of the number of seismic stations in recent years enables to image the Alpine region with unprecedented high-resolution. The AlpArray Seismic Network (AASN), that started on 1st January 2016, is one of the largest temporary seismological network in the academic field. Combined with the permanent seismic stations, we obtain a dense coverage of the Alpine region with station spacing around 50 km. The number of available seismic stations is 3-5 times of those in the studies by Stehly et al. (2009) and Molinari et al. (2015) . The amount of seismic stations not only improves the resolution of tomographic results, but also enables some specific tomographic methods based on dense arrays, such as Eikonal tomography (Lin et al., 2009; Lin and Ritzwoller, 2011a).

Wave-equation-based tomography using numerical modeling of wave propagation in 3-D heterogeneous medium becomes feasible with advances in numerical techniques and computational facilities (at regional and continental scales : e.g. Tape et al. (2009); Fichtner et al. (2009); Zhu et al. (2012); Yuan et al. (2014); Fichtner and Villaseñor (2015)). This naturally leads to the methodological improvement of ambient noise tomography by combining it with wave-equation-based tomographic methods, leading to ambient noise wave-equation tomography (Chen et al., 2014; Gao and Shen, 2014; Shen and Ritzwoller, 2014; Liu et al., 2017). The new method, benefiting from accurate 3-D wavefield simulation and sensitivity kernels computation, is believed to improve the final 3-D Vs model as compared to the two-step inversion approach.

The primary goal of this thesis is to build a new generation of high-resolution shear-wave velocity models of the Alpine crust and uppermost mantle using ambient noise based tomographic methods. To that end, we compile a cross-correlation dataset using four years of seismic noise recorded at 1293 broadband seismic stations across Europe. The tomography proceeds in three steps using different methods :

- In the first step, we perform ambient noise group velocity tomography for the European crust and uppermost mantle. We invert Rayleigh wave group velocity measurements in the period range 5-150 s using the well-established two-step inversion approach.
- In the second step, we perform ambient noise phase velocity tomography. Rayleigh wave phase velocity measurements are first inverted in the same manner as in step 1 for the European crust and uppermost mantle. The obtained results are used to confirm the model built in step 1. Then, Rayleigh wave phase velocity measurements in the period range 7-25 s are inverted using Eikonal tomography to obtain azimuthal anisotropy for the Alpine crust.

- In the third step, we perform ambient noise wave-equation tomography to refine the shear-wave velocity model for the Alpine crust and uppermost mantle. We iteratively improve the model built in step 1 by minimizing the phase traveltime difference between observed and synthetic waveforms in the period band 10-55 s. The inversion is performed with a WET workflow using the SEM46 code package developed within the SEISCOPE consortium (https ://seiscope2.osug.fr).

1.2 Thesis structure

This thesis contains six chapters.

In Chapter 1 (this chapter), we present the motivation and objectives of the thesis.

In Chapter 2, we review the ambient noise cross-correlation technique. We show mathematical demonstrations and numerical illustrations of the reconstruction of the Green's function from noise cross-correlations. With numerical tests, we analyze the influences of the anisotropic noise source distribution and medium heterogeneity in our specific case.

In Chapters 3-5, we present our ambient noise tomographic applications, corresponding to the three steps mentioned above. In Chapter 3, published as Lu et al. (2018), we apply the ambient noise group velocity tomography to determine a shear-wave velocity model and a probability model of interfaces for the European crust and uppermost mantle. In Chapter 4, we present two ambient noise tomographic applications based on phase velocity measurements, with a focus on the use of Eikonal tomography to study the azimuthal anisotropy of the Alpine crust. In Chapter 5, we present our application of ambient noise wave-equation tomography for the Alpine crust and uppermost mantle. We show how this new method improves the results obtained from the traditional 2-step inversion approach.

In the last chapter, we conclude on the results of the thesis and discuss the potential improvements.

Chapitre 2

Cross-correlation of ambient seismic noise

Sommaire

2.1 Introduction

It has been demonstrated experimentally and theoretically that, in the case of random or isotropic wavefields, the Green's function can be reconstructed by cross-correlating the signals recorded at two passive receivers, seeing one of them as source and another as receiver. This has opened up new horizons for the seismologists to extract information about Earth's structure from the cross-correlations of ambient seismic noise.

The goal of this thesis is to image the European crust and uppermost mantle using the cross-correlations of ambient seismic noise. Thus, it is necessary to first give an overview of the cross-correlation technique and analyze possible discrepancy between the true and

reconstructed Green's function due to non-ideal conditions, such as the anisotropic source energy distribution and medium heterogeneity.

In this section, we briefly review the development of cross-correlation technique. In section 2.2, we introduce its principles using mathematical demonstrations and numerical illustrations. In section 2.3, we quantitatively analyze the discrepancy between the true and reconstructed Green's function due to an anisotropic source energy distribution and medium heterogeneities. In the numerical experiments in section 2.2 and 2.3, we focus on our specific case. We analyze the vertical component Rayleigh waves. The anisotropic source energy distribution is estimated from our cross-correlation dataset of Europe, and the medium heterogeneities are induced using an European seismic velocity model.

2.1.1 Context

The earlier studies of cross-correlation technique can be traced back to those of Aki (1957) and Claerbout (1968). Aki (1957) derived the original formulation of spectral correlation in homogeneous medium with 2-D plane waves. This initialized the SPatial AutoCorrelation method (SPAC), which is widely used for measuring dispersive properties of surface waves in the near-surface imaging. Claerbout (1968) showed that the reflection response at a surface receiver can be retrieved by the auto-correlation of passive recordings of the transmission responses in a horizontally layered medium. A conjecture was proposed later by Claerbout for the case of two receivers, generally stating that the cross-correlation of passive recordings at two surface locations can reconstruct the reflection response at one of the locations if there was a source at the other. This provided the basis for the 'daylight imaging' technique in the exploration seismology.

More recently, successful retrieval of Green's function from cross-correlations was obtained in the field of ultrasonics (Weaver and Lobkis, 2001). They proved that the cross-correlation of a diffuse noise field in a closed system provided the complete Green's function. The results were further generalized by inducing scattering to approximate the 'diffuse noise field' environment (Lobkis and Weaver, 2001). Derode et al. (2003a,b) showed that the exact Green's function can be retrieved in an open system from the cross-correlation of multiply scattered waves based on a time-reversal experiment. Snieder (2004) used the stationary phase theorem to show the convergence of the noise correlation function towards the Green's function. They stated that the Green's function are obtained by a process of constructive interference of the scattered waves aligned with the station–station azimuth, and the equipartition of normal modes is not a necessary condition. Wapenaar (2004) derived a relation between the Green's function and the cross-correlation based on reciprocity theorem, which holds in any inhomogeneous medium.

In seismology, the first attempt was made by Campillo and Paul (2003), who successfully reconstructed the Green's function between seismic stations in the central Mexico by cross-correlating coda waves generated by 30 earthquakes along the west coast of

Mexico. Later, Shapiro and Campillo (2004) demonstrated that the fundamental mode Rayleigh wave can be extracted from the correlations of the ambient seismic noise. Body waves retrieval is reported by Roux et al. (2005), who identified the presence of direct P-waves in the noise cross-correlations using a small seismic array of Parkfield network, California.

For more details about the context of cross-correlation technique, readers can also refer to some published reviews (Campillo, 2006; Larose et al., 2006; Wapenaar et al., 2010b,a; Cupillard et al., 2012; Snieder and Larose, 2013; Campillo and Roux, 2015).

2.1.2 Applications

The successful retrieval of the Green's function from the cross-correlation of ambient seismic noise has great perspectives in seismology, because the traditional earthquake-based seismology is often limited by the spatial and temporal availability of earthquakes. Using the cross-correlation of ambient seismic noise overcomes these limitations, for the reason that each station pair becomes a virtual source-receiver pair with continuous recordings. Since N stations results into $N \cdot (N-1)/2$ source-receiver pairs, it especially favors regions with dense seismic network. Shapiro et al. (2005) first applied the cross-correlations to surface wave tomography. Since then, it has experienced a rapid evolution involving many areas in seismology, including surface wave tomography, body wave imaging, monitoring of seismic velocity changes, etc. Now, it becomes an important component of seismology, referred to as noise-based seismology.

2.1.2.1 Surface wave tomography

Surface waves travel directly beneath the surface of the Earth with highest amplitude in seismograms. It is a natural resource to image Earth's crust and uppermost mantle. Traditional surface wave tomography infer medium properties using group or phase velocities of surface waves based on earthquakes observations, which plays an important role in geophysical imaging in both regional and global scales. However, the method is limited in several aspects by the use of earthquake observations : (1) data coverage is sparse in regions of seismic silence ; (2) data coverage is often heterogeneous, as earthquakes mainly occur along the active plate boundaries ; (3) high-frequency component data (<20 s) is deficient due to the attenuation of long distance earthquake waves ; (4) precise earthquake source information is required.

In seismology, the cross-correlations of ambient seismic noise have first been applied in surface wave tomography, as the surface waves are the most easily retrieved component. This is because most noise sources are generated by near-surface activities, for instance human activities for high-frequency (>1 Hz) and 'miscroseisms' for low-frequency (<1 Hz). As a consequence, the prime component in the recorded ambient seismic noise is surface waves, in particular Rayleigh waves (Toksoz and Lacoss, 1968). Accordingly, the

cross-correlation of ambient seismic noise is also dominated by surface waves, especially Rayleigh waves.

The contribution of the cross-correlations of ambient seismic noise to the traditional surface wave tomography is evident : (1) the coverage of cross-correlation data is station-dependent. Thus, it overcomes the data availability in the regions of seismic silence, and it obviously increases the amount and spatial distribution uniformity of data in the regions of dense seismic network. (2) for the reason that the dominant periods of microseisms are less than 20 s, the cross-correlations are rich in high-frequency components (<20 s), which is crucial for crustal imaging ; (3) the cross-correlation directly infers the Green's function between two stations, so that no extra source information is required.

The first application of cross-correlations to surface wave tomography was conducted by Shapiro et al. (2005), who constructed Rayleigh waves group velocity tomographic images of California using cross-correlations of 1 month of ambient seismic noise. From then on, the cross-correlations have been extensively applied to surface wave tomography from local to global scales, prospecting the depth range from the shallow subsurface to mantle transition zone (at local scale : e.g. Brenguier et al. (2007); Picozzi et al. (2009), at regional scale : e.g. Yao et al. (2008); Stehly et al. (2009), at continental scale : e.g. Yang et al. (2007); Bensen et al. (2009), and at global scale : e.g. Nishida et al. (2009); Haned et al. (2016)). It is nowadays a promising domain, giving rise to a new class of methods referred to as 'ambient noise tomography'.

Since the ambient noise tomographic method is the core part of the thesis, we extend the discussion in each of the following chapters.

2.1.2.2 Body wave imaging

FIGURE 2.1 – Schematic illustration of the sensitivity kernel for the cross-correlation function (from Snieder and Larose (2013)). Left : for surface waves, all sources along the receiver station line contribute to the final cross-correlation function ; right : for body waves, only sources located in a specific area contribute to the final cross-correlation function.

Although surface waves are often dominant components, the cross-correlation of ambient seismic noise can potentially reconstruct the full Green's function, including also body waves. Unlike surface waves propagating along the surface, body waves travel

through the interior of the Earth and have a stronger sensitivity to medium interfaces. Thus, body waves are of great use to image deeper structure and interfaces. However, the extraction of body waves is more difficult than that of surface waves. That is due to the 3-D propagation of body waves, so that only sources located in a specific small area along the receiver-station line provide the constructive interference of cross-correlations (Fig. 2.1 right). Since the ambient noise sources are spatially and temporally unstable, the convergence towards the Green's function of body waves is slow. On the contrary, the propagation of surface waves follows a 2-D regime, therefore sources from a larger area along receiver station line can contribute to the cross-correlation. (Fig. 2.1 left).

Due to the difficulties of extraction and their relative low amplitudes, the body waves are still less prominent than surface waves in term of applications in noise-based seismology. At global scale, body waves are mainly used to retrieve deep seismic phases (Nishida, 2013; Lin et al., 2013; Boué et al., 2013, 2014a), and image inner core (Huang et al., 2015; Wang et al., 2015). At regional scale, body waves applications mainly focus on detecting major discontinuities of the earth, for instance the Moho (Zhan et al., 2010; Tibuleac and von Seggern, 2012), the mantle transition zone (Poli et al., 2012) and the D" reflector (Poli et al., 2015). Some applications at local scale for tomography and reflection imaging are reported (Draganov et al., 2009; Nakata et al., 2015).

2.1.2.3 Monitoring of seismic velocity changes

The cross-correlation of ambient seismic noise also provides us the unique chance to reconstruct continuous Greens's functions with daily or monthly temporal resolution. Benefiting from continuous Green's functions, one can measure the relative seismic velocity changes, so called noise-based monitoring. As seismic velocity changes have long been proved to be related to the subsurface stress field (O'Connell and Budiansky, 1974; Birch, 1961; Reasenberg and Aki, 1974), following the seismic velocity changes can be used to reveal the variations of physical properties in the crust.

The two basic methods for monitoring are stretching (Lobkis and Weaver, 2003) and doublet (called also Moving Window Cross Spectral method) (Poupinet et al., 1984). The former one is a time domain measurement by stretching the original waveform with a series of coefficients ϵ. The ϵ that provides the best fitting waveform is defined as the seismic velocity changes. The later one is a frequency domain measurement, which usually measures the phase shift in each sliding window between two cross-correlations and find the velocity changes through two linear regressions. The measurements are applied on both surface and coda wave parts, as time difference increases with increasing lapse time.

Seismic velocity changes are usually coincident with earthquakes with a quick velocity drop followed by a relatively slow recovery procedure (Brenguier et al., 2008a; Froment et al., 2013) and some volcanic activities (Wegler and Sens-Schönfelder, 2007; Brenguier et al., 2008b). The changes can also find its origin in some environmental factors related stress changes, such as rainfall induced pore pressure changes (Sens-Schönfelder and Wegler, 2006; Wang et al., 2017), atmospheric temperature generated thermoelastic effect

(Hillers et al., 2015a), tidal effects (Yamamura et al., 2003; Hillers et al., 2015b) and some loading effects from snow (Wang et al., 2017), etc. Therefore, noise-based monitoring can not only help to understand the variation of stress field before and after an earthquake, but also be a supplementary method to geodesy to study the climate-related stress changes in the crust.

2.2 Theory

In this section, we provide mathematical demonstrations and numerical illustrations of the reconstruction of the Green's function using cross-correlations. For mathematical demonstrations, we consider both homogeneous and heterogeneous medium. For simplicity, we consider scalar waves in both cases, but the conclusions made are also valid for vector (elastic) waves.

However, the mathematical demonstrations are often based on strong assumptions, which can be rarely met in reality. Thus, we further show numerical illustrations on the reconstruction of the Green's function under more realistic conditions. We consider two situations : (1) homogeneous medium with isotropic source energy distribution and (2) heterogeneous medium with anisotropic source energy distribution. In particular, we focus on our specific application for the European region. The anisotropic source energy distribution is approximated by the azimuthal signal-to-noise ratio patterns of our cross-correlation dataset of Europe (see section 3.2.8), and the heterogeneous medium is built using European model *EPcrust* (Molinari and Morelli, 2011).

2.2.1 Mathematical demonstrations

2.2.1.1 Homogeneous medium

Following the concept of Aki (1957), we show a mathematical demonstration on the reconstruction of the Green's function from the cross-correlation in 3-D free-space homogeneous medium. We assume an isotropic illumination of uncorrelated plane waves.

The scalar (acoustic) wave equation is a second order partial differential equation :

$$\Delta u(\vec{r};t) - \frac{1}{c^2}\frac{\partial^2 u(\vec{r};t)}{\partial t^2} = f(\vec{r};t), \tag{2.1}$$

where Δ is the Laplace operator, $u(\vec{r};t)$ is the displacement at location $\vec{r}$ and time t, c is the velocity of medium, and $f(\vec{r};t)$ is the source term that describes the effect of the source on the medium. The Green's function $G(\vec{r},\vec{r'};t)$ is a particular solution of the wave equation to an impulse source :

$$\Delta G(\vec{r},\vec{r'};t) - \frac{1}{c^2}\frac{\partial^2 G(\vec{r},\vec{r'};t)}{\partial t^2} = \delta(\vec{r}-\vec{r'})\delta(t-t'), \tag{2.2}$$

where δ is the Dirac delta function, and $\delta(\vec{r}-\vec{r'})\delta(t-t')$ denotes the impulse source at position $\vec{r'}$ and time t. In homogeneous medium, we have the solution of the Green's function in form of

$$G(\vec{r},\vec{r'};t) = \frac{1}{4\pi r}\delta(t-\frac{r}{c}) \tag{2.3}$$

in the time domain, and

$$G(\vec{r},\vec{r'};w) = \frac{1}{4\pi r}exp(-ikr) \tag{2.4}$$

in the frequency domain, where $k = w/c$ is the wavenumber and $r = |\vec{r}-\vec{r'}|$ is the distance to the impulse source. Seeing that the Green's function is the record of response at one point to an impulse source at another point, it carries information about the medium.

We consider two receivers positions $\vec{r}_1$ and $\vec{r}_2$ in the medium. According to (Cox, 1973), in case of isotropic illumination of uncorrelated plane waves, the normalized cross spectrum $C(\vec{r}_1,\vec{r}_2,w)$ of records at the two receivers can be expressed as

$$C(\vec{r}_1,\vec{r}_2;w) = J_0(kr). \tag{2.5}$$

where J_0 denotes a Bessel function of first kind and order 0, and $r = |\vec{r}_1-\vec{r}_2|$ is the distance between the two receivers. Equation 2.5, shown by Aki (1957) for 2-D case, is the essential theory of the SPatial AutoCorrelation method. It states that the phase information between two receivers can be extracted from the cross-correlation of records at the two receiver locations. Equation 2.5 can be further expressed as

$$C(\vec{r}_1,\vec{r}_2;w) = \frac{\sin(kr)}{kr}. \tag{2.6}$$

From equation 2.6, we can obtain the cross-correlation function in the time domain by its inverse Fourier transform :

$$\begin{aligned} C(\vec{r}_1,\vec{r}_2;t) &= \frac{1}{2\pi}\int_{-\inf}^{\inf}\frac{\sin(kr)}{kr}exp(iwt)dw, \\ &= \frac{1}{4\pi}\int_{-\inf}^{\inf}\frac{exp[iw(t+r/c)]}{ikr}dw - \frac{1}{4\pi}\int_{-\inf}^{\inf}\frac{exp[iw(t-r/c)]}{ikr}dw. \end{aligned} \tag{2.7}$$

Taking the time derivative of this time domain cross-correlation function, we have

$$\begin{aligned} \frac{C(\vec{r}_1,\vec{r}_2;t)}{dt} &= \frac{c}{4\pi r}\int_{-\inf}^{\inf}exp[iw(t+r/c)]dw - \frac{c}{4\pi r}\int_{-\inf}^{\inf}exp[iw(t-r/c)]dw, \\ &= \frac{c}{4\pi r}[-\delta(t-\frac{r}{c}) + \delta(t+\frac{r}{c})]. \end{aligned} \tag{2.8}$$

Regarding the solution of the Green's function given in equation 2.3, we obtain the following relation :

$$\frac{dC(\vec{r}_1,\vec{r}_2;t)}{dt} = \frac{c}{4\pi r}[-G(\vec{r}_1,\vec{r}_2,t) + G(\vec{r}_1,\vec{r}_2,-t)], \tag{2.9}$$

which means that the Green's function can be retrieved from the derivative of the cross-correlation function. The two terms in the parentheses in the right-hand side correspond to the forward and backward propagated Green's functions between the two receivers. The two terms are also known as the causal and acausal sides of the Green's function. Since the causal and acausal sides do not interfere with each other, for each side, we can have the following expression :

$$\frac{dC(\vec{r}_1,\vec{r}_2;t)}{dt} = -\frac{c}{4\pi r}G(\vec{r}_1,\vec{r}_2,t). \tag{2.10}$$

2.2.1.2 Heterogeneous medium

Here, we generalize the demonstration to heterogeneous medium. To that end, we follow the approaches of Wapenaar (2004) and Campillo and Roux (2015) using reciprocity theorem. The scalar wave equation 2.2 can be expressed as Helmholtz equation in the frequency domain :

$$\Delta G(\vec{r},\vec{r'};w) + k^2 G(\vec{r},\vec{r'};w) = \delta(\vec{r}-\vec{r'}), \tag{2.11}$$

where $G(\vec{r}, \vec{r'}; w)$ is the frequency domain Green's function for position $\vec{r}$ to an impulse source located at position $\vec{r'}$.

We consider two positions $\vec{r}_1$ and $\vec{r}_2$ in a locally heterogeneous and far-field homogeneous medium. For an arbitrarily closed surface S in the far-field, we define the flux through the surface as :

$$I = \int_S \{G(\vec{r}_1, \vec{r}; w)\nabla G(\vec{r}_2, \vec{r}; w)^* - \nabla G(\vec{r}_1, \vec{r}; w)G(\vec{r}_2, \vec{r}; w)^*\}\, dS, \tag{2.12}$$

where $G(\vec{r}_1, \vec{r'}; w)$ and $G(\vec{r}_2, \vec{r'}; w)$ are the Green's functions for the two positions $\vec{r}_1$ and $\vec{r}_2$ to a source located at position $\vec{r'}$ on the surface, ∇ denotes the divergence operator, and the asterisk $*$ indicates the complex conjugate. In an energy lossless medium, we can apply the divergence theorem :

$$\begin{aligned} I &= \int_V \nabla \{G(\vec{r}_1, \vec{r}; w)\nabla G(\vec{r}_2, \vec{r}; w)^* - \nabla G(\vec{r}_1, \vec{r}; w)G(\vec{r}_2, \vec{r}; w)^*\}\, dV, \\ &= \int_V \{G(\vec{r}_1, \vec{r}; w)\Delta G(\vec{r}_2, \vec{r}; w)^* - \Delta G(\vec{r}_1, \vec{r}; w)G(\vec{r}_2, \vec{r}; w)^*\}\, dV. \end{aligned} \tag{2.13}$$

Equations 2.12 and 2.13 give the correlation-type reciprocity theorem for scalar waves. From equation 2.11, we have

$$\begin{aligned} \Delta G(\vec{r}_1, \vec{r}; w) &= \delta(\vec{r}_1 - \vec{r'}) - k^2 G(\vec{r}_1, \vec{r}; w), \\ \Delta G(\vec{r}_2, \vec{r}; w) &= \delta(\vec{r}_2 - \vec{r'}) - k^2 G(\vec{r}_2, \vec{r}; w). \end{aligned} \tag{2.14}$$

By substituting equations 2.14 into 2.13, we obtain

$$I = G(\vec{r}_1, \vec{r}_2; w) - G(\vec{r}_2, \vec{r}_1; w)^*, \tag{2.15}$$

where $G(\vec{r}_1, \vec{r}_2; w)$ and $G(\vec{r}_2, \vec{r}_1; w)$ refer to the causal and acausal sides of the Green's function between the two positions $\vec{r}_1$ and $\vec{r}_2$. Then, we combine equations 2.12 and 2.15 to get the following relation :

$$\begin{aligned} &G(\vec{r}_1, \vec{r}_2; w) - G(\vec{r}_2, \vec{r}_1; w)^* = \\ &\int_S \{G(\vec{r}_1, \vec{r}; w)\nabla G(\vec{r}_2, \vec{r}; w)^* - \nabla G(\vec{r}_1, \vec{r}; w)G(\vec{r}_2, \vec{r}; w)^*\}\, dS. \end{aligned} \tag{2.16}$$

Since we assume the surface is far from the locally heterogeneous medium, $G(\vec{r}_1, \vec{r'}; w)$ and $G(\vec{r}_2, \vec{r'}; w)$ can be approximated by equation 2.4 :

$$\begin{aligned} G(\vec{r}_1, \vec{r}; w) &\sim \frac{1}{4\pi|\vec{r} - \vec{r}_1|} exp(-ik|\vec{r} - \vec{r}_1|), \\ G(\vec{r}_2, \vec{r}; w) &\sim \frac{1}{4\pi|\vec{r} - \vec{r}_2|} exp(-ik|\vec{r} - \vec{r}_2|), \end{aligned} \tag{2.17}$$

and therefore :

$$\begin{aligned} \Delta G(\vec{r}_1, \vec{r}; w) &\sim -ikG(\vec{r}_1, \vec{r}; w), \\ \Delta G(\vec{r}_2, \vec{r}; w) &\sim -ikG(\vec{r}_2, \vec{r}; w). \end{aligned} \tag{2.18}$$

By substituting equation 2.18 into 2.16, we have

$$G(\vec{r}_1, \vec{r}_2; w) - G(\vec{r}_2, \vec{r}_1; w)^* = -2ik \int_S \{G(\vec{r}_1, \vec{r}; w) G(\vec{r}_2, \vec{r}; w)^*\} \, dS. \tag{2.19}$$

In equation 2.19, the left hand side refers to the causal and acausal sides of the Green's function between the two positions, while the right hand side is related to the spatial integral of the cross-correlations of wavefields to sources on an arbitrary far-field closed surface. If we further assume the sources on the surface are mutually uncorrelated, equation 2.19 can be expressed in a more general way :

$$G(\vec{r}_1, \vec{r}_2; w) - G(\vec{r}_2, \vec{r}_1; w)^* = -2ik[u^{obs}(\vec{r}_1, w) u^{obs}(\vec{r}_2, w)], \tag{2.20}$$

where $u^{obs}(\vec{r}_1, w)$ and $u^{obs}(\vec{r}_2, w)$ are the frequency-domain wavefields observed at the two receiver positions. In the time domain , equation 2.20 can be expressed as

$$G(\vec{r}_1, \vec{r}_2; t) - G(\vec{r}_2, \vec{r}_1; -t)^* = -\frac{2}{c} \frac{dC(\vec{r}_1, \vec{r}_2, t)}{dt}, \tag{2.21}$$

where $C(\vec{r}_1, \vec{r}_2, t)$ is the cross-correlation of wavefields recorded at the two receiver positions. We notice that equation 2.21 is equivalent to equation 2.9, except for the amplitude. Thus, as in homogeneous medium, the Green's function can be retrieved from the derivative of the cross-correlation of wavefields in a heterogeneous medium.

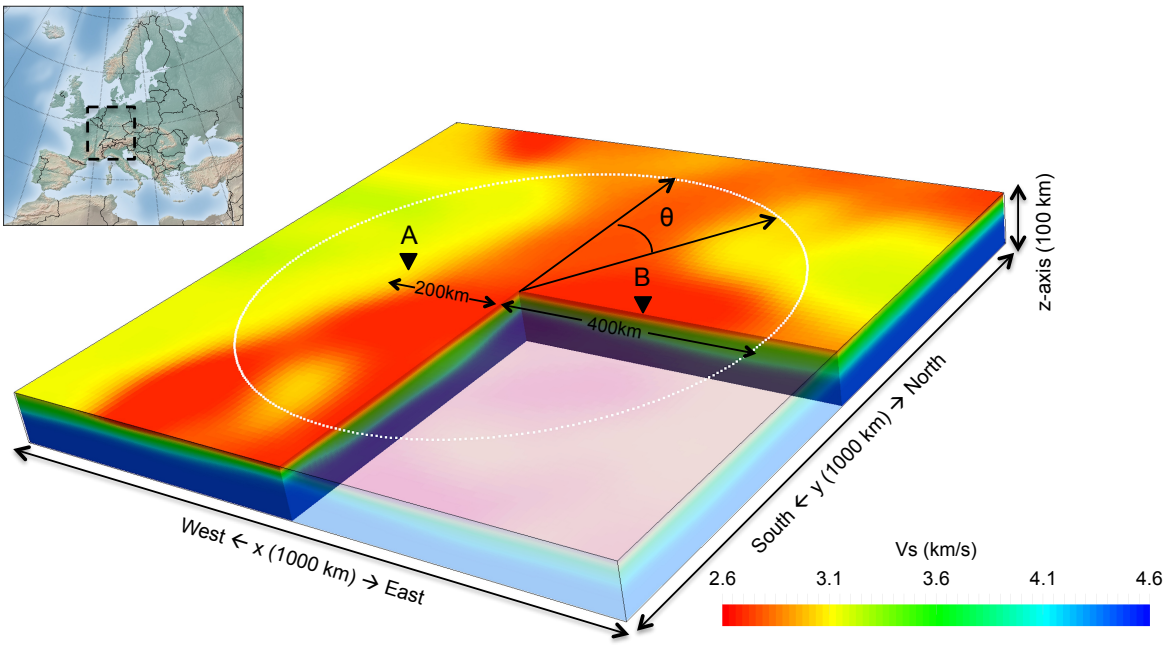

FIGURE 2.2 – Numerical setting for heterogeneous medium. Dashed line frame in the upper left figure shows the scope of the model. Color shows the shear-wave velocity values taken from the European model *EPcrust*. White dots are the schematic representation of sources along a circle, θ refers to the azimuth of a source measured from the center of model, and black triangles show the locations of the receiver station pair A-B.

2.2.2 Numerical illustrations

Using mathematical demonstrations, we show that the Green's function can be retrieved from the derivative of the cross-correlation of wavefields in both homogeneous and heterogeneous medium. In the demonstration of homogeneous medium, we assume isotropic illumination of uncorrelated plane waves in free space. In the demonstration of heterogeneous medium, we assume an energy lossless free space, that sources located on a far-field surface are mutually uncorrelated, and receivers are enclosed in a locally heterogeneous domain. In view of the strong assumptions made in the mathematical demonstrations, we further perform numerical experiments on the reconstruction of the Green's function. We analyze the vertical component of Rayleigh waves, which are used for our tomographic applications. We consider two situations : (1) homogeneous medium with isotropic source energy distribution and (2) heterogeneous medium with anisotropic source energy distribution.

The numerical simulations are performed using spectral element method in a 3-D elastic model of size 1000 km×1000 km×100 km (see Fig. 2.2 for numerical setting). In

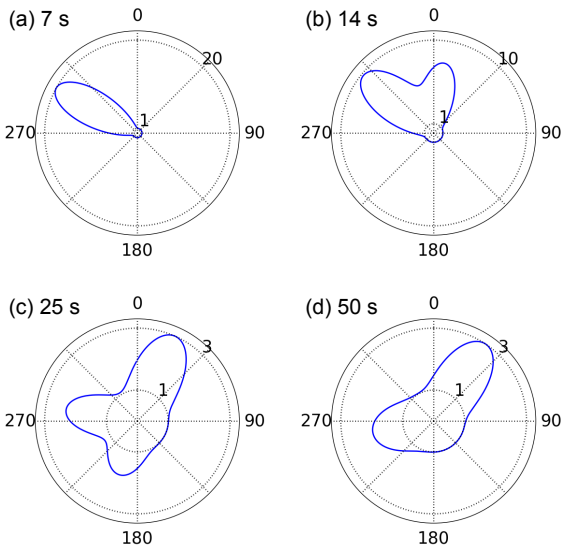

FIGURE 2.3 – Anisotropic source energy distributions at 7, 14, 25 and 50 s. We estimate the anisotropic source energy distribution using the azimuthal signal-to-noise distribution pattern measured in our cross-correlation dataset of Europe at each period (see section 3.2.8 for the azimuthal signal-to-noise distribution patterns).

situation (1), the model has a constant shear-wave velocity of 3.5 km/s, Vp and medium density are computed from the shear-wave velocity through empirical relations (Ludwig et al., 1970; Brocher, 2005). In situation (2), the values of shear-wave velocity, pressure-wave velocity and medium density are taken from the European model $EPcrust$ (Molinari and Morelli, 2011). The anisotropic source energy distribution is approximated by the azimuthal signal-to-noise pattern computed from our cross-correlation dataset of Europe at 14 s (Fig. 2.3, and see section 3.2.8 for the azimuthal signal-to-noise distribution patterns). We analyze a receiver station pair A-B located in the center of computational domain with inter-station distance of 400 km, while 3600 sources lie uniformly along a circle with radius of 400 km. We apply a vertical force at each source location, and a filtered dirac function is used as the source time function. Since both sources and receivers are on the free surface, by applying a vertical force, only Rayleigh waves are recorded as surface waves in the seismograms in a homogeneous medium, and Rayleigh waves are dominant components in the seismograms in a heterogeneous medium.

For each source along the circle, we cross-correlate vertical-component waveforms recorded at the two receiver locations. The obtained cross-correlations are tapered to $\pm$ 3 center periods around the envelope maximum, so that we can remove a part of body waves and some spurious arrivals caused by reflections from the absorbing boundaries. In situation (2) of anisotropic noise source distribution, the cross-correlation for each source is further modulated by the source energy in that azimuth. These cross-correlations for

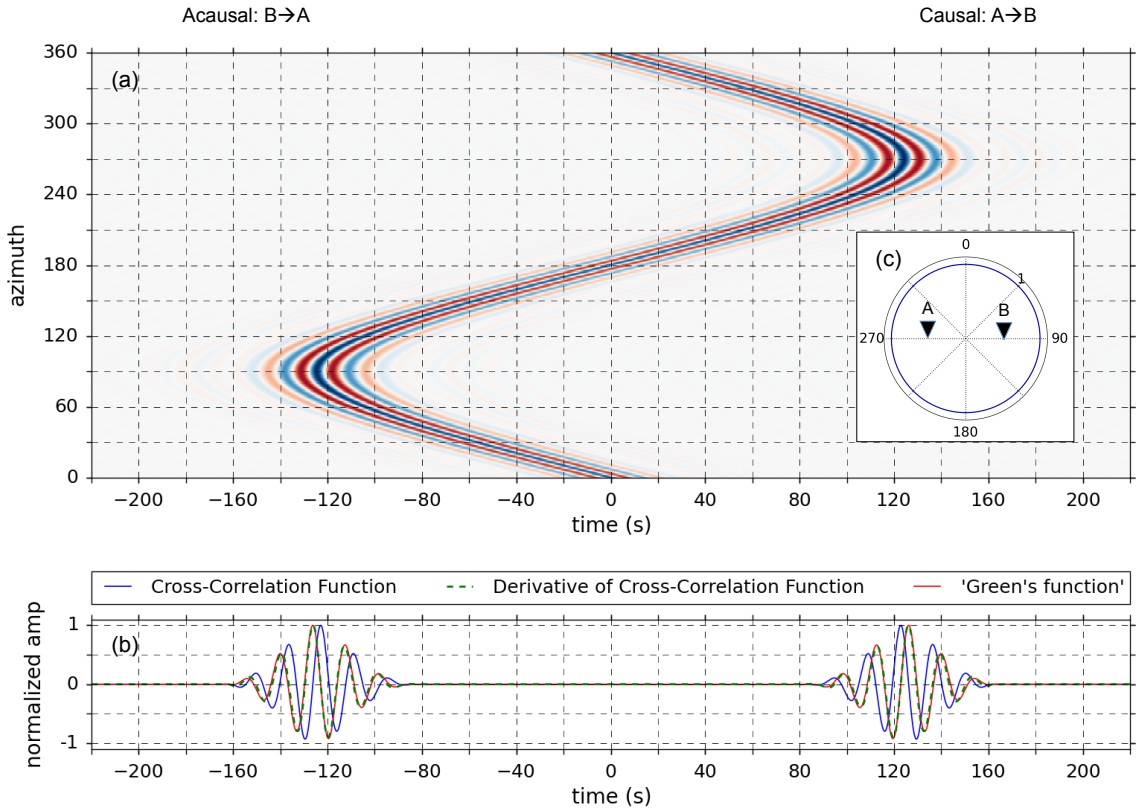

FIGURE 2.4 – Numerical illustration on the reconstruction of the Green's function at 14 s for situation (1) homogeneous medium with isotropic source energy distribution. The numerical setting is shown in Fig. 2.2, except that we use an homogenous model. We cross-correlate records at the two receiver locations A and B for sources located along the circle. The cross-correlations are plotted in (a) according to the azimuths of their corresponding sources. These cross-correlations are stacked to form the final cross-correlation function. In (b), we show the comparison of the final cross-correlation function (blue line), the derivative of final cross-correlation function (dashed green line) and the true Green's function (red line). (c) shows the isotropic source energy pattern.

individual sources are stacked to form the final cross-correlation (blue lines in Fig. 2.4b and Fig. 2.5b).

As shown in Fig. 2.4a and Fig. 2.5a, we clearly see the contributions from sources located in different azimuths to the final cross-correlation. It exists a constructive interference for cross-correlations to sources located in the receivers line direction (around 90° for B->A and around 270° for A->B). On the contrary, the cross-correlations for sources located out of the receivers line direction canceled out. This can be explained by the stationary phase theorem, that the cross-correlations with slowly varying phases add

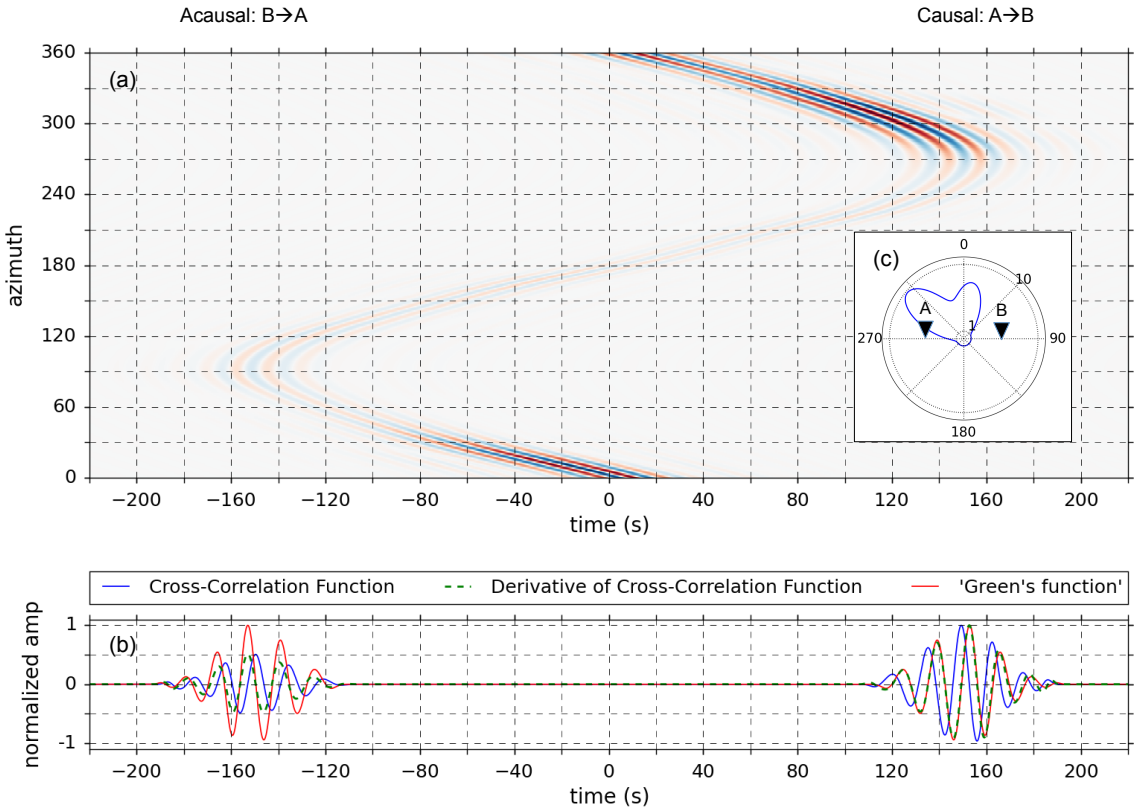

FIGURE 2.5 – Same type of plot as in Fig. 2.4 for situation (2) heterogeneous medium with anisotropic source energy distribution. The numerical setting is shown in Fig. 2.2. The amplitudes of cross-correlation for each source is modulated by the source energy in that azimuth. As a consequence, (a) is dominated by the cross-correlations for sources in the energetic directions (around 0°-30° and 280°-360°). (c) shows the anisotropic source energy pattern.

constructively, while those with rapidly varying phases add incoherently.

In our numerical experiments, the true Green's function between the two receivers is obtained from the direct records at one receiver when applying a source at the other. Fig. 2.4b and Fig. 2.5b show the comparison of the final cross-correlation (blue line), the derivative of final cross-correlation (green dashed line) and the true Green's function (red line). In Fig. 2.4b, the final cross-correlation has a $\pi/2$ phase shift to the true Green's function, while the derivative of final cross-correlation and the true Green's function are almost identical. Therefore, the conclusions made in section 2.2.1 are still valid in a homogeneous medium with isotropic source energy distribution. In Fig. 2.5b, we have observed good phase agreement between the derivative of final cross-correlation and the true Green's function in both causal and acausal sides, and an obvious amplitude

discrepancy in the acausal side. Thus, in a heterogeneous medium with anisotropic source energy distribution, we can obtain reliable phase estimations of the Green's function from the derivative of final cross-correlation, but poor retrieval of the true amplitude.

2.3 Influences of anisotropic source energy distribution and medium heterogeneity

In this section, we quantitatively analyze the influences of anisotropic source energy distribution and medium heterogeneity on the reconstruction of the Green's function from cross-correlations. Even though the numerical experiments in section 2.2.2 show good phase agreement between the true and reconstructed Green's function (the derivative of cross-correlation), we find it necessary to quantitatively estimate possible minor discrepancies as the seismic tomography often looks for a few percent of velocity variation.

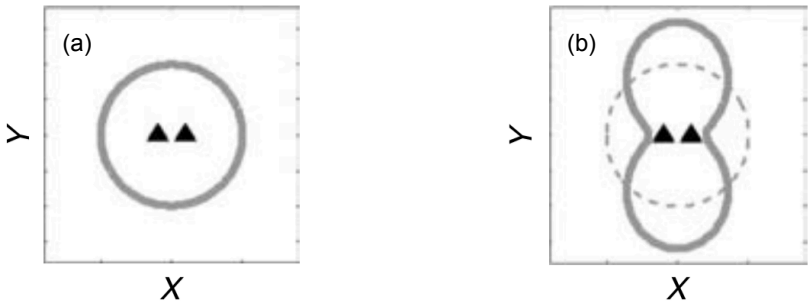

FIGURE 2.6 – Numerical setting used in the study of Froment et al. (2010). In both (a) and (b), black triangles show locations of the receiver station pair, dashed gray lines show the positions of sources located along the circle, and thick grey lines show source energy distributions. They measure the travel time errors estimated from the true and reconstructed Green's function due to the anisotropic source energy distribution shown in (b). The reconstructed Green's function obtained from the isotropic source energy distribution shown in (a) is assumed to be the true Green's function.

Weaver et al. (2009) investigated the influences of smooth anisotropic source energy distribution on traveltime (phase) estimates in a homogeneous medium, resulting in the theoretical expression of traveltime error $\delta t \sim B(\theta)''/(2tw^2B(\theta))$, where $''$ refers to the second order derivative of the azimuthal-dependent source energy distribution function $B(\theta)$, t is the total travel time and w is the angular frequency. Froment et al. (2010) confirmed the theoretical expression using real measurements from seismic prospecting data. Using the source energy distribution $B(\theta) = 1 - 0.6 \times cos(\theta)$ shown in Fig. 2.6b,

they obtained up to 2 percent of traveltime estimate error. They further extended the theoretical expression to case with a local homogeneity of the medium in the vicinity of the paths between the receivers, leading to the relation $\delta t = \delta t_p + \delta t_s$, where δt_p and δt_s are respectively the error induced by the anisotropic source energy distribution and the medium heterogeneity.

Using synthetic data, Tsai (2009) and Yao and van der Hilst (2009) have also studied the influences of anisotropic source energy distribution and medium heterogeneity on the reconstruction of the Green's function. In case of anisotropic source energy distribution in homogeneous medium, large traveltime estimate errors occur at long periods for station pairs with short inter-station distance, and located in the azimuths of quick source energy variation. These observations agree with the theoretical expression of traveltime error of Weaver et al. (2009). Besides, they showed that the effects of medium heterogeneity are nonnegligible.

However, the anisotropic source energy distribution and medium heterogeneity are site-dependent, so it is hard to generalize the results obtained in previous studies to all other cases. Here, we perform the same numerical experiments as in section 2.2.2, but for station pairs in all azimuths. We quantitatively estimate the discrepancies between the true and reconstructed Green's function in terms of amplitude, group and phase velocity measurements. We analyze three situations : (1) heterogeneous medium with anisotropic source energy distribution ; (2) homogeneous medium with anisotropic source energy distribution and (3) heterogeneous medium with isotropic source energy distribution. The three situations respectively give the total discrepancy, the discrepancy induced by the anisotropic source energy distribution and the discrepancy induced by the medium heterogeneity. As in section 2.2.2, we focus on our specific application. The anisotropic source energy distribution is approximated by the azimuthal signal-to-noise ratio patterns computed from our cross-correlation dataset of Europe (Fig. 2.3, and see section 3.2.8 for the azimuthal signal-to-noise distribution patterns), and the heterogeneous medium is built using the European model *EPcrust* (Molinari and Morelli, 2011). We consider the four representative periods 7 , 14 , 25 and 50 s in the short and intermediate period ranges. The analyses do not concern longer periods, because the seismic noise at long periods follows a global propagation regime (global hum), that differs from our numerical setting. At each period, we cut the Rayleigh wave components of the true and reconstructed Green's function by tapering the seismograms to $\pm$ 3 center periods around their envelope maxima.

2.3.1 Amplitude distortion

The reconstructed Green's function from the cross-correlation is supposed to be proportional to the true Green's function, which means an amplitude coefficient is needed to recover the absolute amplitudes of the true Green's function. For simplicity, we do not consider the absolute amplitudes in our analysis. Instead, we use the amplitude ratio of envelope maximum of causal to acausal side of the reconstructed Green's function

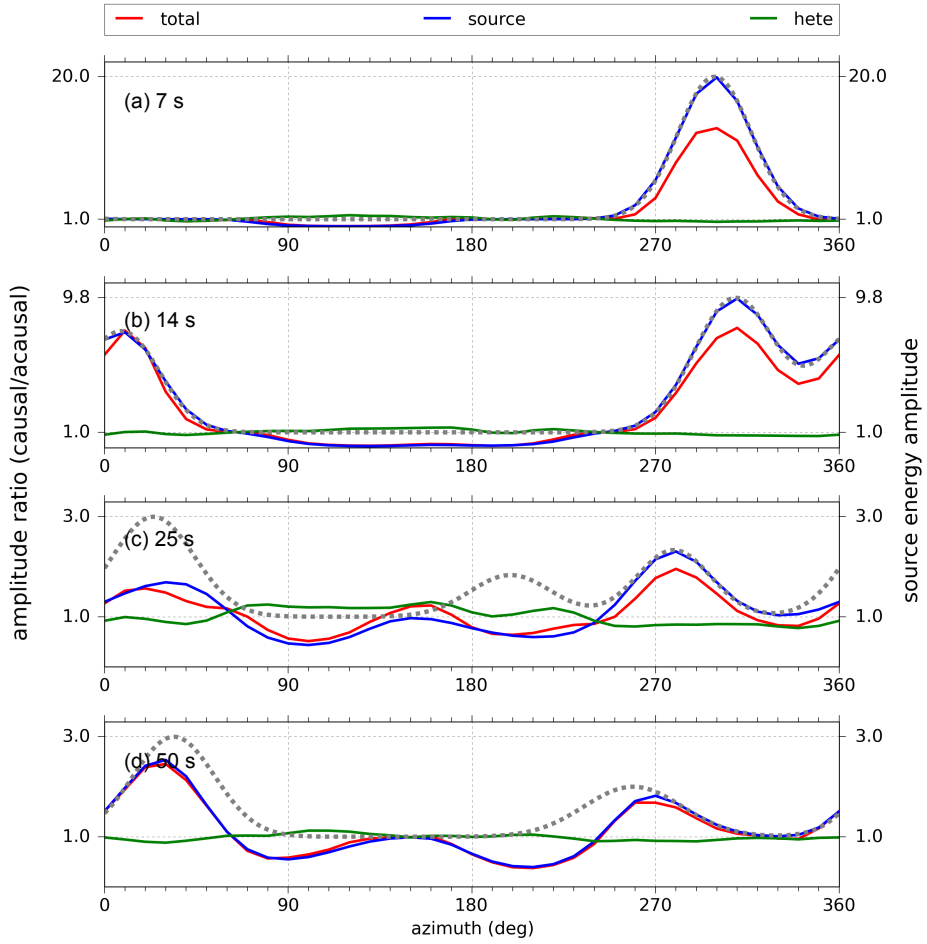

FIGURE 2.7 – Amplitude ratio of causal to acausal side of the reconstructed Green's function plotted according to the azimuth of receiver station pair at 7, 14, 25 and 50 s (see Fig. 2.2 for numerical settings). We consider three situations : (1) heterogeneous medium with anisotropic source energy distribution (red line) ; (2) homogeneous medium with anisotropic source energy distribution (blue line) and (3) heterogeneous medium with isotropic source energy distribution (green line). We show the source energy pattern using gray dashed line at each period.

as an indicator of influences of the anisotropic source energy distribution and medium heterogeneity on the amplitude.

Fig. 2.7 clearly shows that the amplitude ratio of causal to acausal side of the reconstructed Green's function is very sensitive to the anisotropic source energy distribution. At each period, the azimuthal pattern of the amplitude ratio due to the anisotropic source energy distribution is highly related to its source energy pattern. Large amplitude

ratios occur in the directions of strong source energy (for instance, around azimuth 300° at 7 s). The maximum amplitude ratio reaches 19.9, 9.7, 2.3, 2.5 at 7, 14, 25 and 50 s, respectively.

The influence of medium heterogeneity itself is very limited. However, when both the anisotropic source energy distribution and the medium heterogeneity are present, the amplitude ratios are much smaller than the case with only anisotropic source energy distribution in certain azimuths (for instance, around azimuth 300° at 7 s). The presence of medium heterogeneity has reduced the amplitude difference between the causal and acausal sides of the reconstructed Green's function, because the diffraction in heterogeneous medium results in more scattered wavefields.

Indeed, the strong influence of the anisotropic source energy distribution and medium heterogeneity on the amplitude of the reconstructed Green's function is the most important obstacle towards full waveform ambient noise tomography. As far as we know, all ambient noise tomographic applications use only phase information up to now. We extend the discussion in chapter 5.

2.3.2 Measurement errors of group and phase velocities

At each period, we measure the group and phase velocities for the true and reconstructed Green's function. The energy arrival time is obtained by picking the envelop maximum of the seismogram, and the phase arrival time is converted from the phase given by $\theta + 2\pi n$, with θ the phase angle and n the number of cycles. We consider straight-ray theory for the velocity measurements, so that the group and phase velocities are simply obtained by the ratio of inter station distance (400km) to the energy arrival time and the phase arrival time, respectively.

Fig. 2.8 and Fig. 2.9 show the measurement errors of group and phase velocities, as the differences between measurements from the true and reconstructed Green's function. Unlike the amplitude ratio, group and phase velocities are much weakly influenced by the anisotropic source energy distribution and medium heterogeneity. For both group and phase velocities, the measurement errors basically increase with period. The group velocity measurement errors reach 0.07%, 0.13%, 0.45% and 1.47% respectively at 7, 14, 25 and 50 s, considering an average velocity of 3.0, 3.5, 3.8 and 4.3 km/s at the four periods. Accordingly, the phase velocity measurement errors reach 0.07%, 0.22%, 1.82% and 1.69%. At each period, large errors often occur in the azimuths of rapid source energy variation (for instance, azimuth 240-360° at 7 s). In general, the azimuthal patterns of both group and phase velocity are more chaotic than those of amplitude ratio. As a consequence, in tomographic studies, using measurements from different azimuths can partly cancel out the errors.

We have also noticed that the group and phase velocity measurement errors for situation (1) can be estimated by the sum of situations (2) and (3). To some extent, this

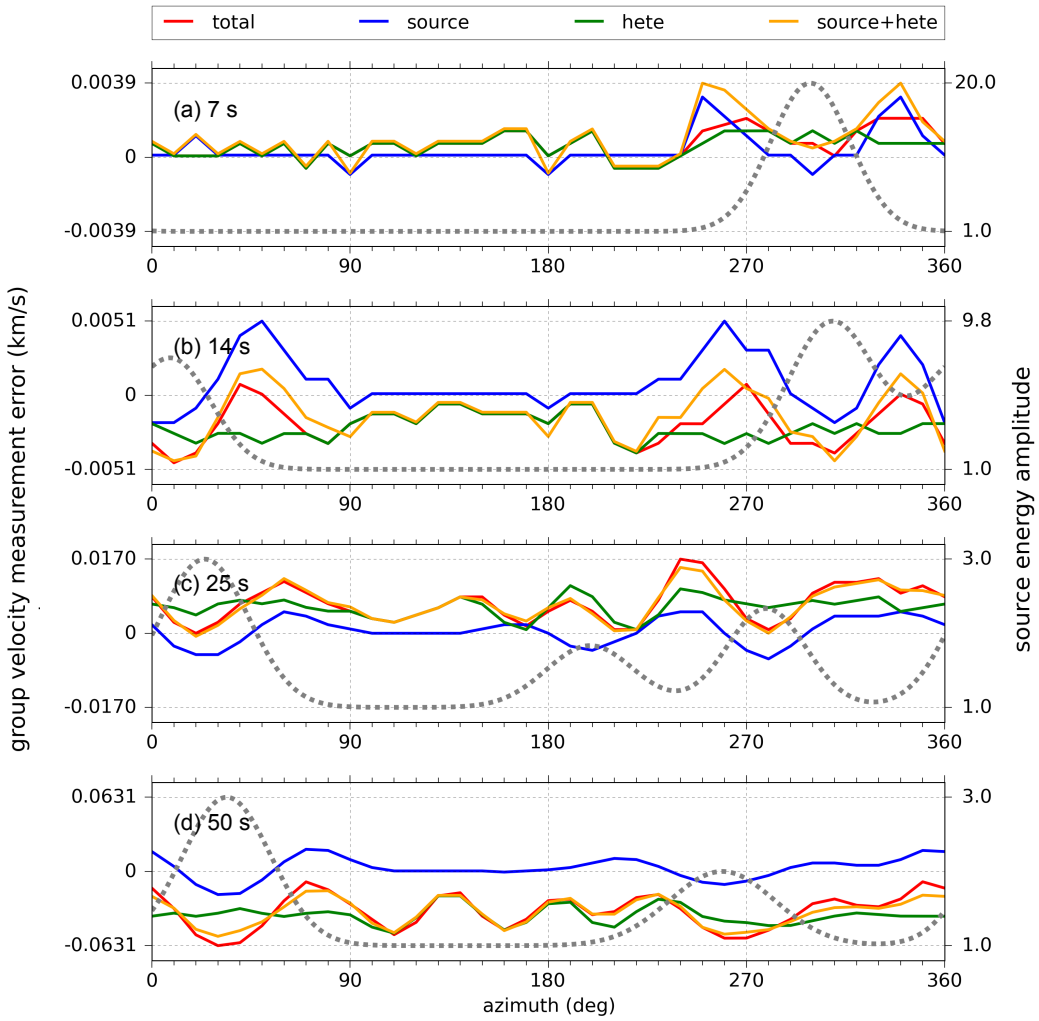

FIGURE 2.8 – Group velocity measurement errors of the reconstructed Green's function plotted according to the azimuth of receiver station pair at 7, 14, 25 and 50 s (see Fig. 2.2 for numerical settings). We consider three situations : (1) heterogeneous medium with anisotropic source energy distribution (red line) ; (2) homogeneous medium with anisotropic source energy distribution (blue line) and (3) heterogeneous medium with isotropic source energy distribution (green line). Orange line refers to the sum of situations (2) and (3). We show the source energy pattern using gray dashed line at each period.

confirms the extended theoretical expression of time estimate errors proposed by Froment et al. (2010), that the total time estimate error induced by the anisotropic source ditribution and the medium heterogeneity is the sum of those due to each of the two factors.

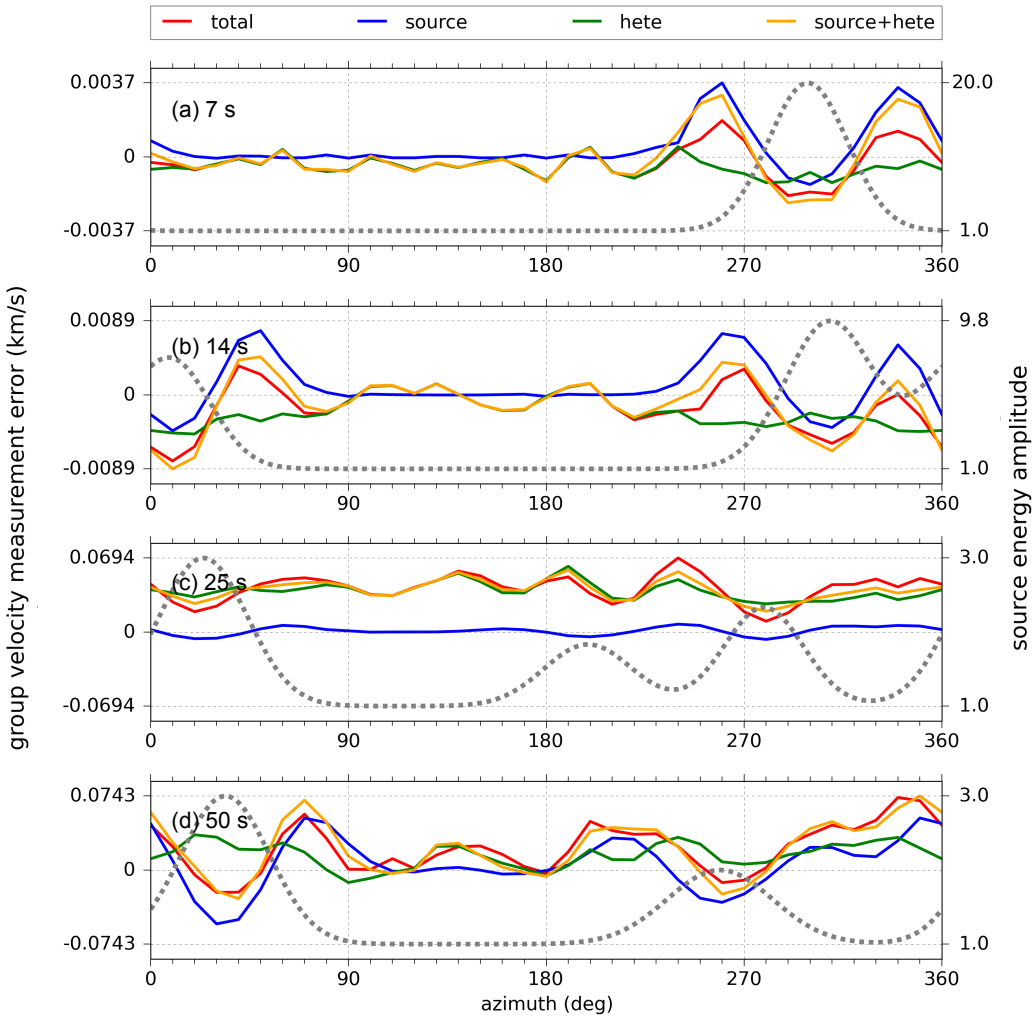

FIGURE 2.9 – Same type of plot as in Fig. 2.8, but for phase velocity measurement errors.

2.4 Conclusions

In this Chapter, we have briefly reviewed the cross-correlation technique and analyzed possible discrepancies between the true and reconstructed Green's function from the cross-correlation of ambient seismic noise. Using mathematical demonstrations, we showed that the Green's function can be reconstructed from the derivative of cross-correlation in 3-D. This conclusion is confirmed by numerical experiments for the vertical component of Rayleigh wave in homogeneous medium with isotropic source energy distribution. We further quantitatively analyzed discrepancies between the true and reconstructed Green's function when the anisotropic noise source distribution and medium

heterogeneity present. The analysis shows strong sensitivity of the amplitude of the reconstructed Green' function to the anisotropic source energy distribution. Group and phase velocity measurements are more reliable. In particular at short periods (<20 s), both group and phase velocity measurement errors are negligible. The errors basically increase with period, reaching 1.47% for group velocity measurements at 50 s and 1.82% for phase velocity measurements at 25 s. The total velocity measurement errors due to the anisotropic source energy distribution and medium heterogenerity can be estimated by the sum of the individual contribution from each of the two factors, verifying the extended theoretical expression of time estimate errors proposed by Froment et al. (2010).

In the numerical experiments, we focused on our specific case. The heterogeneous medium is built using a European model, and the anisotropic source energy pattern is estimated from our cross-correlation dataset. As a consequence, the work above gives us an good estimate of possible errors in our cross-correlation data. The reliability of group and phase velocity measurements provides a solid basis for the following ambient noise based Rayleigh wave tomographic applications.

Chapitre 3

Ambient noise group velocity tomography

Sommaire

3.1 Context

3.1.1 AlpArray Seismic Network

The AlpArray project (`http://www.alparray.ethz.ch/en/home/`) is a European multinational consortium towards better understanding of orogenesis and its relationship to mantle dynamics, plate reorganizations, surface processes and seismic hazard in the greater Alpine orogenic system (Hetényi et al., 2018). The project, which is a joined effort of 36 institutions from 11 countries, has officially started on 1st January 2016.

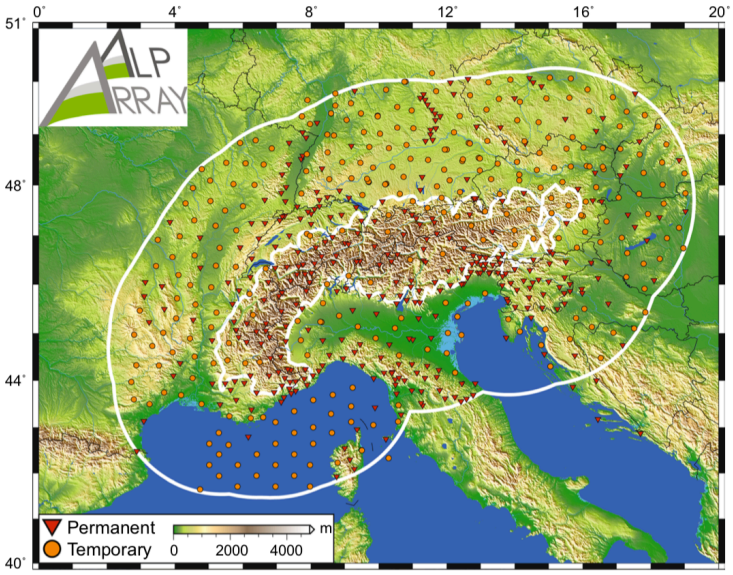

FIGURE 3.1 – Geometry of the AlpArray Seismic Network, from Hetényi et al. (2018). The permanent (red triangles) and temporary (orange circles) broadband stations cover the area within 250 km of the smoothed 800-m altitude line of the Alps (outer and inner thick white lines).

The primary focus of the project is developing the AlpArray Seismic Network (AASN), which consists in deployment of over 600 broadband seismic stations covering the greater Alpine region for 2 years, including ocean-bottom seismometers in the Ligurian Sea (Fig. 3.1). The AASN temporary seismic network, combined with permanent seismic stations, results in a dense coverage of the greater Alpine region with average station spacing less than 52 km. The available seismic data have sufficient aperture and resolution required by multiple seismological methodologies, providing a unique chance to have a self-consistent comprehensive seismic imaging of this region.

Since we use continuous seismic data in the period range of July 2012 - June 2016 in our tomographic applications, we use only half a year data from 116 AlpArray seismic stations deployed in the early stage of the project. However, as shown in Fig. 3.3, these AlpArray stations are crucial to fill the large gaps of permanent stations in the greater Alpine region.

3.1.2 Available seismic velocity models of European crust

Seismic velocity models of the Earth crust have drawn intensive research attention , because they are essential for several geophysical applications, such as mantle tomogra-

phy, location of earthquakes, seismic waveform modelling and geodynamic simulation.

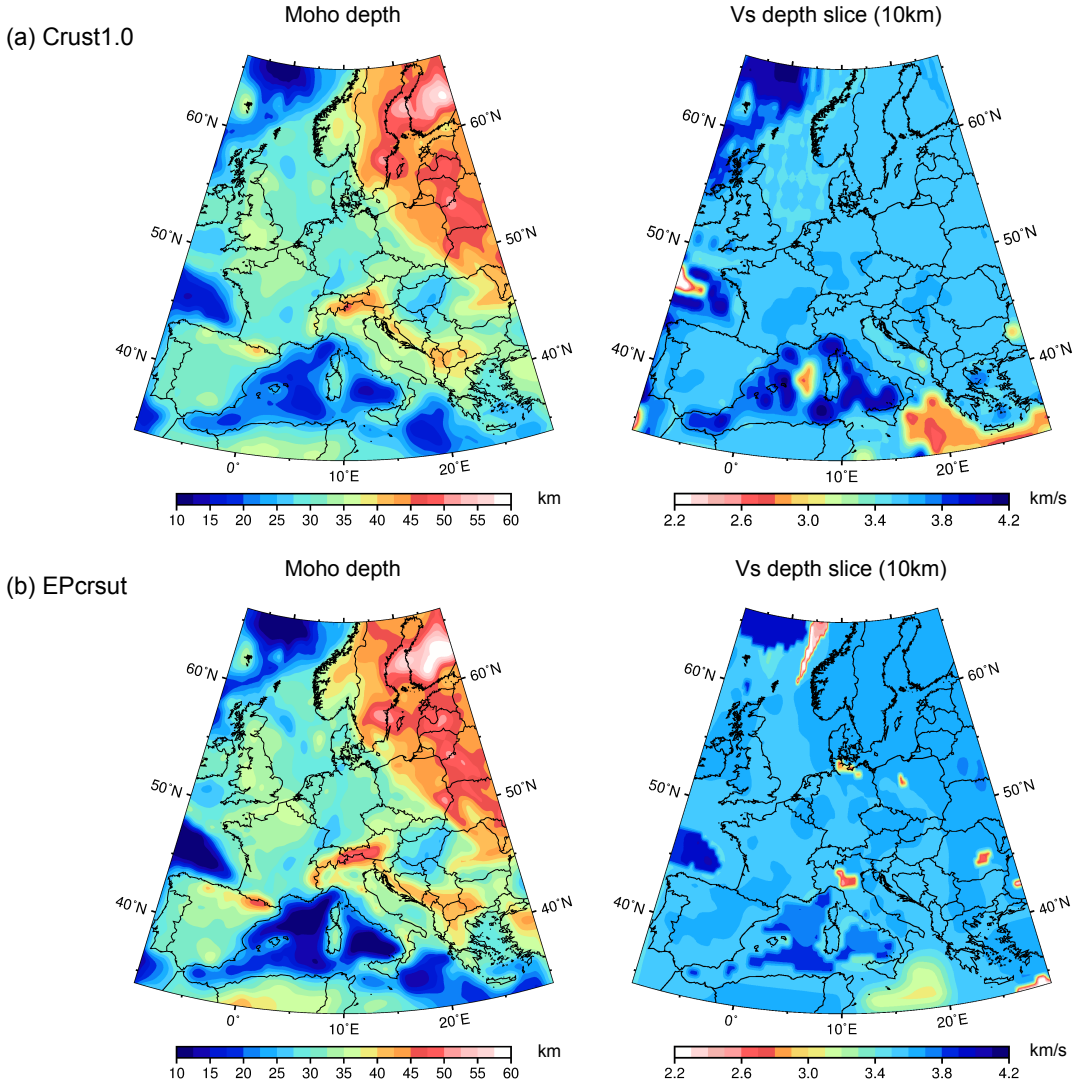

FIGURE 3.2 – Moho depth maps and Vs depth slices at 10 km from CRUST1.0 (a) and EPcrust (b).

Within Europe, CRUST1.0 (Laske et al. (2013)) and EPcrust (Molinari and Morelli, 2011) are often used as reference crustal seismic velocity models. The model CRUST1.0, derived from a compilation of seismic tomography, controlled source seismic data and geological information, is a widely used crustal seismic velocity model at global scale. The model is specified on a 1×1 degree grid and described by 8-layers, while each layer is defined by its isotropic P- and S-wave velocities and density. The model EPcrust (Molinari and Morelli, 2011) is the most up-to-date seismic velocity model at European

continental scale. It is built from a comprehensive analysis of existing geophysical results, including global, local seismic models, active and passive seismic experiments. The model is composed of 3-layers including sedimentary layer, upper crust and lower crust, while each layer is also defined by its isotropic P- and S-wave velocities and density. The released version of the model EPcrust is specified on a 0.5×0.5 degree grid.

In spite of their extensive applications, the CRUST1.0 and EPcrust are layered models specified on coarse grids with low spatial resolution. As a consequence, the two models are not appropriate for direct geological or tectonic studies, and other studies (for instance, mantle tomography) based on the two models might generate non-negligible errors. As shown in Fig. 3.2, the Moho depth maps derived from the two models are laterally smooth, and the Vs depth slices do not show good correspondence with well-recognized near-surface geological units.

Seismic ambient noise is rich in the short period band, so that it is an appropriate source of data for crustal imaging, especially in areas of low to moderate seismic activity like most of Europe. The increasing number of seismic stations in the European region further favors the ambient noise based tomographic method, which treats each seismic station pair as a source-receiver pair. Moreover, the new 1-D depth inversion algorithm that we developed in this thesis provides not only reliable seismic velocity profiles, but also valuable additional information on medium discontinuities. For these reasons, there is a strong need to derive a new generation of high-resolution continuous seismic velocity model for the European crust using ambient noise tomography. In the following section, we present our ambient noise tomography of the European crust and uppermost mantle.

3.2 High-resolution surface wave tomography of the European crust and uppermost mantle from ambient seismic noise

Article published on Geophysical Journal International. Citation : Lu, Y., Stehly, L., Paul, A., and AlpArray Working Group, 2018. High-resolution surface wave tomography of the European crust and uppermost mantle from ambient seismic noise, Geophys. J. Int., 214 (2), 1136-1150, doi :10.1093/gji/ggy188.

Summary : Taking advantage of the large number of seismic stations installed in Europe, in particular in the greater Alpine region with the AlpArray experiment, we derive a new high-resolution 3-D shear-wave velocity model of the European crust and uppermost mantle from ambient noise tomography. The correlation of up to four years of continuous vertical-component seismic recordings from 1293 broadband stations (10° W-35° E, 30° N-75° N) provides Rayleigh wave group velocity dispersion data in the period band 5-150 s at more than 0.8 million virtual source-receiver pairs. Two-dimensional Rayleigh

wave group velocity maps are estimated using adaptive parameterization to accommodate the strong heterogeneity of path coverage. A probabilistic 3-D shear-wave velocity model, including probability densities for the depth of layer boundaries and S-wave velocity values, is obtained by non-linear Bayesian inversion. A weighted average of the probabilistic model is then used as starting model for the linear inversion step, providing the final Vs model. The resulting S-wave velocity model and Moho depth are validated by comparison with previous geophysical studies. Although surface-wave tomography is weakly sensitive to layer boundaries, vertical cross-sections through our Vs model and the associated probability of presence of interfaces display striking similarities with reference controlled-source (CSS) and receiver-function sections across the Alpine belt. Our model even provides new structural information such as a ∼8 km Moho jump along the CSS ECORS-CROP profile that was not imaged by reflection data due to poor penetration across a heterogeneous upper crust. Our probabilistic and final shear wave velocity models have the potential to become new reference models of the European crust, both for crustal structure probing and geophysical studies including waveform modeling or full waveform inversion.

Key words : Ambient noise, Tomography, Europe, Alps, Shear-wave velocity model

3.2.1 Introduction

The European lithosphere is characterized by strong heterogeneity at a scale of a few tens to a few hundreds of km, in particular along its southern margin due to the long history of Tethyan subductions and collisions with Africa and the Mediterranean microplates. Until recently, reference seismic models of the European crust have been built by combining results of active and passive seismic experiments carried out at regional scale (EuCRUST-07 (Tesauro et al., 2008), Crust1.0 (Laske et al., 2013) and EPcrust (Molinari and Morelli, 2011)). Seismic models of the European mantle are derived separately using these crustal velocity models as a priori information(Boschi et al., 2009; Schivardi and Morelli, 2011; Molinari et al., 2015; Legendre et al., 2012; Zhu et al., 2015). Probing the entirety of such a heterogeneous lithosphere at a suitable resolution, for instance of a few tens of km in the upper crust and with a single method remains a challenge. In the heart of Europe, the Alps have been intensely studied by geologists for more than a century, and they provide a unique natural laboratory to advance our understanding of orogenesis and its relationship to present and past mantle dynamics. While many concepts that underlie current studies of mountain belts and convergence dynamics were born in the Alps, the dynamics of this complex belt is not yet understood due to a lack of high-quality geophysical data. A first step in the re-evaluation of deep structures and processes that occur beneath the Alps is high-resolution imaging of the crust and uppermost mantle.

In the last decades, the structure of the Alpine crust has been probed at regional scale by controlled-source seismic profiles (from west to east : ECORS-CROP, Nicolas

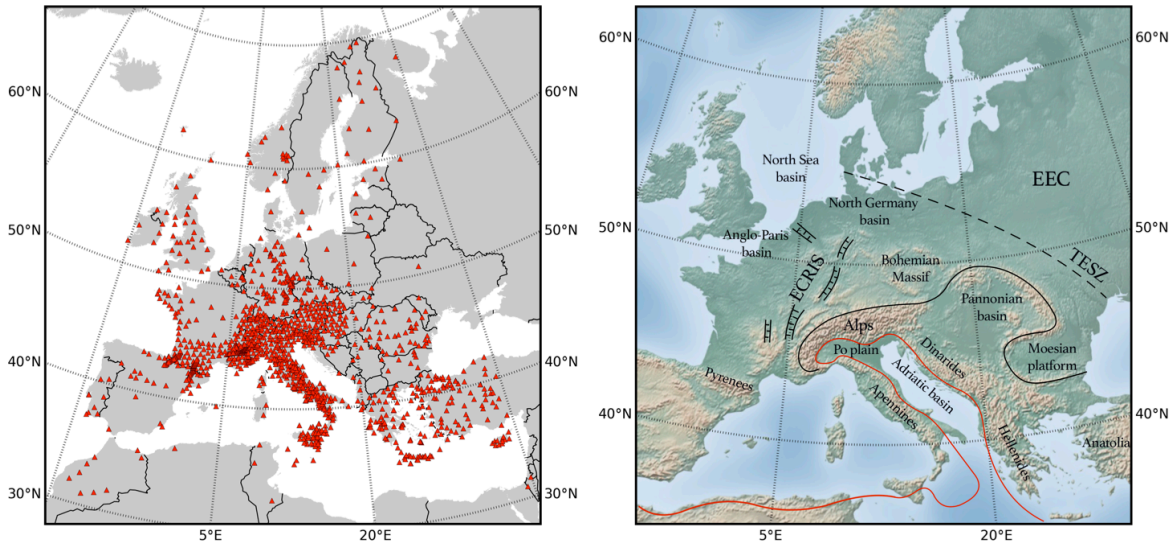

FIGURE 3.3 – Top : map of the 1293 broadband seismic stations (red triangles) used in this study. Bottom : main geological units discussed in the paper. ECRIS : European Cenozoic Rift System (modified from Dèzes et al. (2004)) ; EEC : Eastern European Craton ; TESZ : Trans-European Suture Zone (modified from Pharaoh (1999)). The black line outlines the Alpine Front, and the red line the boundary between the Eurasian and African plates (modified from Platt (2007)).

et al. (1990) ; NFP-20, Pfiffner et al. (1997) ; TRANSALP, Lüschen et al. (2004)), local earthquake tomography studies (e.g. (Paul et al., 2001), Diehl et al. (2009)) and receiver function studies (e.g. Kummerow et al. (2004) ; Spada et al. (2013) ; Zhao et al. (2015)).

Since the pioneering work by Shapiro and Campillo (2004), ambient-noise tomography has proven to be particulary efficient to image the crust and uppermost mantle at the scale of continents provided that continuous noise records are available at dense arrays of seismic stations. Indeed, experimental, theoretical and laboratory studies have shown that the Rayleigh wave between two seismic stations can be reconstructed from the cross-correlation of seismic noise records at the stations, basically turning each station to a source of seimic waves (Weaver and Lobkis, 2001, 2002; Campillo and Paul, 2003; Wapenaar, 2004; Roux et al., 2005; Larose et al., 2006; Sánchez-Sesma et al., 2006). In the Alpine region, Stehly et al. (2009); Li et al. (2010); Verbeke et al. (2012); Molinari et al. (2015), used noise correlations to compute Rayleigh wave phase and group velocity, and to derive isotropic shear-wave velocity models. Fry et al. (2010) studied the azimuthal anisotropy of Rayleigh wave phase velocities in the crust of the Western Alps.

Since the first ambient-noise tomography at European scale conducted by Yang et al. (2007), numerous new permanent broadband seismic stations have been instal-

led in Europe and their data are being distributed by the EIDA facility (`https://www.orfeus-eu.org/data/eida/`). Moreover, seismologists from ten European countries have joined their effort in the AlpArray seismic network that covers the broader Alpine region with a dense (average spacing 50 km) and homogeneous array of more than 600 seismic stations, filling the gaps between permanent stations with temporary stations (`http://www.alparray.ethz.ch/en/home/`, Hetényi et al. (2018)). These data provide a unique opportunity to image the crust and uppermost mantle beneath the greater Alps at an unprecedented resolution. In addition, the use of records from permanent stations surrounding the broader Alpine region together with stations in the Alps not only allows probing the Alpine mantle to larger depth, but it also provides the opportunity to compute a velocity model of the crust and uppermost mantle beneath most of Europe. This is the main goal of the present work, which uses up to four years of data from the 1293 stations shown in Fig. 3.3.

Through the processing of noise records at these stations, we measured Rayleigh wave velocities at several hundreds of thousands of station pairs (depending on the considered frequency), from which we derived 2-D group velocity maps in the 5-150 s period band. We finally obtained a 3-D Vs model of the crust and uppermost mantle beneath Europe by inverting for a local 1-D Vs profile in each cell.

Since the solution of this inverse problem is non-unique, we further developed the grid search approach by Stehly et al. (2009) and Macquet et al. (2014) to obtain a probabilistic 3-D Vs model. The probabilistic model gives at each location (longitude, latitude, depth) a probabilistic distribution of Vs, and the probability to have a layer boundary. This is done using a Bayesian approach that consists in exploring the whole model space assuming a three layer crust above a mantle half-space. Starting from this probabilistic 3-D Vs model, we then derived a final 3-D Vs model by linear inversion.

Imaging sharp discontinuities with surface waves such as the Rayleigh waves reconstructed from ambient-noise correlations is an issue because their velocities are not strongly sensitive to the depth of layer boundaries. We show that our model, which includes probabilistic information on the depth estimates of layer boundaries, provides reliable information on Moho depth or thickness of sedimentary basins.

In summary, the originality of our work compared to previous ambient-noise tomography studies of the Alpine region (Stehly et al., 2009; Li et al., 2010; Verbeke et al., 2012; Molinari et al., 2015) is three folds : (1) We performed ambient noise tomography at a broader scale covering a large part of Europe with a particular emphasis on the Alpine region using unprecedented density of data ; (2) Ambient noise tomography is usually restricted to the 5-50 s period band that is suitable for probing the crust. Here, we were able to measure Rayleigh wave velocity to 150 s, making it possible to get a reliable Vs model for both the crust and the uppermost mantle ; (3) We derived a 3-D Vs probabilistic model of the Alps, including the depth of layer boundaries.

This paper is organized as follows : we first present how data have been processed and the correlations computed. We then present group velocity maps obtained accross

Europe in the 5-150 s period band. In section 3.2.4, we present the 3-D shear wave velocity model obtained from the inversion of group velocity maps using a two-step data-driven inversion algorithm. Finally, we discuss some geological implications of our model for the Alpine region.

3.2.2 Data processing

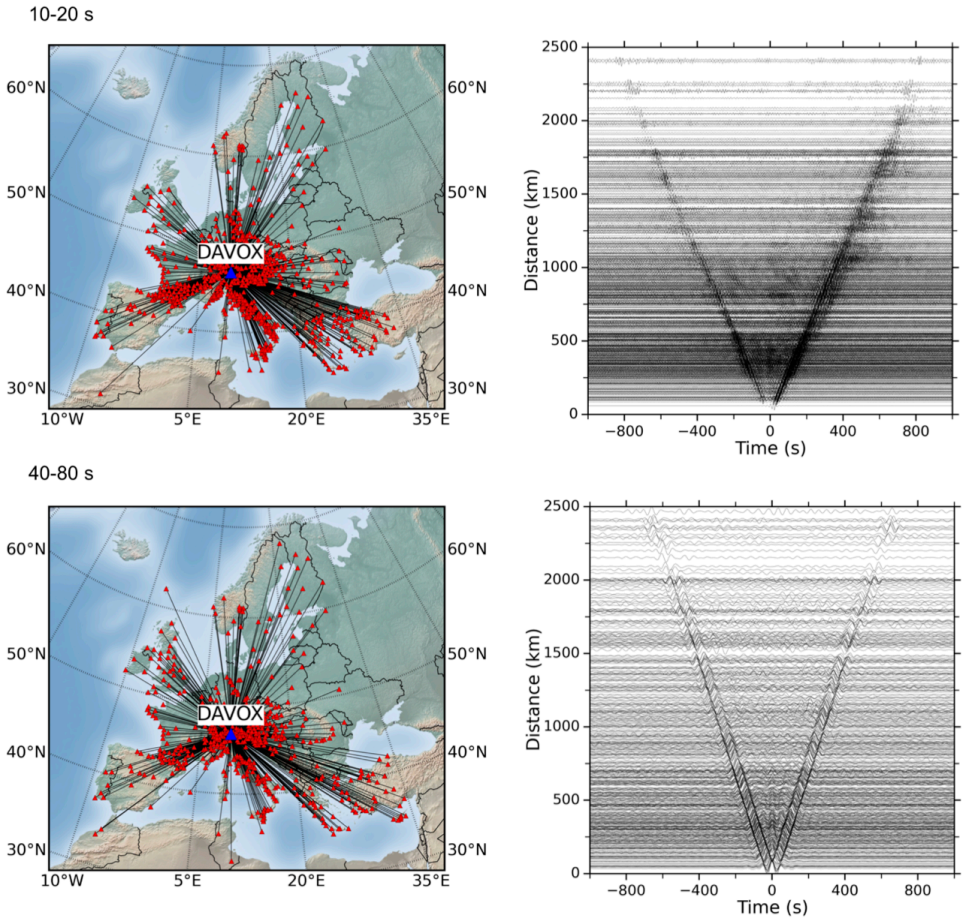

FIGURE 3.4 – Selected cross-correlations computed between DAVOX and the other stations as a function of the inter-station distance, filtered in the period bands 10-20 s (top) and 40-80 s (bottom). Fig. 3.13 in supplementary material shows cross-correlations in period bands 20-40 s and 80-150 s.

We used up to 4 years (July 2012 - June 2016) of continuous seismic noise recorded by 1293 broadband stations (Fig. 3.3), located in the area [10°W-35°E, 30°N-70°N] (see chapter origin of data). The data were obtained through the European Integrated Data

Archive (EIDA). As shown by Fig. 3.3, the best station coverage is achieved in the Alpine and Apennine regions, where the average inter-station distance is $\sim$ 50 km.

Before computing the correlations for each receiver pair, we pre-processed the noise recorded by each station in two main steps. Firstly, each daily record was detrended, band-pass filtered (0.005 - 2 Hz), corrected from the instrument response and decimated to 5 Hz. Secondly, we followed the processing scheme proposed by Boué et al. (2014b) to remove earthquakes and other transient events, and to decrease the contribution of dominant noise sources. Each daily record was split into 4 hours segments. Within each 4-hr segment, we iteratively removed energetic signals with amplitude four times greater than the standard deviation. Within each day, we removed 4-hr segment when its energy distribution is uneven and its energy is 1.5 times greater than the daily average. The remaining segments were whitened in the frequency domain.

For each of the 0.8 million station pairs, we computed the cross-correlation of up to four years of continuous noise records by segment of four hours. The resulting cross-correlations were then stacked. Fig. 3.12 (Supplementary material) shows the histogram of the number of months used to compute the stacked correlations. Fig. 3.4 shows the cross-correlations computed between station DAVOX in Switzerland and the other 1292 stations, sorted by inter-station distance in the 10-20 s and 40-80 s period bands. The cross-correlations are plotted in such a way that the causal (positive time) and acausal parts (negative time) correspond to seismic waves propagating eastwards and westwards respectively. In the 10-20 s period band, the Rayleigh wave emerges clearly with an average velocity $\sim$2.9 km.s^{-1} in both the causal and acausal parts. We note that the amplitude of the Rayleigh wave is larger in the causal than in the acausal part. This is consistent with a dominant noise source located in the northern Atlantic Ocean (Stehly et al., 2006; Pedersen and Krüger, 2007; Yang and Ritzwoller, 2008). In the period band 40-80 s, the Rayleigh wave has a velocity $\sim$3.9 km.s^{-1}. The correlations are more symmetric in this period band, because the propagation of surface waves is global, and the same noise source contributes simultaneously to both sides of the correlations.

3.2.3 Group velocity tomography

3.2.3.1 Group velocity measurement and selection

We used multiple filter analysis (Dziewonski et al., 1969; Herrmann, 1973) to compute the Rayleigh wave group velocity dispersion curves in the 5-150 s period band. We adapted the filter width to the inter-station distance to accommodate the trade-off between time and frequency domain resolution (Levshin et al., 1989). Group velocity measurements were performed separately on the causal and acausal parts for each station pair. We selected the most reliable group velocity measurements for each period by applying three criteria : (1) We considered only station pairs separated by 3 to 50 wavelengths. The lower limit aims at avoiding interference of Rayleigh waves between the causal and acausal parts, while the higher limit eliminates long paths that bring

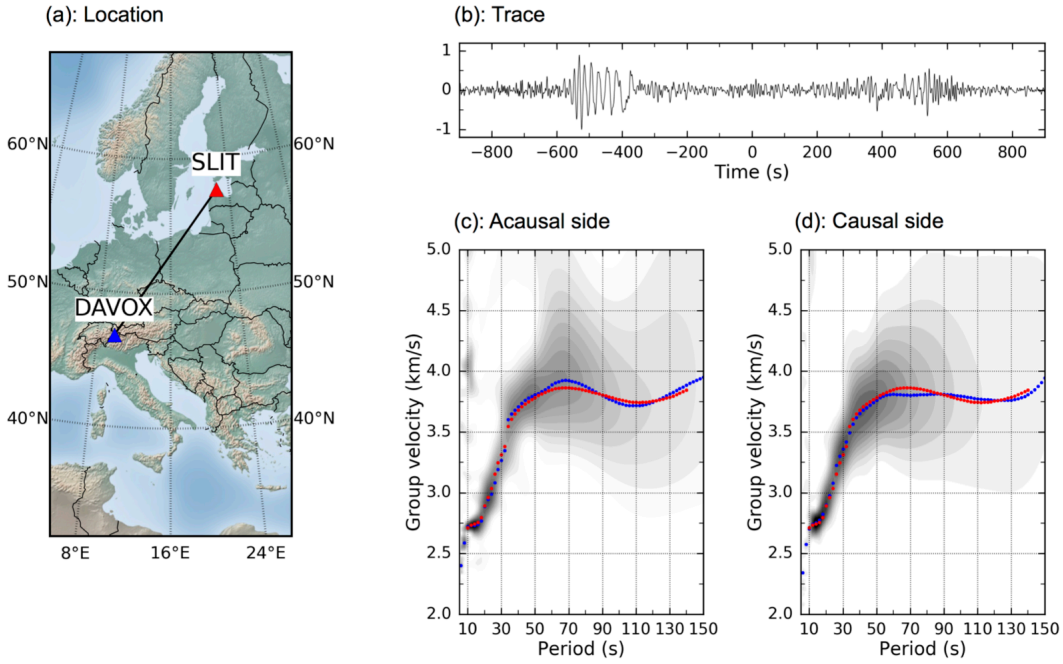

FIGURE 3.5 – Group velocity dispersion curves measured for station pair DAVOX-SLIT. (a) Location map ; (b) Noise correlation waveform ; (c-d) Results of multiple-filter analysis for the causal and acausal parts. The shaded background displays energy in the time-frequency domain. The group velocity curve is plotted as blue dots, and the final dispersion curve (average of the causal and acausal parts) is shown as a red dotted line.

Period (s)	8	15	25	40	125
Distance	395,206	593,555	654,319	628,433	330,814
SNR	222,071	366,315	370,312	175,846	22,483
Symmetry	100,852	232,314	189,369	118,548	15,294
Error ($km.s^{-1}$)	0.066	0.057	0.083	0.080	0.083

TABLE 3.1 – Number of group velocity measurements kept after each step of the selection procedure. Error refers to the average uncertainty at that period.

less information on the medium. (2) we evaluated the signal-to-noise ratio (SNR) of the causal and acausal Rayleigh waves in the period band of interest. The SNR is defined as the ratio of the peak amplitude of the Rayleigh waves to the standard deviation of the coda waves (Stehly et al., 2009). We kept only station pairs with SNR greater than 5 for both the causal and acausal parts. (3) We discarded all station pairs with group velocities measured on the causal and acausal parts of the correlations differing by more

than 0.2 km.s^{-1}. This criterion rejects measurements strongly biased by a heterogeneous distribution of noise sources.

Table 3.1 presents the statistics of the selection procedure at representative periods. After selection, we kept 2% to 30% of the station pairs depending on the period. The uncertainty on the group velocity is defined as the difference between the causal and acausal measurements. This uncertainty mainly arises from : (1) the non-homogeneous noise source distribution that results in asymmetric cross-correlations ; (2) the compromise between resolution in the time domain and resolution in the frequency domain in the time-frequency analysis. As a whole, group velocity measurements have an average uncertainty in the range 0.05-0.09 km.s^{-1}.

Finally, we averaged the causal and acausal Rayleigh wave group velocities of the selected station pairs to obtain the final measurements. As an example, Fig. 3.5 shows the dispersion curve measured between DAVOX and SLIT.

3.2.3.2 Inversion for 2-D group velocity maps : method

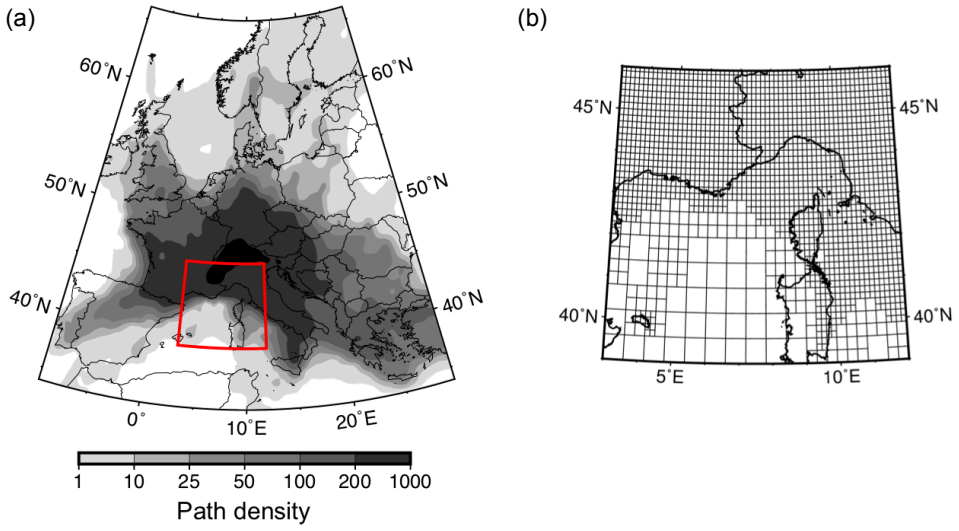

FIGURE 3.6 – Example of adaptive parameterization at period of 8 s. (a) Number of paths crossing each $0.15° \times 0.15°$ cell ; (b) Meshing resulting from the three level adaptive parameterization in a selected region (red frame in a).

At target periods, selected Rayleigh wave group velocities were inverted to 2-D tomographic maps using a linearized inversion algorithm based on the ray theory. Following Boschi and Dziewonski (1999), the inverse problem is defined as :

$$\begin{bmatrix} A \\ \mu G \end{bmatrix} * x = \begin{bmatrix} d \\ 0 \end{bmatrix} \tag{3.1}$$

where $A * x = d$ is the 'standard' ill-conditioned forward problem and $\mu G * x = 0$ is the regularization term.

In the first relation, the matrix A contains for each path the path length of Rayleigh waves within each cell. Vector d contains the difference between the observed travel time and the computed travel time derived from a homogenous initial velocity model. We chose the mean of all measurements as the initial velocity at a given period. Vector x contains the desired slowness perturbations.

The second relation defines the roughness regularization, which stabilizes the system by minimizing a first-order solution roughness for neighbouring cells. The construction of the damping operator G is discussed into detail by Schaefer et al. (2011).The roughness regularization coefficient μ was determined near the maximum curvature of the "L-curve" to compromise the trade-off between data fitting and regularization (Hansen, 2001). The linear problem was solved in a least square sense. Its solution was approximated via an iterative LSQR algorithm (Paige and Saunders, 1982).

In view of the strong heterogeneity of the data coverage, we implemented an adaptive parameterization using cell sizes of 0.6°, 0.3° and 0.15° depending on the path density. To that end, we first meshed our region of interest with 0.6° cells. Areas with more than 100 paths per cell were then discretized using 0.3° cells. We further refined the mesh to 0.15° in areas with more than 100 paths per 0.3° cell. Fig. 3.6 shows the parameterization used to compute the 8 s group velocity map. Using this adaptive parameterization, we optimized local resolution while reducing the complexity of the problem and the computational cost (Spakman and Wortel, 2004; Schaefer et al., 2011).

The resolution of 2-D tomographic result is evaluated by multi-scale checkerboard tests (see Fig. 3.14 in supplementary material). For the upper crust, the resolution reaches 0.3° in the Alpine region. At Moho depth, the resolution reaches 0.9° in the Alpine region and it is better than 1.8° in most of the area.

The uncertainty of the inversion is evaluated using Jackknifing tests (see Fig. 3.15 in supplementary material).

3.2.3.3 Group velocity maps

The depth sensitivity of Rayleigh waves depends on their dominant period. Between 5 and 150 s, Rayleigh waves are mostly sensitive to depths ranging from 4 to 200 km, which almost correspond to the whole lithosphere.

At 8 s (Fig. 3.7a), Rayleigh waves are mostly sensitive to the upper crust (5-8 km). Thus, we observe low velocity anomalies associated with sedimentary basins such as

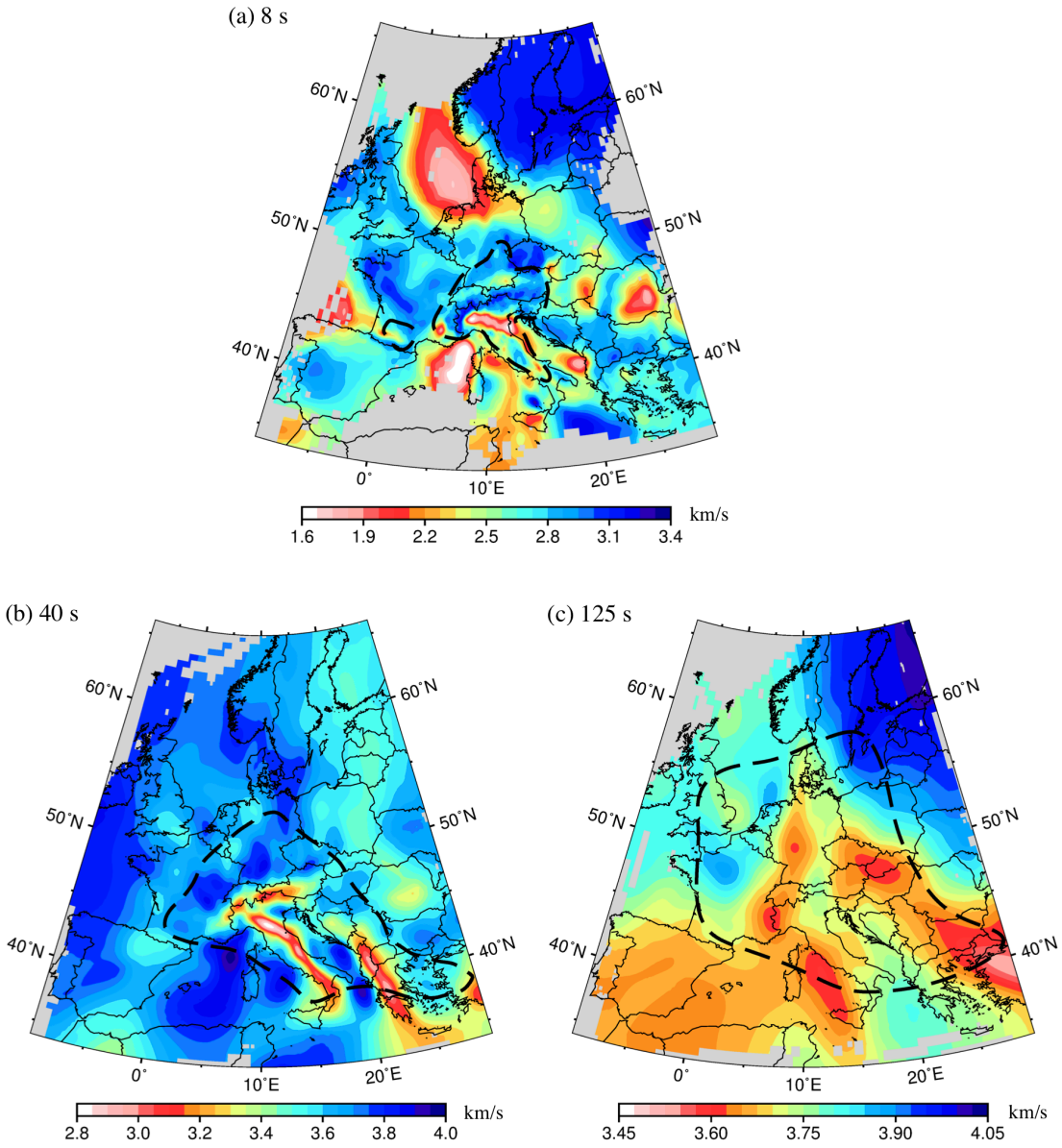

FIGURE 3.7 – Group velocity maps at representative periods 8, 40 and 125 s. We plot only cells crossed by more than 10 paths. The black dashed lines enclose the well-resolved area as defined in Fig. 3.14 from the checkerboard tests. Fig. 3.16 in supplementary material shows group velocity maps at periods 5, 15, 25 and 75 s.

the North Sea basin, the northwest Mediterranean sea, the Po plain, the Pannonian basin and and the Moesian platform. The northwest Mediterranean sea and the Po plain exhibit velocities as low as 1.5 km.s^{-1}. On the other hand, high velocity anomalies

are mainly related to orogenic belts including the Alps, as well as Variscan massifs such as the Bohemian Massif. A strong high velocity anomaly characterizes the Eastern Europe Craton (EEC, including the Baltic shield, the Russian platform and the Ukrainian platform). At 40 s (Fig. 3.7b), we image low velocity anomalies along the Alps, the Apennines, the Dinarides and the Hellenides, which are due to the deep crustal roots of these mountain ranges. At 125 s period (Fig. 3.7c), Rayleigh waves probe upper mantle structures, in particular the Trans-European Suture Zone (TESZ), which is the boundary between the high velocity lithosphere of the EEC and the low velocity lithosphere of the West-European platform.

3.2.4 3-D shear-wave velocity model

3.2.4.1 Inversion for shear-wave velocity

Our aim is to derive two 3-D Vs models of Europe : (1) A probabilistic model resulting from an exhaustive grid search which gives at each location the probability distribution of Vs and the probability of presence of a layer boundary. We shall show that this model is suitable for structural interpretation. (2) A final model computed from the probabilistic model that provides at each location and depth a unique value of Vs. This model may be used as starting point of further geophysical studies such as full waveform tomography.

To that end, we extract the local Rayleigh wave group velocity dispersion curve at each cell of our model from the group velocity maps presented in the previous section. Each dispersion curve is inverted to get a local 1-D Vs model. All 1-D Vs models are finally assembled in a quasi-3-D final Vs model. However, the 1-D inversion is still challenging since the solution of the inverse problem is non-unique. We choose to use a two-step data-driven inversion algorithm.

Firstly, we build a probabilistic model using a Bayesian approach : at each cell of the model, assuming a 4-layer structure, we search the whole model space by comparing the local Rayleigh wave dispersion curve with the dispersion curves associated with a library of 8 million of 1-D Vs models. This comparison is done in the 5-70 s period band. It provides a probabilistic model that includes at each cell/depth the probability distribution of the S-wave velocity and the probability of presence of a layer boundary.

Secondly, we further derive a unique Vs model at each cell by performing an additional linear inversion that uses the whole Rayleigh wave dispersion curve (5-150 s). This second step is mainly used to constrain the velocity in the uppermost mantle. The inversion method is presented in details in the following sections.

3.2.4.2 Computation of a probablistic Vs crustal model using a Bayesian algorithm

Our Bayesian algorithm is derived from the approach used by Bodin et al. (2012b); Shen et al. (2013) for joint inversion of surface wave dispersion and receiver functions.

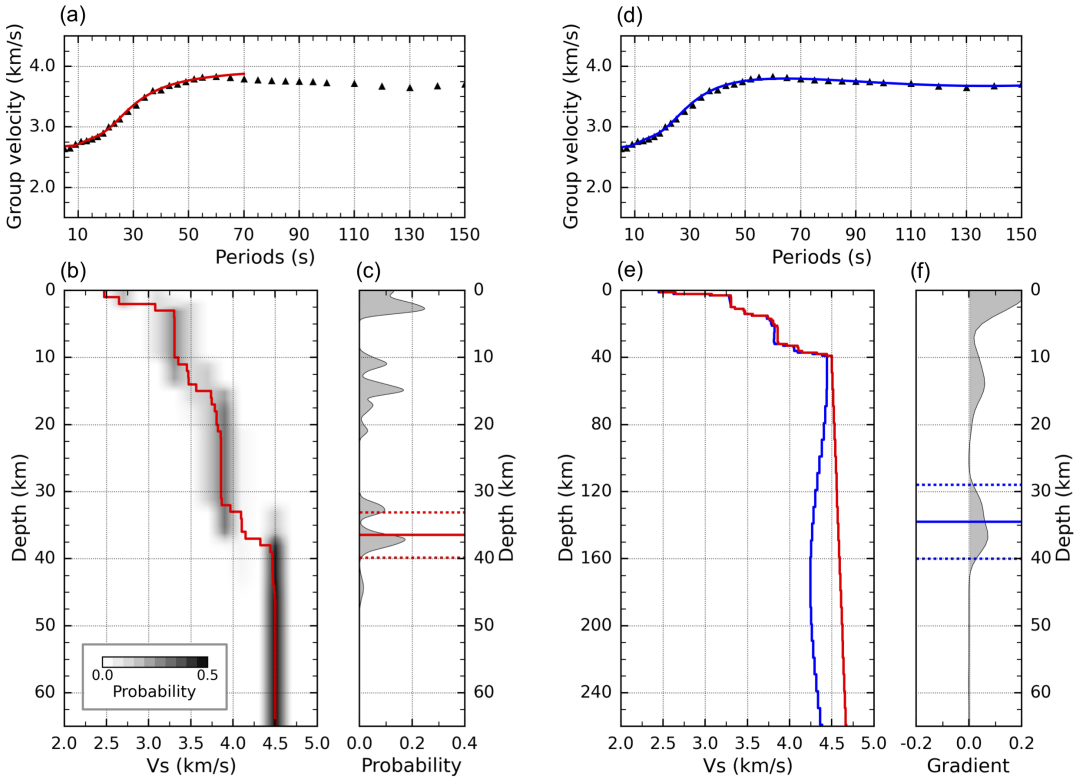

FIGURE 3.8 – Computation scheme and results of the two-step inversion of dispersion data for shear wave velocity at a cell located in the Molasse basin (8.5°E, 47.5°N). Left : non-linear Bayesian inversion step (to 70 s maximum period) ; Right : linear inversion step (to 150 s period). (a) Observed (black triangles) and predicted (red curve) Rayleigh wave dispersion curves using the Bayesian inversion. (b) Resulting Vs model displayed as a posteriori probability distribution of the S-wave velocity at each depth (gray background) obtained from the Bayesian inversion. The weighted average of the Vs models is shown as red curve. (c) Probability for a layer boundary to be located at a given depth (gray shaded curve), and estimate of Moho depth with uncertainty (continuous and dotted red lines). (d) Observed and predicted dispersion curves after the linear inversion (black triangles and blue solid line respectively). (e) Vs model predicted by the weighted average of the probabilistic model (red solid line) and final result of the linear inversion (blue solid line). The two models are similar in the crust and differ in the mantle. (f) Depth gradient of the final Vs model (shaded curve) and estimated Moho depth (blue solid line) defined as the central position of the transition zone from crustal velocity to mantle velocity.

Since our observations only contain local Rayleigh wave group velocity dispersion, we simplify the original approach in two main aspects. Firstly, we simplify the inversion parameterization assuming that at each cell the model can be described by a four-layers

	Thickness (km)	Vs (km.s^{-1})
1st layer (sediment)	0-16	1.7-2.7
2nd layer (upper crust)	0-24	2.7-3.5
3rd layer (lower crust)	2-42	3.5-4.1
4th layer (mantle)	inf	4.1-4.7
increment	1.0	0.2
Uncertainty (σ)	0.01 - 0.20 km.s^{-1}	

TABLE 3.2 – A priori parameter settings of the Bayesian inversion.

model (see Table 3.2). Secondly, we simplify the likelihood function assuming that the local Rayleigh wave velocities at different periods are independent from each other and have equal uncertainties.

In view of the relative simple parameterization, we can directly search over the full model space without using sophisticated optimization techniques. To that end, we compute a library of 8.10^6 synthetic 4-layers 1-D Vs models and their corresponding Rayleigh wave group velocity dispersion curves. Each model includes a sedimentary layer, an upper crust, a lower crust and a half-space representing the uppermost mantle. Each layer is parameterized by its thickness and S-wave velocity. We restrict the range of thicknesses and velocities to plausible values following the reference models Crust1.0 (Laske et al., 2013) and EPcrust (Molinari and Morelli, 2011). Table 3.2 presents the ranges of explored parameters. P-wave velocities and densities are converted from Vs using empirical formulas (Ludwig et al., 1970; Brocher, 2005).

At each cell, we evaluate the misfit between the local dispersion curve d_{obs} and each of the synthetic dispersion curve $g(m)$ of our library using the following misfit function :

$$\Phi(m) = (g(m) - d_{obs})^T C_e^{-1} (g(m) - d_{obs}), \tag{3.2}$$

where C_e is the covariance matrix. Similar to Shen et al. (2013), we ignore off-diagonal elements of the covariance matrix by assuming local Rayleigh wave velocities at different periods are independent. Hence, C_e is only defined by diagonal elements, which are the square of uncertainties of the observational dispersion curve at the corresponding period. This is further simplified by using a unique uncertainty σ for all periods,

$$C_e = \begin{bmatrix} \sigma^2 & 0 & 0 \\ 0 & ... & 0 \\ 0 & 0 & \sigma^2 \end{bmatrix}. \tag{3.3}$$

Following (Bodin et al., 2012b), we compute the probability that each synthetic model explains the observed dispersion curve by assuming a Gaussian-type likelihood function :

$$p(d_{obs}|m) = \frac{1}{\sqrt{|C_e|}} exp(-\frac{\Phi(m)}{2}). \tag{3.4}$$

By substituting equations 3.2 and 3.3 into 3.4, we obtain

$$p(d_{obs}|m) = \frac{1}{\sigma^N} exp\left(-\frac{(g(m) - d_{obs})^2}{2\sigma^2}\right), \tag{3.5}$$

where N is the number of measured periods. The difficulty lies in the quantitative estimate of uncertainty σ. To address this question, we use a 'hierarchical approach' and treat σ as an additional parameter (Bodin et al., 2012b). In this way, the inversion procedure performs a grid search for σ and gives a probability value for each possible σ. This self-determined uncertainty not only represents the observational error, but it also takes into account the misfit of the synthetic model.

This procedure gives us the probability that each of the synthetic models explains the local dispersion curve for each cell of the model. By analyzing this information, we can derive the probability to have an interface and a given S-wave velocity at each location/depth as documented by Fig. 3.8.

3.2.4.3 Linear inversion for the final Vs model

From the probabilistic model, we build an initial Vs model by averaging at each cell the 8.10^6 synthetic models weighted by their probability of occurrence. As a consequence, the obtained initial Vs model exhibits velocity gradients instead of sharp discontinuities. Due to our 4-layer model initial assumption, the initial Vs models have a constant velocity in the mantle, which may lead to unrealistic results after linear inversion. Thus, we assume that Vs gradually increases in the mantle from the obtained value below Moho to 4.77 km.s^{-1} at 400 km in agreement with the global model PREM (Dziewonski and Anderson, 1981). The crustal and mantle parts of the initial model are discretized with intervals of 1 and 10 km respectively. At each cell, we then perform a linear inversion of the observed local Rayleigh wave dispersion curve in the 5-150 s period band (Herrmann, 2013). The linear inversion mainly updates the upper mantle velocities.

The robustness of the final Vs model is assessed quantitatively by calculating at each cell the misfit between the observed dispersion curve and the one associated with the Vs model in different period bands (see Fig. 3.17 in supplementary material). In most of the studied region, the rms error is less than 0.04 km.s^{-1}.

3.2.4.4 Example of Vs models obtained in the Molasse basin

Fig. 3.8 shows an example of 1-D shear velocity inversion in the Molasse basin (8.5°E, 47.5°N) to illustrate our inversion procedure. Fig. 3.8b presents the probabilistic crustal model at this location. The probability distribution of Vs (shaded gray area) illustrates the non-uniqueness of the inversion of Rayleigh wave dispersion data. However, we note that at each depth, the range of plausible Vs extends over less than 0.2 km.s^{-1}. Fig. 3.8c presents the probability for a layer boundary to exist at the given depth. The probability function has two local maxima at ∼32.5 and ∼37.5 km that might be interpreted as Moho depth. This ambiguity illustrates the difficulty of mapping interfaces using ambient noise tomography due to : (1) the stronger sensitivity of Rayleigh waves to layer velocities than to velocity contrasts across interfaces, (2) our assumption that structure can be described locally by a 4-layer model while the medium has a complex structure, and (3) the intrinsic non-uniqueness of the solution of the inverse problem. In the example of Fig. 3.8, we define the Moho depth from the probabilistic Vs model as the weighted mean position rather than that of maximum probability. The resulting Moho depth is 36.5±3.5 km while the uncertainty is defined by the standard deviation.

Fig. 3.8e shows the final Vs model obtained from the probabilistic model after the linear inversion. As outlined in the previous section, the final Vs model (blue line) and the weighted average of the probabilistic Vs models (red line) are similar in the crust, and quite different at mantle depth. Fig. 3.8f displays the gradient of the final shear velocity profile as a function of depth. A strong gradient is indicative of a sharp transition zone at a layer boundary. We approximate the boundary depth as the central position of the transition zone, and its thickness gives the uncertainty on the depth estimate. The obtained Moho depth is 35±5 km.

3.2.4.5 Results : 3-D shear wave velocity model

Fig. 3.9 presents 3 depth slices at 10, 30 and 150 km in the final 3-D Vs model. The thick black dashed lines outline the well-resolved area at each depth according to the criteria discussed in section 3.2.3.3.

In the upper crust (10 km), the areas of lowest velocities (2.5 to 2.9 km.s^{-1}) correspond to thick sedimentary basins such as the North Sea basin, the North German basin, the Po plain, the Adriatic basin and the Moesian platform (Fig. 3.9a).

The 30-km depth slice (Fig. 3.9b) underlines variations in crustal thickness, with low velocities (3.5 km.s^{-1}) in the mountain belts (Pyrenees, Alps, Apennines, Dinarides and Hellenides) and high velocities (>4.1 km.s^{-1}) in the areas of stretched continental crust that crosses Western Europe from the northwesternmost Mediterranean Sea to the western Baltic Sea and North Sea Rift System including the European Cenozoic Rift System.

The 150-km depth slice (Fig. 3.9c) displays striking similarities with published mantle velocity models obtained from earthquake records (Boschi et al., 2009; Schivardi and

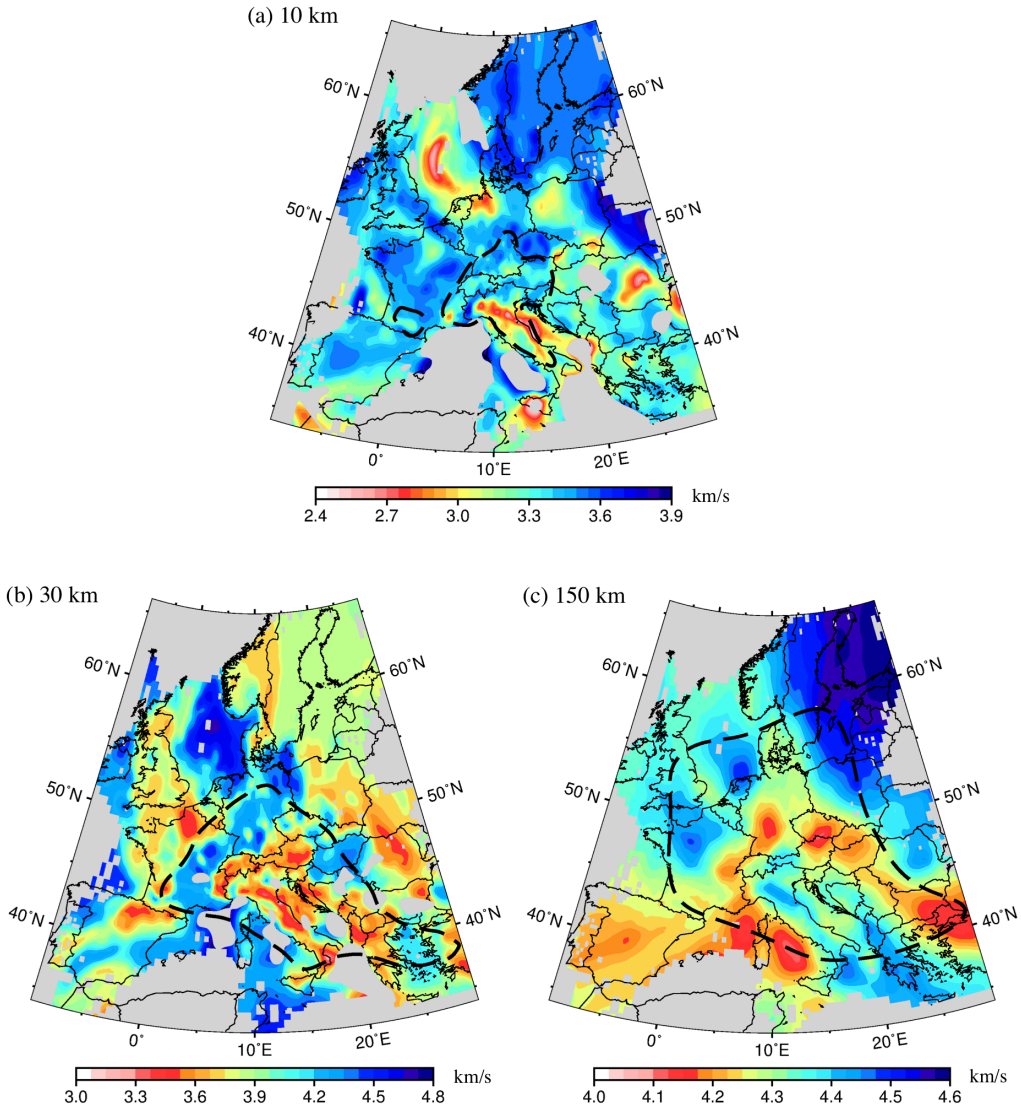

FIGURE 3.9 – Depth slices in the final Vs model at 10 km (a), 30 km (b) and 150 km (c). We only display cells with more than 10 crossing ray paths at 8 s period. Moreover, we discard cells with rms error greater than 0.06 km.s^{-}1 in the short, intermediate and long period range respectively for depth slices at 10, 30 and 150 km (Fig. 3.17). As in Fig. 3.7, the black dashed lines enclose the well-resolved area as defined from the checkerboard tests (Fig. 3.14). Fig. 3.18 in supplementary material displays depth slices at 5, 20, 40 and 75 km.

Morelli, 2011; Legendre et al., 2012; Zhu et al., 2015). The high velocities (>4.4 km.s^{-1}) of the East European Craton strongly contrast with the lower velocities (<4.3 km.s^{-1}) of Western Europe across the Trans-European Suture Zone (TESZ). Low S-wave velocities

($\sim$4.2 km.s^{-1}) characterize the upper mantle of the Western Mediterranean Sea, a roughly south-north stripe beneath the European Cenozoic Rift System and another stripe from the Pannonian basin to Northwestern Anatolia. Conversely, the upper mantle of the Anglo-Paris basin and the North Sea grabens have high Vs (4.4 - 4.5 km.s^{-1}), as well as the deep roots of orogens such as the Apennines, the central-eastern Alps and the Dinaric-Hellenic system. Our Vs model is well resolved to such unusual depths for ambient-noise tomography thanks to a good coverage by long raypaths and long duration of observation to enhance the S/N ratio at long periods. The vertical resolution is however poorer than in the crust because long-period Rayleigh waves are sensitive to a broader range of depth than short-period waves used to probe the crust.

3.2.5 Discussion : a focus on the alpine region

The result of this work is a new, high-resolution Vs model of the crust and uppermost mantle for most of the European region. It is however out of the scope of this paper to discuss its results at such a large scale. Therefore, we focus the discussion on the Alpine region which, thanks to the dense station coverage by permanent seismic networks and temporary arrays such as the AlpArray seismic network is the best-resolved area of our study region. The resolution of the area is 0.3° at 8 s (most sensitive to upper crust) and 0.9° at 40 s (most sensitive to structure at Moho depth).

3.2.5.1 Moho depth map

The Moho discontinuity is a first-order parameter in geophysical and geodynamic models of mountain belts, which draws attention in seismic tomography studies of the lithosphere. Moreover, the depth to the crust-mantle boundary in the Alpine region has been measured by numerous seismic methods including controlled source seismology (CSS), receiver function analyses and ambient noise tomographies that lead to a large set of published Moho map models at European scale (Grad and Tiira, 2009; Molinari and Morelli, 2011) or in the Alpine region (Waldhauser* et al., 1998; Stehly et al., 2009; Spada et al., 2013; Molinari et al., 2015). In Fig. 3.10, we compare our Moho depth maps (Fig. 3.10d-f) with two reference models for the European plate (Fig. 3.10a : Grad and Tiira (2009) ; Fig. 3.10b : Molinari et al. (2015)) and the most up-to-date regional Moho depth map derived from CSS and receiver function data in the greater Alpine region (Fig. 3.10c : Spada et al. (2013)). There is no single definition of the seismic crust-mantle boundary. We therefore show 3 different maps that consider the Moho as a first-order velocity change in Fig. 3.10d (see section 3.2.4.2, and Fig. 3.8c), a transition zone in Fig. 3.10e (see section 3.2.4.2, and Fig. 3.8f) and the top of upper-mantle velocities (isovelocity of 4.1 km.s^{-1}) in Fig. 3.10f.

The main features of our three Moho maps (Fig. 3.10d-f) are similar, except in the region of the Ivrea body (IB in Fig. 3.10e) which is a high-density, high-velocity body located at crustal depth and interpreted as a slice of serpentinized Adriatic upper mantle

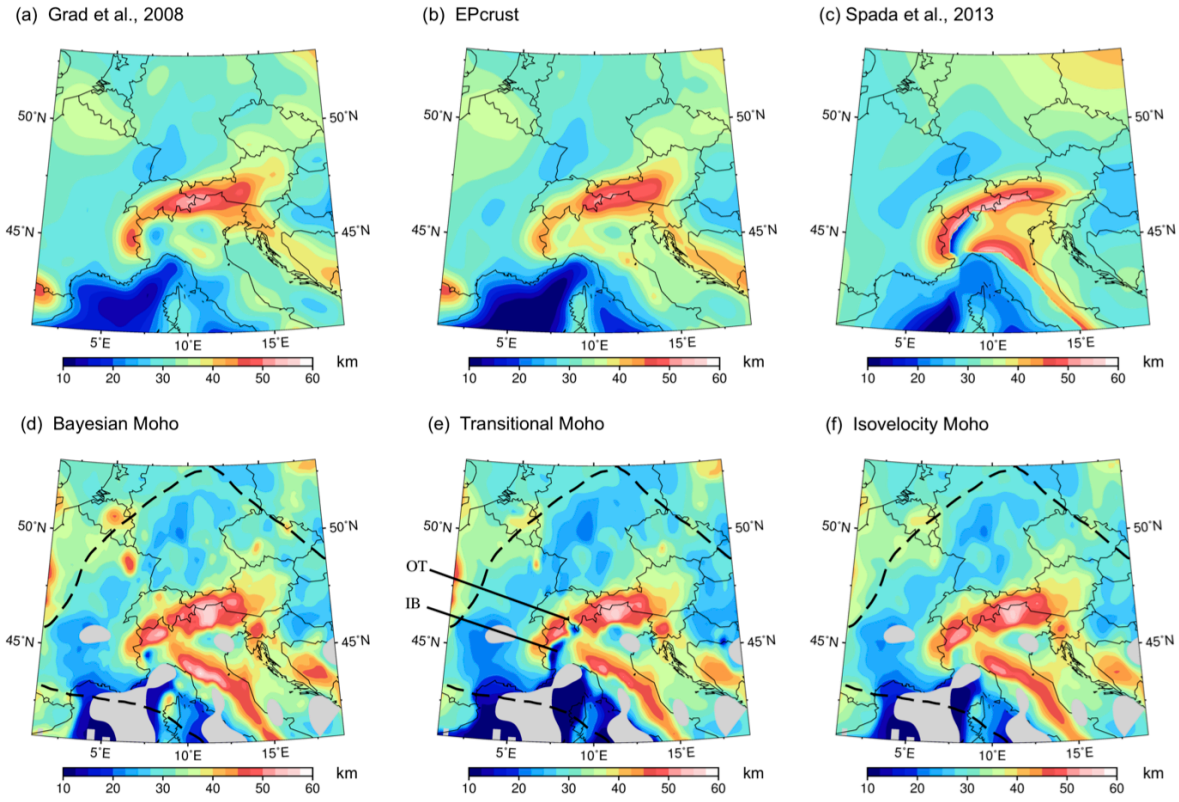

FIGURE 3.10 – Moho depth maps from previous works (a : Grad and Tiira (2009) ; b : model EPcrust, Molinari and Morelli (2011) ; c : Spada et al. (2013)) and derived from this study (d : using the probability for a boundary to be located at the given depth ; e : using the depth gradient of Vs ; f : using the isovelocity 4.2 km.s^{-1}). In each map d-f, the black dashed line encloses the well-resolved area defined at 40 s period (see Fig. 3.14). Besides, we also discard areas with rms error greater than 0.06 km.s^{-1} in the intermediate period band (see Fig. 3.17). IB : Ivrea body ; OT : Ossola-Tessin region. Supplementary Fig. 3.19 shows two 3-D views of the Bayesian Moho depth map that emphasize its strong and rapid lateral changes.

(Closs and Labrouste, 1963; Nicolas et al., 1990). The shallow Moho on top of the Ivrea body shows up well in Fig. 3.10e (transitional Moho) because it is characterized by a strong velocity gradient, albeit with anomalously low Vs in the mantle slice due to serpentinization.

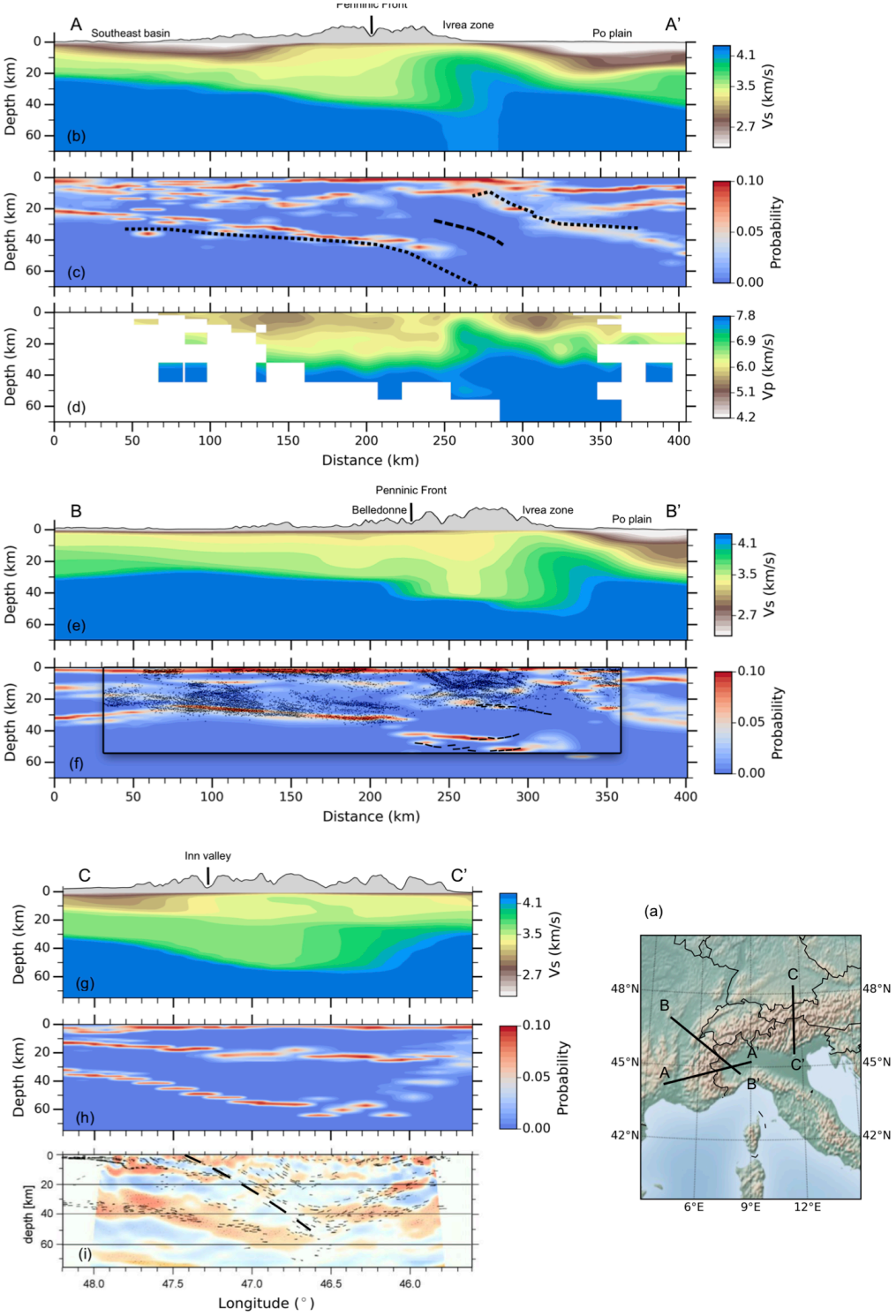
A
Southeast basin
Ivrea zone
Po plain
A'
Depth (km)
(b)
Vs (km/s)
(c)
Probability
(d)
Vp (km/s)
Distance (km)
Penninic Front
B
Belledonne
Ivrea zone
Po plain
B'
(e)
(f)
C
Inn valley
C'
(g)
(h)
(i)
depth [km]
Longitude (°)
(a)
48°N
45°N
42°N
6°E
9°E
12°E

FIGURE 3.11 *(previous page)* – Depth-sections along three representative profiles across the Alpine mountain range : Cifalps (AA', b-d), ECORS-CROP (BB', e-f) and Transalp (CC', g-i). (a) : Location map. For each section, we display the Vs structure (b, e, g), the a posteriori probability density of interfaces derived from the Bayesian inversion (c, f, h) and their comparison with other geophysical studies (c : from Zhao et al. (2015) ; d : from Solarino et al. (2018) ; f : from Sénéchal and Thouvenot (1991) ; i : from Kummerow et al. (2004)). In (c), the black dashed lines indicate the European Moho, the bottom of the Ivrea body and the Adriatic Moho estimated from receiver function analysis along the Cifalps transect. (d) : Vp model obtained from local earthquake tomography along Cifalps. (f) : migrated line-drawing of the vertical seismic reflection data (black dots) and wide-angle seismic reflection data (black dashed lines) for ECORS-CROP transect (inside the black frame). (i) : migrated receiver function data (blue-to-red colors) and line-drawing of the controlled source seismic experiment Transalp. The thick black dashed line indicates the Sub-Tauern ramp.

The comparison with three reference models shows that our Moho maps include more details thanks to our much denser dataset and hence higher resolution. For example, the narrow and very shallow Moho of the Ivrea body shows up in Fig. 3.10e, and to a lesser extent in Fig. 3.10d while it is only visible in Fig. 3.10c. Similarly, the model by Spada et al. (2013) is the only one that displays the thick crust of the Northern Apennines as well as in our Moho models. As Molinari et al. (2015) obtained a similar result with ambient-noise tomography, we confirm again the large Moho depth values estimated in the northern Apennines by Piana Agostinetti and Amato (2009) from receiver function data (∼52 km maximum crustal thickness). The division of the Alpine arc into two regions of thick crust separated by a narrow zone of thinner crust in the central Alps (namely beneath the Ossola-Tessin region, see Fig. 3.10e) is more visible in our Moho maps than in any of the three reference models, in particular in (Fig. 3.10c by Spada et al. (2013). To the west and the north of the Alpine arc, the shallow Moho of the European Cenozoic Rift System is also more visible in our model.

3.2.5.2 Cross-sections along reference profiles (Cifalps, ECORS-CROP, Transalp)

In this section, we compare our results to CSS and receiver function results along three reference cross-sections of the southwestern (Cifalps), northwestern (ECORS-CROP) and eastern Alps (Transalp). The locations of the cross-sections are shown in Fig. 3.11a.

3.2.5.2.1 Cifalps receiver function profile (AA' in Fig. 3.11b-d) The Cifalps experiment is a roughly linear profile of broadband seismic stations installed for 14 months from the Rhone valley (southern France) to the Po plain (northern Italy) across the southwestern Alps. Fig. 3.11b-d compare our results to those of the receiver function

analysis by Zhao et al. (2015) and the local earthquake tomography (LET) by Solarino et al. (2018). They show that the depth to the European Moho estimated from ambient-noise tomography (ANT) is in good agreement with the Moho depth estimated from receiver functions (RF, thick black dotted line) beneath the Frontal Penninic thrust (FPT) and its surroundings (150-210 km). Further to the east, the northeastward dipping European Moho imaged as a weak P-to-S converted phase on the RF profile at depths >45 km shows up with ambient-noise tomography. At the western end of the profile, the RF Moho is deeper than the ANT Moho by 5-8 km beneath the Southeast Basin. The use of an inappropriate velocity model in the migration of the RF data may explain this difference. The Moho structure estimated from ANT beneath the Po plain and on top of the Ivrea body (abscissae > 270 km) correlates well with the RF Moho. The Vs anomaly of the Ivrea body in Fig. 3.11b has a similar shape as the high Vp anomaly imaged from LET in Fig. 3.11d, with a vertical western boundary.

3.2.5.2.2 CSS profile ECORS-CROP (BB' in Fig. 3.11e-f) Fig. 3.11e-f display a comparison between our results and the migrated line-drawing of the ECORS-CROP CSS experiments in the northwestern Alps (Thouvenot et al., 1990; Sénéchal and Thouvenot, 1991). In the European side west of the Frontal Penninic Thrust, the agreement between the ANT Moho and the ECORS-CROP Moho imaged as the base of the reflective lower crust is striking. Further east, the ANT also delineates the European Moho at larger depths (45-55 km) beneath the internal zones, in the part of the section where it was detected by wide-angle profiling but not by near-vertical reflection data. The ANT detects a step of 8 km in the European Moho a few km to the west of the FPT. A similar step can be observed between the Moho of the ECORS-CROP near-vertical reflection section beneath the Belledonne Massif at 38 km depth and the wide-angle Moho reflections at 48-50 km a few km further east (thick dashed lines in Fig. 3.11f). A mid-crustal boundary is detected by the ANT at 25 km depth at the same location as the base of the thick band of reflections in the upper crust of the internal zones. Further east, our ANT also detects the top of the Ivrea body at ∼10 km beneath the westernmost Po plan, and a step-by-step increase of the Adriatic Moho depth that is similar to the results of the ECORS-CROP wide-angle experiment reported by Thouvenot et al. (1990). The shape of the Ivrea body as depicted by the Vs section in Fig. 3.11e is similar to the Cifalps section (Fig. 3.11b) with a vertical western boundary.

3.2.5.2.3 Receiver function and CSS profile Transalp (CC' in Fig. 3.11g-i) The third reference cross-section is the Transalp profile in the eastern Alps (Transalp Working Group 2002). The experiment combined active (near-vertical seismic profiling, wide-angle profiles, cross-line refraction profiles ; (Lüschen et al., 2004)) and passive (receiver function analysis ; (Kummerow et al., 2004)) seismic imaging. Fig. 3.11g-i compare our Vs model (Fig. 3.11g) and probability of occurrence of interfaces (Fig. 3.11h) with the results of the near-vertical reflection profile (migrated line-drawing) and receiver function section (Fig. 3.11i). In the northern half of the profile, our Moho fits very well

the European Moho imaged by near-vertical reflection profiling. This is not the case in the Adriatic side of the section, south of the suture (the so-called "Sub-Tauern ramp" of Lüschen et al. (2004)). The northernmost Adriatic Moho is well delineated by ANT, but 10-15 km deeper than the reflection Moho. Further south, the ANT does not give a well-defined Moho because a large set of crustal models with different Moho depths fit equally well the observed Rayleigh wave dispersion data. Among the three reference cross-sections, the Adriatic side of the Transalp profile is the only example of a clear misfit between our ANT crustal structure and the results of active or passive seismic imaging. Nevertheless, Fig. 3.11i shows that the reflection profile and the receiver function analysis also disagree on the depth of the Adriatic Moho, in particular close to the suture. Our results may even suggest that the European crust underthrusts the Adriatic crust, if we assume that the clear interface at ∼60 km depth in the Adriatic side is the continuation of the European Moho. This hypothesis was not favored by the Transalp team in spite of some clues of overlapping Adriatic and European Mohos in the RF sections (Fig. 2 in Kummerow et al. (2004)).

3.2.6 Conclusions

Taking advantage of the rapidly increasing number of broadband seismic stations in Europe in the last ten years, including the AlpArray temporary seismic network in the greater Alpine region, we compiled a large dataset including up to four years of vertical-component continuous seismic records from 1293 stations. Daily records were cross-correlated and stacked for ∼0.8 million station pairs. For each station pair, we measured Rayleigh wave group velocity from the cross-correlation function in the period band 5-150 s and we made a careful selection of measurements according to inter-station distance, signal-to-noise ratio, similarity of measurements in the causal and acausal sides. Two-dimensional group velocity maps were computed using adaptive parameterization taking into account local path density. In a final step, we inverted local group velocity dispersion curves extracted at each cell for a set of 1-D Vs models. The 1-D inversion follows a two-step data-driven inversion algorithm, with a non-linear Bayesian inversion followed by a linear least-square inversion.

Our main methodological improvement is this two-step data-driven inversion algorithm that results in two reliable velocity models without a priori information. The first step is a Bayesian inversion that yields a probabilistic model, which result from an exhaustive grid search in a large solution space. It is based on the assumption that at each location, the crust and upper mantle can be described by a four layer model. It provides the probability distribution of Vs and interface depths. In the second step of the inversion, we extract a final Vs model from the probabilistic model using a linear inversion.

Our final Vs model is so far the highest resolution shear-wave velocity model of the European crust derived from ambient noise tomography (0.3° in the upper crust and 0.9° at Moho depth in the Alpine region). Our probabilistic model displays striking

similarities with published seismic profiles along three reference cross-sections across the Alpine mountain range, Cifalps, ECORS-CROP and Transalp. It even provides additional information on the crustal structure, for example in the internal zone of the Alpine orogen where the ECORS-CROP CSS profile failed to probe the deep crust due to the strong reflectivity of the upper crust. A comparison of vertical cross-sections in our two models along the CIFALPS (southwestern Alps) and ECORS-CROP (northwestern Alps) points out unexpected strong differences in the image of the European Moho that deepens continuously towards the northeast along CIFALPS while it displays a $\sim$8 km Moho jump beneath the inner boarder of the Belledonne Massif along the ECORS-CROP profile. This illustrates that with a dense networks of broadband stations and using our inversion scheme, ambient noise tomography can image crustal discontinuities with a similar resolution to that of controlled-source tomography and receiver function analysis.

Moreover, we probe depths as large as 200 km covering almost the whole lithosphere thanks to long raypaths ($>$ 1500 km) and long-duration noise records for most of the long raypaths. The resulting uppermost mantle structure is in good agreement with earthquake-based tomographic results.

We propose to consider our two models as new reference models of the European crust and uppermost mantle. Our probabilistic model provides probability estimates for layer boundary depths that are potentially of great use in crustal structure studies and geological interpretations, including Moho depth investigations in regions with insufficient station coverage for receiver function analysis. Our final model, which provides a single S-wave velocity at each location is suitable for further geophysical studies including waveform modeling and full-waveform inversion. Both models will be distributed on the authors' website `https://sites.google.com/view/seismology-yanglu`.

3.2.7 Supplementary material

3.2.7.1 Cross-correlation functions

Fig. 3.12 shows the histogram of the number of months used to obtain the stacked cross-correlation functions. A large part of the cross-correlation dataset is obtained by stacking over less than 16 months. This results mainly from stations not operated simultaneously, in particular for pairs including temporary stations.

Fig. 3.4 shows cross-correlation functions computed for station CH.DAVOX in the 10-20 s and 40-80 s period bands. In addition, Fig. 3.13 shows cross-correlation functions in the 20-40 s and 80-150 s period bands. Fig. 3.13 documents the clear emergence of Rayleigh wave signals in the 80-150 s period band, therefore showing that we can extend our time-frequency analysis and subsequent tomographic study to such long periods.

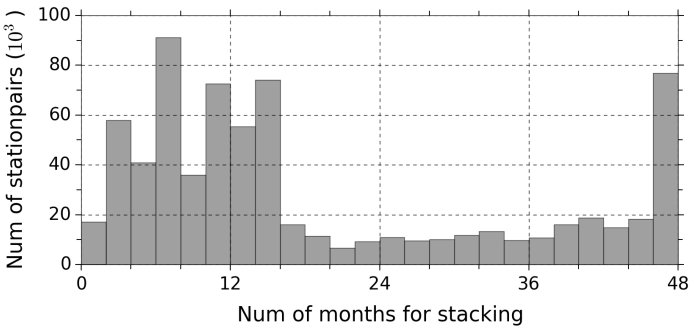

FIGURE 3.12 – Histogram of the number of months used to compute the stacked correlations.

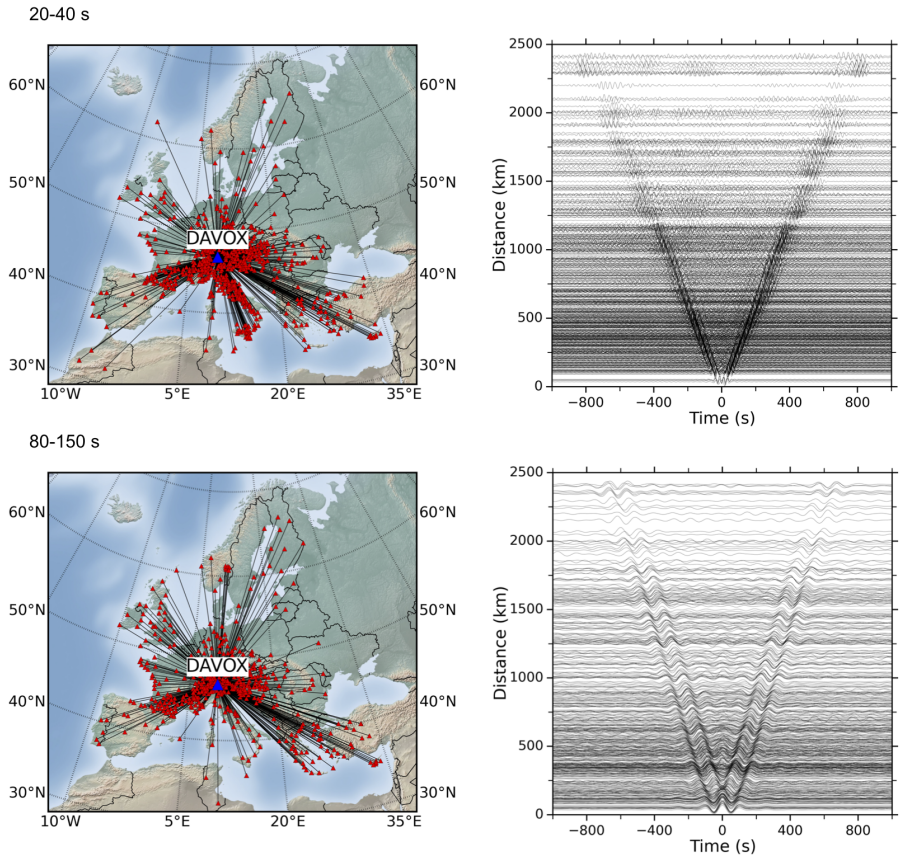

FIGURE 3.13 – Stacked cross-correlation functions for station pairs including station CH.DAVOX in the period bands 20-40 s (top) and 80-150 s (bottom).

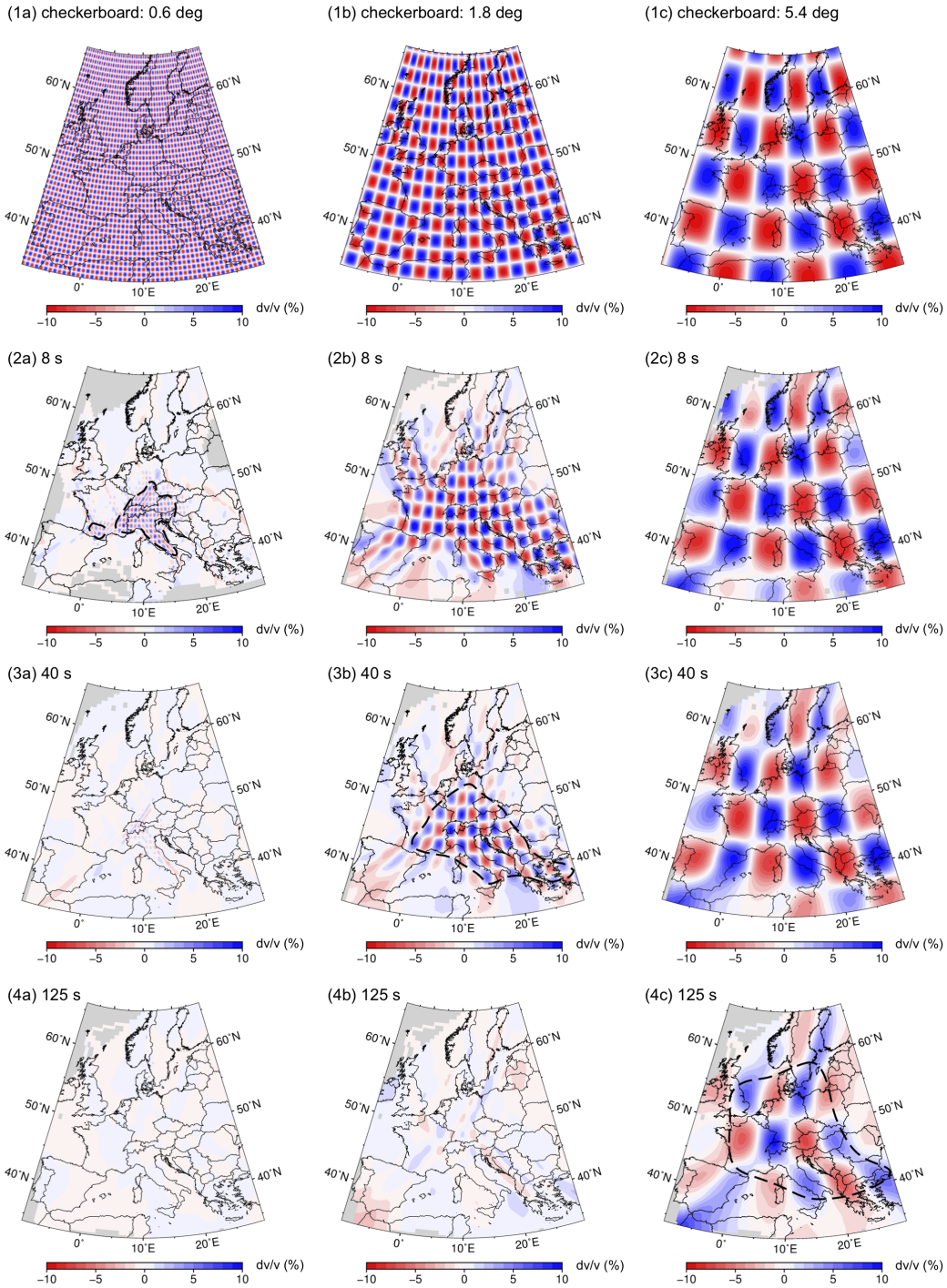
(1a) checkerboard: 0.6 deg
(1b) checkerboard: 1.8 deg
(1c) checkerboard: 5.4 deg
(2a) 8 s
(2b) 8 s
(2c) 8 s
(3a) 40 s
(3b) 40 s
(3c) 40 s
(4a) 125 s
(4b) 125 s
(4c) 125 s
60°N
50°N
40°N
0°
10°E
20°E
−10 −5 0 5 10
dv/v (%)

FIGURE 3.14 *(previous page)* – Resolution assessment of group velocity maps using multi-scale checkerboard tests. (1a-c) input models with velocity anomalies of size 0.6°, 1.8° and 5.4° ; (2a-c) outputs for period 8 s ; (3a-c) outputs for period 40 s ; (4a-c) outputs for period 125 s. The black dashed lines in Figs. 2a, 3b, 4c enclose areas with resolution better than 0.6°, 1.8° and 5.4° at 8, 40 and 125 s respectively.

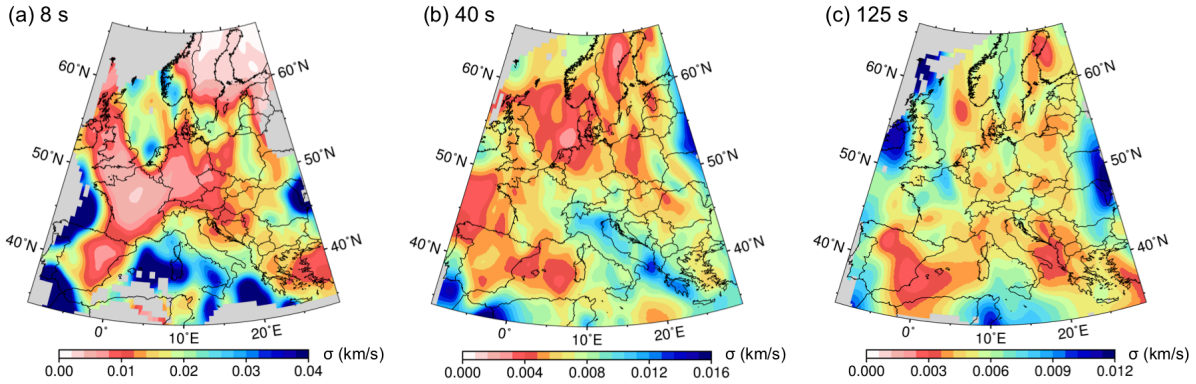

FIGURE 3.15 – Uncertainty assessments of inversion for group velocity maps using Jackknifing tests at periods 8, 40 and 125 s. Arbitrarily selected 80 % of the original data are used to invert for group velocity maps. This procedure is iterated 30 times. Standard deviations of the ensemble of results are plotted to document the inversion uncertainty. The analysis of results should be limited to the area well sampled by data, which means simultaneously good data coverage and good data azimuthal distribution.

3.2.7.2 Resolution evaluation : Checkerboard tests

We evaluate the resolution of the 2-D group velocity maps using checkerboard tests (Boschi and Dziewonski, 1999; Spakman and Wortel, 2004). For each period, we use multi-scale checkerboard models that include alternating velocity anomalies with amplitudes of ±10% of the background velocity. Synthetic Rayleigh wave travel times are computed assuming they travel along the great circle path connecting each pair of station. To simulate measurement errors, we add gaussian noise with standard deviation of 5 percent of the synthetic Rayleigh wave travel times. The synthetic travel times are inverted using the same parameterization and regularization as for the observational data.

Fig. 3.14 shows the results of the checkerboard tests for group velocity maps at periods 8, 40 and 125 s using anomalies of size 0.6°, 1.8° and 5.4°. At each period, the best resolution is achieved in the Alpine region. Towards peripheral areas, the resolution degrades and the smearing increases due to lower path density and uneven azimuthal

distribution. The resolution depends on the period : at 125 s, velocity anomalies of 5.4° are recovered, whereas velocity anomalies of 0.6° can be reconstructed in the Alpine and Apennines regions at 8 s. To interpret our 2-D group velocity maps, we define the areas with a resolution of at most 0.6°, 1.8° and 5.4° as the well-resolved areas for period 8, 40 and 125 s respectively. However, the resolution estimate using these three anomaly sizes is rather conservative. Checkerboard tests using smaller anomaly sizes show that the resolution of group velocity maps in the Alpine region reaches 0.3° at 8 s, 0.9° at 40 s, and 2.7° at 125 s.

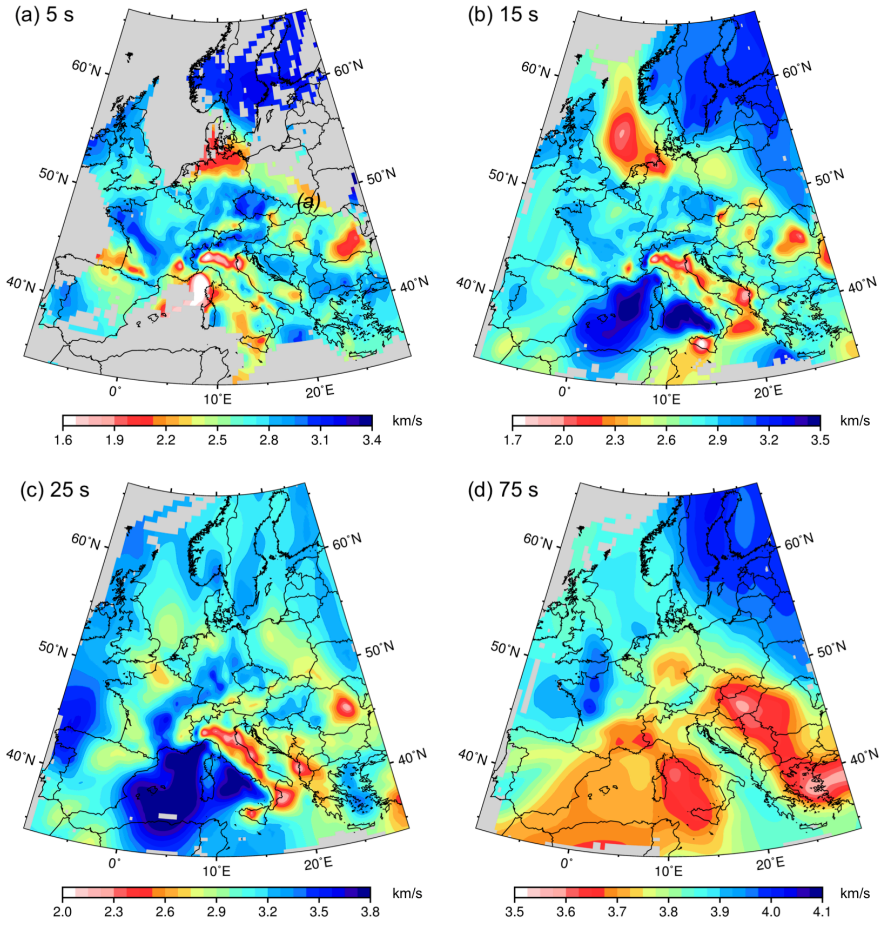

FIGURE 3.16 – Group velocity maps at periods 5, 15, 25 and 75 s. We plot only cells crossed by more than 10 paths.

3.2.7.3 Uncertainty assessment : Jackknifing tests

We evaluate the uncertainty of the 2-D group velocity maps using Jackknifing tests. The Jackknifing tests repeat inversions using arbitrary subsets of real data and analyze statistics of the ensemble of results (Gung and Romanowicz, 2004; Rawlinson et al., 2014). The standard deviation of the ensemble is often used to estimate the inversion uncertainty. Fig. 3.15 presents the results of Jackknifing tests for inversions at representative periods of 8, 40 and 125 s. Large areas of the study region display good stability with standard deviations smaller than 0.03 km.s^{-1}.

3.2.7.4 Group velocity maps

Fig. 3.7 shows group velocity maps at representative periods 8, 40 and 125 s. Fig. 3.16 shows additional group velocity maps at periods 5, 15, 25 and 75 s.

3.2.7.5 Inversion misfit

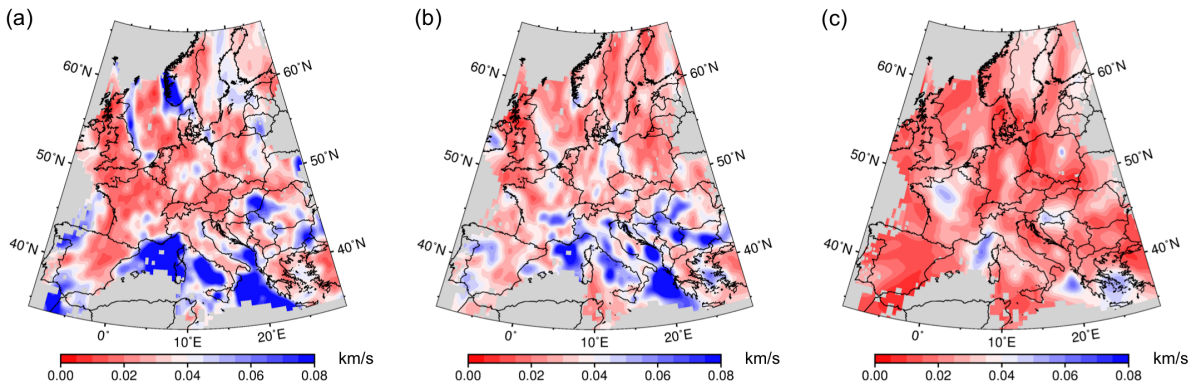

FIGURE 3.17 – Rms errors of inversion results for period bands 5-15 s (a), 15-55 s (b) and 55-150 s (c). We plot only cells with more than 10 crossing paths at 8 s.

For each cell, we calculate the rms error between the observed local dispersion curve and the dispersion curve predicted from the final Vs model. The rms error in a given period band provides a rough estimate of the reliability of the inversion in the depth range with the strongest sensitivity to that period band. Fig. 3.17 shows rms errors in period bands 5-15 s, 15-55 s and 55-150 s. Large errors are mainly observed in areas with poor path coverage, hence low-quality local dispersion curves. Accordingly, we avoid interpreting our results in areas with large errors at depths 10 km (5-15 s), 30 km (15-55 s), and 150 km (55-150 s) (see section 3.2.4.5, and Fig. 3.9). Besides, we ignore areas

with large errors in the period band 15-55 s for Moho depth estimate (see section 3.2.5.1, and Fig. 3.10).

3.2.7.6 Depth slices in the final Vs model

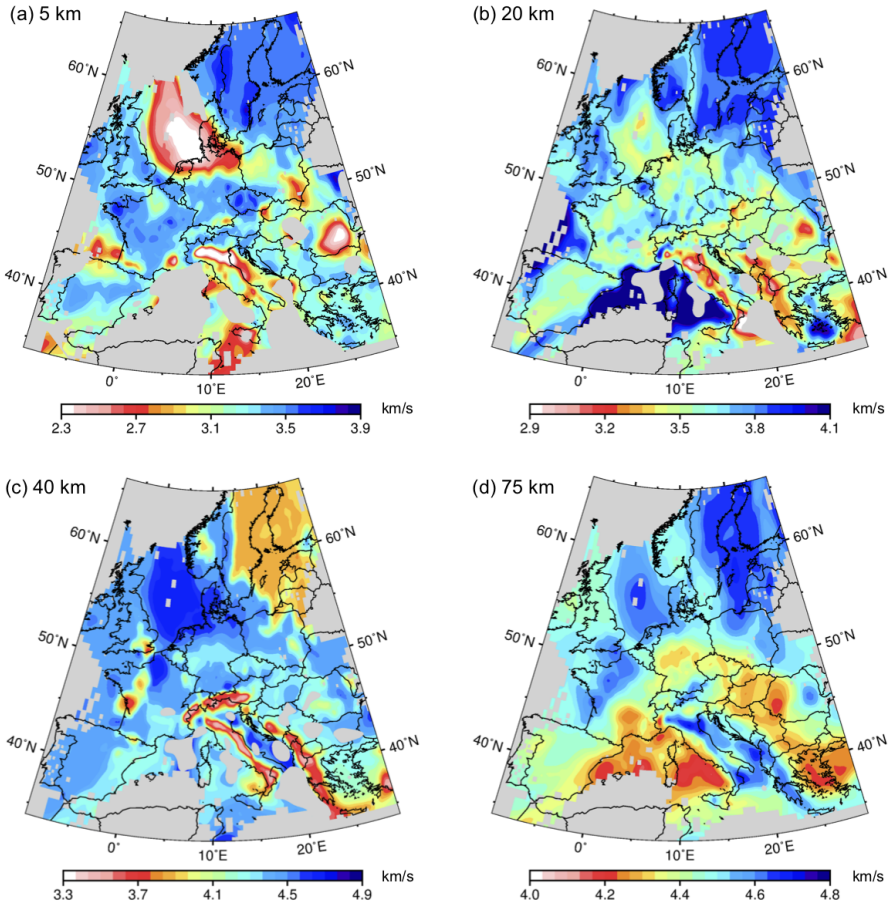

FIGURE 3.18 – Depth slices in the final Vs model at 5, 20, 40 and 75 km. We plot only cells crossed by more than 10 paths at 8 s period. Moreover, we discard cells with rms error greater than 0.06 km.s^{-1} (see Fig. 3.17).

Fig. 3.9 shows depth slices in the final Vs model at representative depths 10, 30 and 150 km. In Fig. 3.18, we provide additional slices at 5, 20, 40 and 75 km depth.

3.2.7.7 3-D view of the Bayesian Moho depth map

In Fig. 3.19, we provide 3-D views of the Bayesian Moho depth map (shown in Fig. 3.10d) that emphasize its strong and rapid lateral changes.

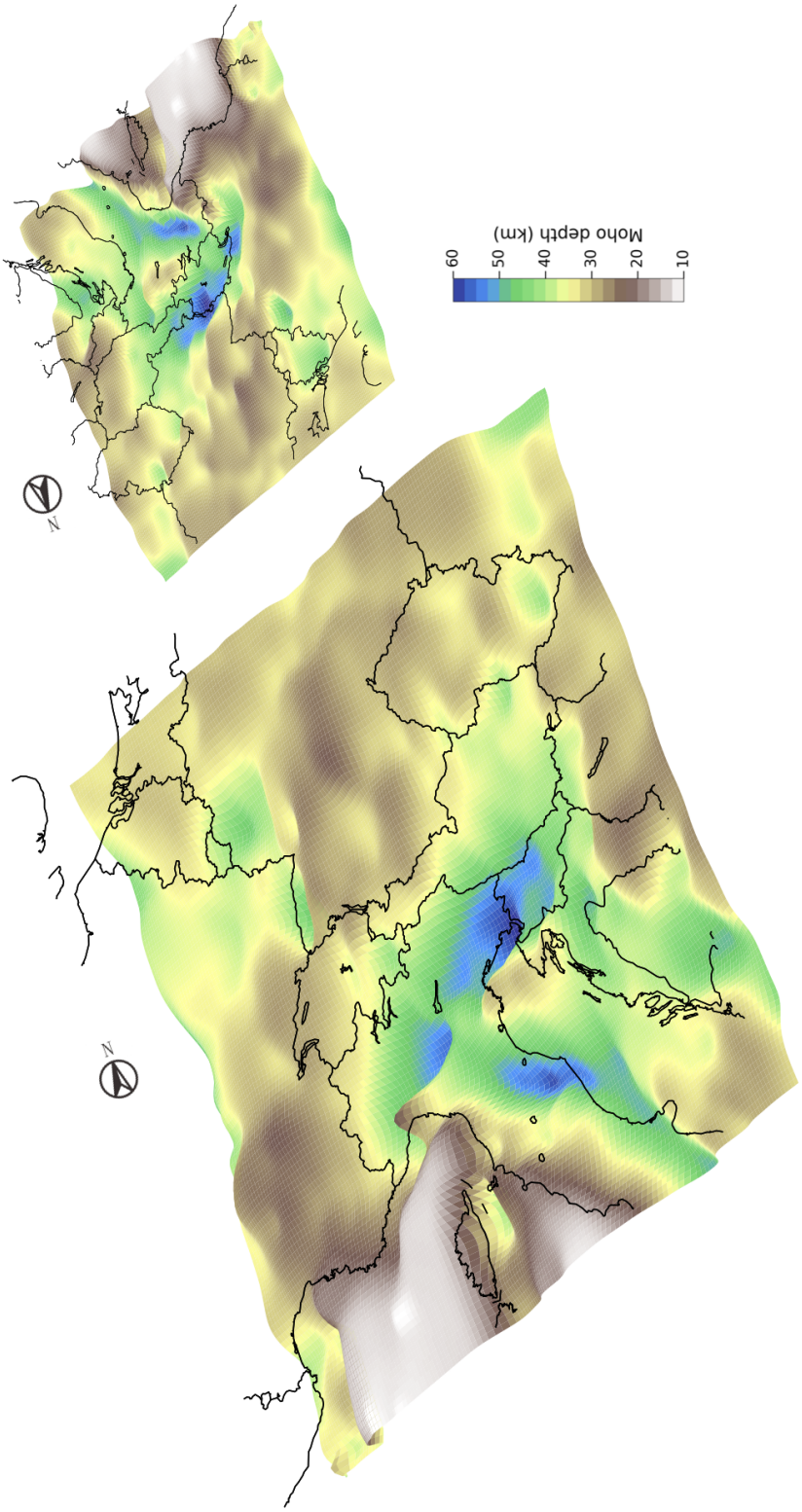

FIGURE 3.19 – 3-D views of the Bayesian Moho depth map in the greater Alpine region (map view in Fig. 3.10d)

3.2.8 Additional figures on the cross-correlation dataset

3.2.8.1 Body waves

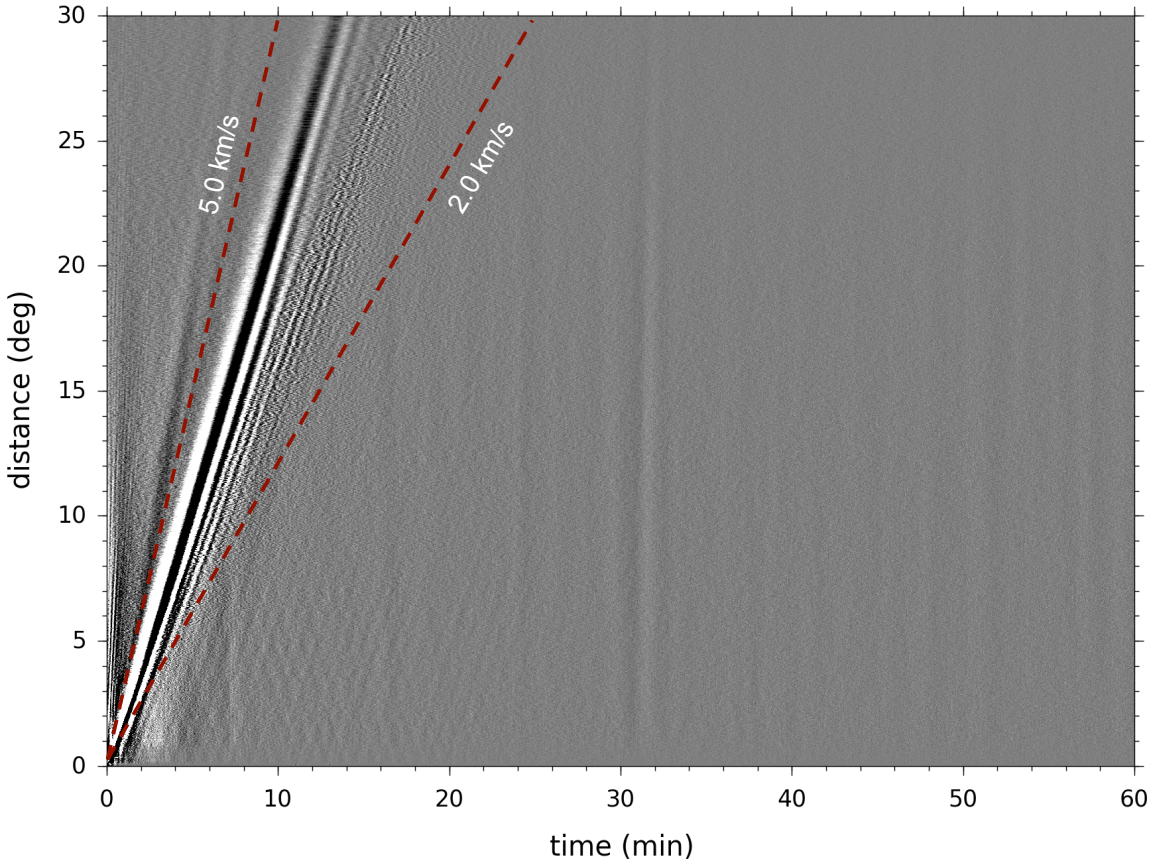

FIGURE 3.20 – Plot of binned cross-correlation functions sorted by inter-station distances. The binned cross-correlation functions refer to the causal and time-reversed acausal sides of cross-correlation functions stacked over bins of 2 km and filtered between 5-150 s.

We showed cross-correlation functions using station pairs including station DAVOX in Fig. 3.4 and Fig. 3.13. A clear emergence of Rayleigh waves can be observed in different period bands from 10 s to 150 s. In addition, we give a global view of all the cross-correlation functions in Fig. 3.20. We plot the causal and time-reversed acausal sides of all the cross-correlation functions filtered between 5 s - 150 s, stacked over bins of 2 km and sorted by inter-station distance. Still, we observe very clear dispersive Rayleigh waves, traveling with velocities between 2.0 and 5.0 km/s (red dashed lines in Fig. 3.20).

Besides, body waves can be observed as well. In Fig. 3.21, we muted the dominant Rayleigh waves to enhance other less energetic phases. We can see P-waves arriving

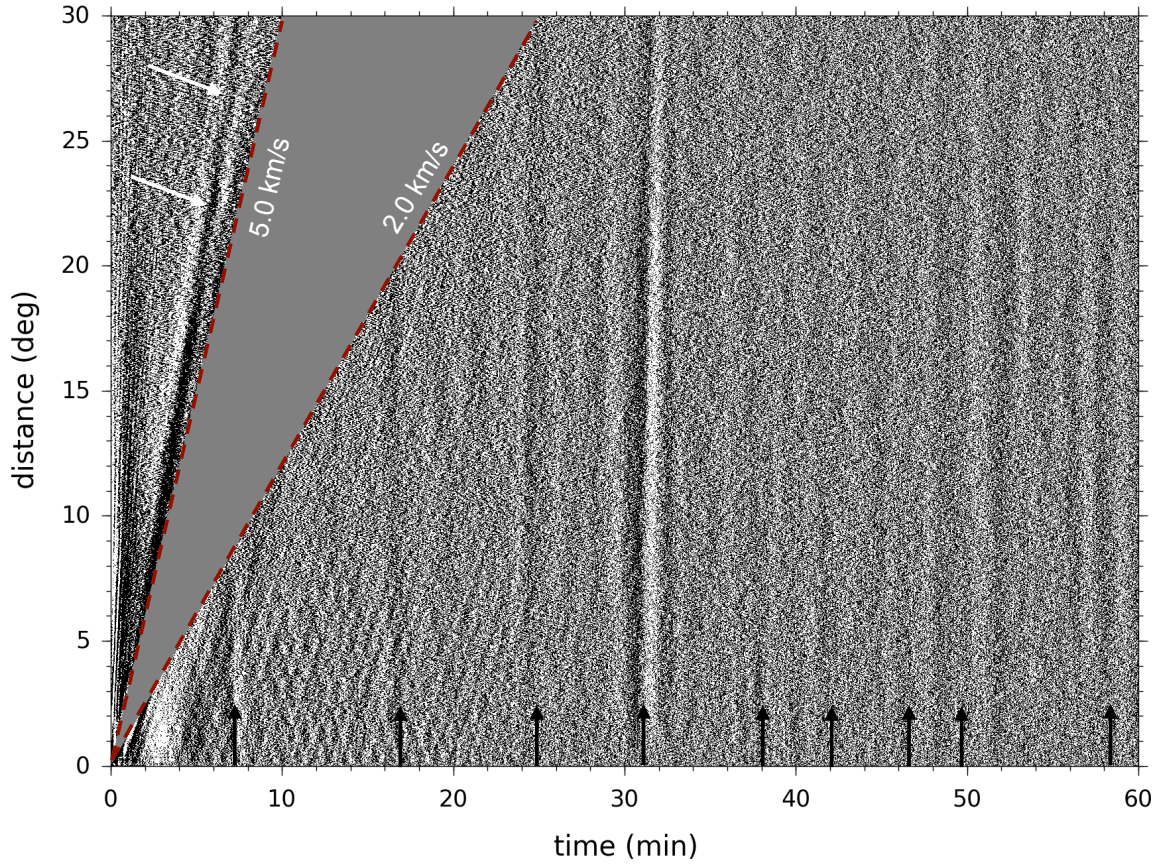

FIGURE 3.21 – Plot of binned cross-correlation functions sorted by inter-station distances. The binned cross-correlation functions refer to the causal and time-reversed acausal sides of cross-correlation functions stacked over bins of 2 km and filtered between 5-150 s. The surface waves are muted (between the two red dashed lines). White arrows indicate P-waves, and black arrows indicate deep reflection phases.

before the Rayleigh waves with velocities around 7 $km.s^{-1}$ (indicated by white arrows). The later arriving phases can be deep reflected body waves (indicated by black arrows). For instance, the phases arrived around 17 min might be the shear-waves reflected on the outer core (ScS). Thus, our cross-correlation dataset is also of potential use of body wave and deep earth imaging.

3.2.8.2 Azimuthal SNR distribution

Fig. 3.22 shows the azimuthal distribution of signal-to-noise ratio (SNR) for our cross-correlation dataset. The signal-to-noise ratios for the causal and acausal sides of all the cross-correlation functions are sorted by their azimuths, and averaged over bins of 15° at

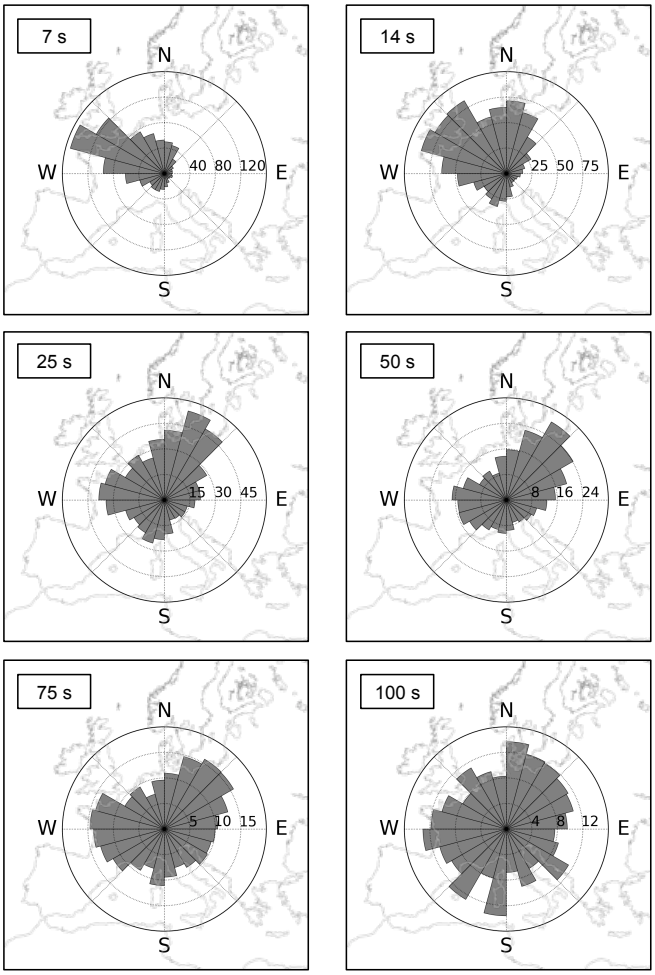

FIGURE 3.22 – Azimuthal distribution of signal-to-noise ratio at representative periods. We plot signal-to-noise ratios averaged over bins of 15° for the causal and time-reversed acausal sides of all the cross-correlation functions. 7 s and 14 s correspond to the secondary and primary microseism.

representative periods. At each period, the obtained azimuthal distribution of signal-to noise ratio roughly depicts the distribution of noise source energy at that period.

Noise sources at 7 s and 14 s (secondary and primary microseisms peak) are the most energetic. At these periods, noise sources are dominated by microseisms related to the oceanic activities (Longuet-Higgins, 1950; Hasselmann, 1963). The secondary microseism is produced by the nonlinear interference of wave trains propagating in opposing directions at nearby coastlines, while the primary microseism is generated by the interaction of ocean waves with sea bottom topography in deep waters (Stehly et al., 2006; Tian and Ritzwoller, 2015). At 7 s, we observe a very strong directivity of incoming noise energy

from the North-West, corresponding to the strong noise source of the North Atlantic ocean (Kedar et al., 2008; Hillers et al., 2012). At 14 s, strong energy comes from the North-West and also from other directions of coastal areas, such as the North (North Sea and Baltic Sea), the South (Mediterranean Sea), and the South-West (Iberian peninsula). On the contrary, very weak energy is detected at both periods from the East, which is the direction of continental area. At 25 s and 50 s, we observe two dominant energy arrival directions, the West and the North-East. Compared with shorter periods, the directivity of noise source energy distribution is less strong. At 75 s and 100 s, the noise source energy distribution becomes isotropic. This can be explained by the global hum as the dominant noise source at these periods, and the global propagation contributes to both the causal and acausal sides of the cross-correlation functions. In summary, the noise sources are energetic and anisotropic at short periods, while they are less energetic and more isotropic at longer periods. The observations are in agreements with those of Pedersen and Krüger (2007); Yang and Ritzwoller (2008) for Europe.

Chapitre 4

Ambient noise phase velocity tomography

Sommaire

4.1 Introduction

In this chapter, we present two ambient noise tomographic studies based on Rayleigh waves phase velocity measurements. We use the same cross-correlation dataset as in the ambient noise group velocity tomography in chapter 3. Following Ekström et al. (2009), we measure Rayleigh waves phase velocities from the spectral domain cross-correlations in the period range 5-150 s.

The measured phase velocities are first inverted in the same manner as in the group velocity tomography. We obtain a series of 2-D Rayleigh waves phase velocity maps and

a final 3-D shear-wave velocity model of the European crust and uppermost mantle. Besides, benefiting from the dense seismic station array in the Alpine region, we also perform the Eikonal tomography adopting the approach proposed by Lin et al. (2009). We construct Rayleigh waves phase velocity isotropic maps and azimuthal anisotropy maps at discrete periods between 7 and 25 s for the Alpine region.

Although the Rayleigh wave group and phase velocities provide coherent information, we perform these additional phase velocity tomographic studies for the following reasons : (1) we measure the group and phase velocities using two independent methods. Thus, the tomographic results obtained from the group and phase velocity measurements can be used to confirm each other ; (2) the Eikonal tomography provides useful supplementary information on the phase velocity azimuthal anisotropy.

4.2 Phase velocity measurement

In ambient noise tomography, surface wave phase velocities are often estimated from the time domain cross-correlations. Phase velocities can be estimated using the two-station method (Bloch and Hales, 1968; Landisman et al., 1969), which is the most classical way in the earthquake-based surface wave tomography. Bensen et al. (2007) proposed to derive the phase velocities from the integral of the group velocity dispersion curve.

Nonetheless, we notice that the two methods are limited in the following aspects. The two-station method requires that the source and two receiver stations roughly locate along a great circle. Using the method of Bensen et al. (2007), the derived phase velocities are not independent measurements from the group velocities. Moreover, the two methods measuring phase velocities from the time domain cross-correlations should obey the far-field approximation of surface waves. Thus, the phase velocities can only be measured for station pairs with inter-station distance larger than 3 wavelengths as suggested by Bensen et al. (2007).

In our study, we measure phase velocities from the frequency domain cross-correlations following the approach proposed by Ekström et al. (2009). The approach is based on Aki's original formulation for the cross-correlation of stochastic wavefields. We remind the formulation shown in equation 2.5 :

$$C_(\vec{r}_1, \vec{r}_2; w) = R\left\{C_(\vec{r}_1, \vec{r}_2; w)\right\} \quad = J_0(k(w)r) = J_0(\frac{w}{c(w)}r), \tag{4.1}$$

where $R\{\}$ refers to the real part of the normalized cross spectrum $C_(\vec{r}_1, \vec{r}_2; w)$ for two receivers located at positions $\vec{r}_1$ and $\vec{r}_2$, J_0 denotes a Bessel function of first kind and order 0, $k(w)$ is the wavenumber, w is the angular frequency, $c(w)$ is the frequency-dependent phase velocity of the medium and $r = |\vec{r}_1 - \vec{r'}_2|$ is the distance between the two receivers.

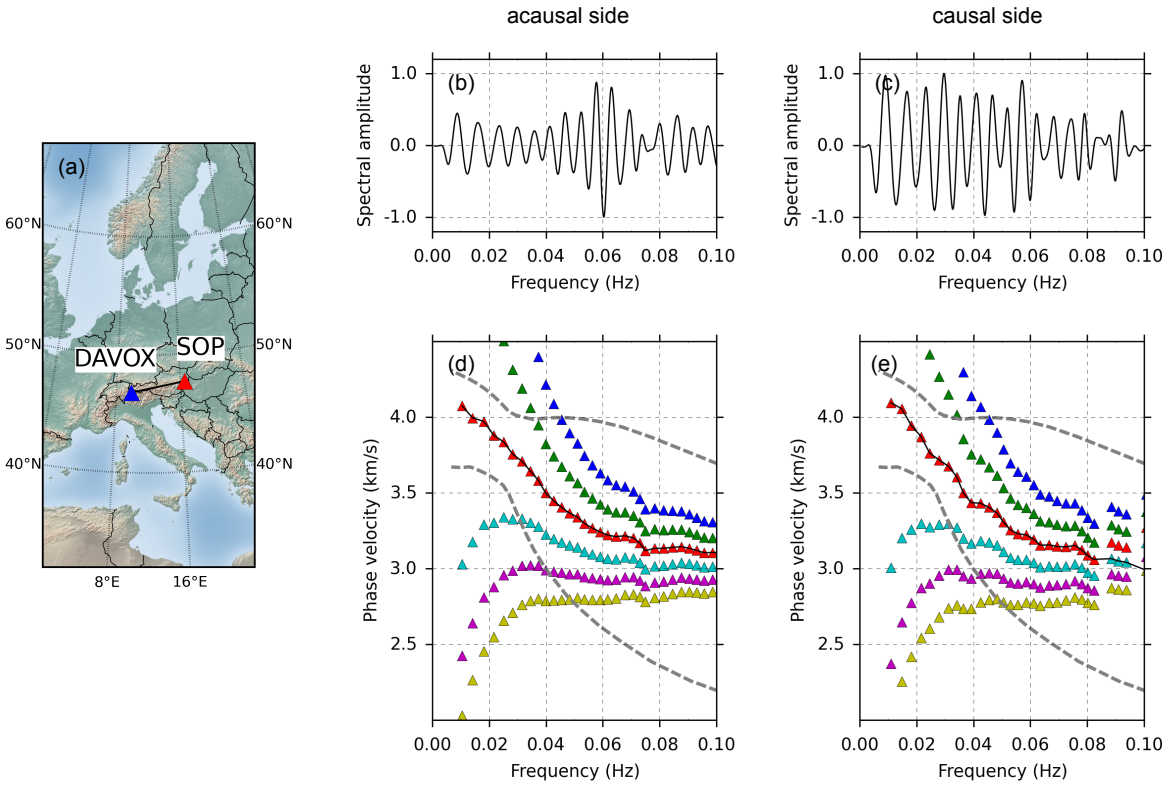

FIGURE 4.1 – Phase velocity measurements for station pair DAVOX-SOP. (a) Location map ; (b-c) Real parts of the acausal and causal sides of the cross spectrum ; (d-e) Colored triangles indicate the calculated possible phase velocities at each zero-crossing frequency in (b) according to equation 4.2, where colors blue, green, red, cyan, purple correspond respectively to $m = -2, -1, 0, 1, 2$. Two dashed grey lines refer to the minimum and maximum limits of phase velocity selection. Black lines show the selected phase velocities for the acausal and causal sides of cross-correlation.

The formulation states that, in the case of stochastic wavefields, the imaginary part of the frequency domain cross-correlation diminished and its real part can be expressed as a Bessel function related to the phase velocity. In other words, the phase velocity can be directly derived from the real part of the frequency domain cross-correlation.

The formulation is derived assuming stochastic wavefields generated by isotropic illumination of uncorrelated plane waves. Such strong assumptions made are far from real environments in the Earth. However, the anisotropic illumination of noise sources mainly influence the amplitude of cross-correlation spectrum, rather than the locations of zero-crossing frequencies (Ekström et al., 2009). Thus, we choose to derive phase velocities only at these zero-crossing frequencies of the cross-correlation spectrum. For the nth zero-crossing frequency w_n, the phase velocity is given by

$$c(w_n) = \frac{w_n r}{z_{n+m}}, \tag{4.2}$$

where z_{n+m} is the $(n+m)$th zero-crossing value of the Bessel function J_0, and $m = 0, \pm 1, \pm 2, ...$ account for the missed or extra zero-crossings in the real observations.

The phase velocity measurements, performed between station pairs, have no strict requirements of seismic station geometry. The measured phase velocities are independent measurements from the group velocities. By using the frequency domain cross-correlation, the approach avoids the limitation of far-field approximation of the time domain methods. To provide reliable phase velocity measurement, only one wavelength is required for the inter-station distance. Boschi et al. (2013) confirm the approach by comparing more than 1,000 phase velocity measurements with those estimated by the two-station approach.

In practice, we measure the phase velocities on both causal and acausal sides of the cross-correlation. For each side, we first compute the real part of cross spectrum. At each zero-crossing frequency of the cross spectrum, we calculate a series of possible phase velocities according to equation 4.2 for different choices of m. At the low frequency end, we determine the choice of phase velocities using the minimum and maximum limits of plausible phase velocities. The limits are given by the upper and lower boundaries of synthetic phase velocity dispersion curves computed using all the 1-D models derived from our ambient noise group velocity tomography. Towards higher frequencies, we select phase velocities by checking the continuity of the phase velocity dispersion curve. As an example, Fig. 4.1 shows the phase velocities measured on the causal and acausal sides of the cross-correlation between DAVOX and SOP.

Period (s)	7	25	75	150
Measurements	28,603	59,532	27,246	4,598

TABLE 4.1 – Number of phase velocity measurements.

In each side of the cross-correlation, the measured phase velocities are interpolated at regularly spaced periods. The interpolated phase velocity measurements on the two sides are further selected. At each period, the phase velocity measurements are kept only if : (1) signal-to-noise ratios of both sides are larger than 3 ; (2) phase velocity difference between the two sides are smaller than 0.2 km/s. Finally, the kept phase velocity measurements are averaged over the two sides to obtain the final measurements. Table 4.1 presents the number of phase velocity measurements at representative periods, which is approximately 1/4-1/3 of that of group velocity measurements.

4.3 Phase velocity tomography of the European crust and uppermost mantle

4.3.1 Method

The goal of this section is to derive a 3-D shear-wave velocity model for the European crust and uppermost mantle, using Rayleigh waves phase velocities measured from cross-correlations of ambient seismic noise in the period range 5-150 s. To that end, we apply the two-step surface wave inversion approach as in the group velocity tomography in chapter 3.

In the first step, period-dependent Rayleigh waves phase velocity maps are estimated following a linearized inversion algorithm proposed by Boschi and Dziewonski (1999) using the great-circle assumption of ray path. The phase velocity measurements are inverted on an adaptive grid using square cells of sizes 0.6°, 0.3°, 0.15° depending on the data density. The inversion is stabilized using roughness regularization, and the regularization coefficient is determined by the 'L-curve' analysis (Hansen, 2001).

In the second step, we extract a local phase velocity dispersion curve in each cell from the phase velocity maps derived in the first step. Each local phase dispersion curve is inverted to obtain a 1-D shear-wave velocity model, which together form a 3-D shear-wave velocity model. To invert for the 1-D model, we use a two-step data-driven inversion algorithm : a probabilistic model is first built using a Bayesian inversion approach, followed by a linearized inversion to better constrain the velocity in the uppermost mantle (Lu et al., 2018).

4.3.2 Phase velocity maps

In Fig. 4.2, we chose to show Rayleigh waves phase velocity maps at representative periods 7, 25, and 75 s. As shown in Fig. 4.2d, the Rayleigh waves phase velocity is sensitive to larger depth than the group velocity at the same period. Rayleigh waves phase velocities at 7, 25, and 75 s are sensitive to similar depths as group velocities at 8, 40 and 125 s, accordingly, phase velocity maps provide similar information as group velocity maps at corresponding periods (see Fig. 3.9 for group velocity maps in section 3.2.3.3).

At 7 s, Rayleigh wave phase velocities are mostly sensitive to structure of upper crust ($\sim$7 km). The low velocity anomalies are related to sedimentary basins such as the North Sea basin, the Po plain, the Pannonian basin and the Moesian platform, where the Po plain is the most striking feature with phase velocity as low as 2 km/s. The high velocity anomalies characterize orogenic mountain belts like the Alps, and Variscan massifs like the Bohemian Massif. At 25 s, Rayleigh wave phase velocities are mostly sensitive to depth $\sim$ 28 km. Thus, we observe low velocity anomalies along the mountain belts such as the Alps, the Apennines and the Hellenides, as a result of their deep crustal roots. At

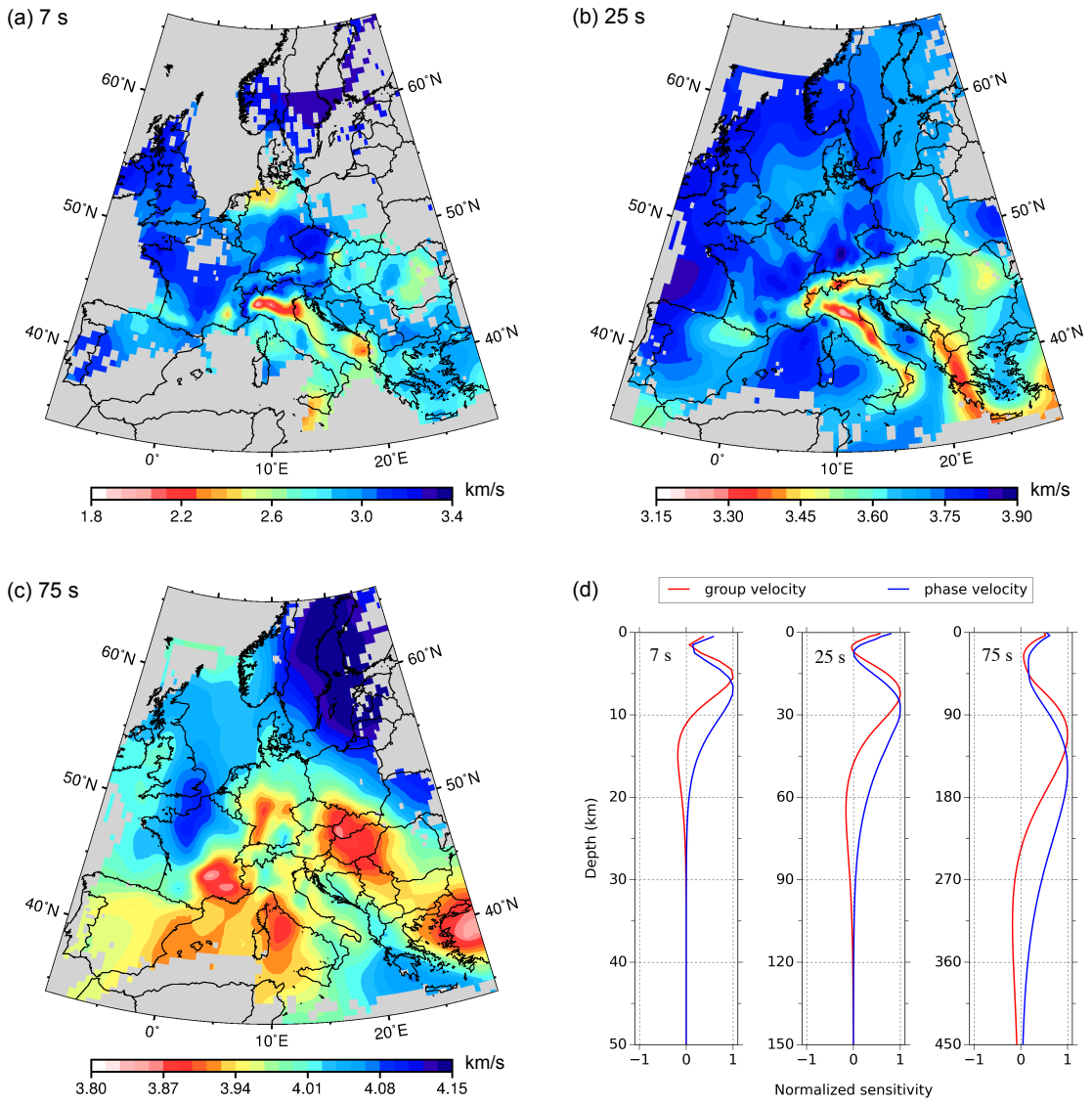

FIGURE 4.2 – Phase velocity maps at representative periods 7, 25, and 75 s. We plot only cells crossed by more than 10 paths. In (d), we show the normalized depth sensitivity kernels to Vs for Rayleigh wave group and phase velocities at the three periods, which are computed using the average Vs model in *LSP_Eucrust*1.0 (Lu et al., 2018).

75 s, Rayleigh wave phase velocities have their dominant sensitivities at a depth $\sim$ 150 km. We image the Trans-European Suture Zone (TESZ), marking the transition from the low-velocity West-European platform to the high-velocity lithosphere of the Eastern Europe Craton (EEC).

4.3.3 3-D shear-wave velocity model

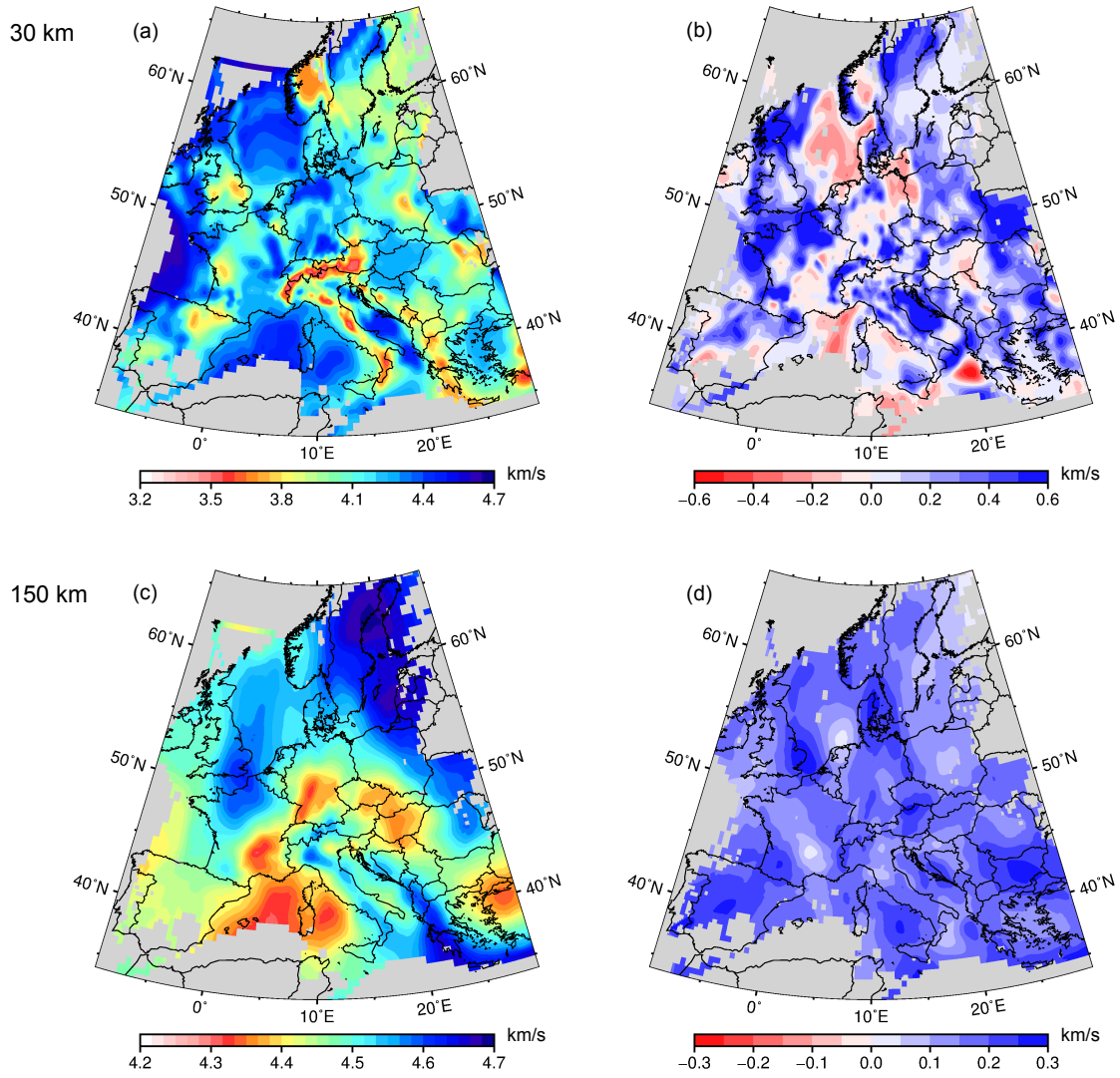

FIGURE 4.3 – Depth slices at 30 km (a) and 150 km (c) in the final 3-D Vs model, and their differences from results derived by group velocity tomography (b,d).

In Fig. 4.3a,c, we present 2 depth slices at 30 and 150 km in the final 3-D Vs model. In general, the depth slices derived by the phase and group velocity tomography underline similar features (see Fig. 3.11 for depth slices derived from the group velocity tomography in section 3.2.4.5). The 30-km depth slice reflects the variation of crustal thickness. In the mountain belts of large crustal thickness, such as the Alps, the Apennines, the Dinarides and the Hellenides, we observe low velocities (<4.0 km/s) of the crust. In

the areas of stretched continental crust, such as the European Cenozoic Rift System and the Pannonian basin, we observe high velocities (>4.2 km/s) of the mantle. In the 150-km depth slice, high velocities are mainly associated to the Eastern Europe Craton and the subducted slabs surrounding the Adriatic plate, as well as the Anglo-Paris basin. Meanwhile, low velocities characterize a stripe beneath the European Cenozoic Rift System and another stripe from the Pannonian basin to Northwestern Anatolia.

However, as shown in Fig. 4.3b,d, we observe non-negligible differences of absolute Vs values between the the depth slices derived by the phase and group velocity tomography. In the 30-km depth slice, the maximum differences reach 0.5 km/s in some areas. In the 150-km depth slice, there exists a systematic shift of Vs value ∼0.2 km/s. These differences have several possible origins, such as : (1) the group and phase velocities are measured using two independent methods ; (2) the number of data in the phase velocity tomography is only 1/4-1/3 of that in the group velocity tomography, so that the parameterization and regularization in the 2-D velocity map inversions are different.

4.4 Eikonal tomography of the Alpine crust

4.4.1 Method

Surface wave tomography usually estimates group or phase velocity maps through linearized inversion of travel time measurements. It is often based on the great-circle assumption of ray path, and the regularization is applied to stabilize the inversion. Surface wave tomography can be performed in a different way, referred to as 'Eikonal tomography'. The method is initially proposed by Lin et al. (2009), and later generalized to 'Helmholtz tomography' by Lin and Ritzwoller (2011a). The basic idea of the method is to track the wavefronts of surface waves, and the local directional phase velocity is given by the gradient of traveltime fields, sampled by a dense seismic array.

In a lateral homogeneous medium, frequency-dependent surface wave propagation obeys the 2-D Helmholtz equation (Friederich et al., 2000) :

$$\frac{1}{c(w,\vec{r})^2} = |\nabla\tau(w,\vec{r})| - \frac{\Delta A(w,\vec{r})}{A(w,\vec{r})w^2}, \tag{4.3}$$

where $c(w,\vec{r})$ is the phase velocity of surface waves at position $\vec{r}$ and frequency w, $\nabla = \frac{\partial}{\partial x} + \frac{\partial}{\partial y}$ refers to the local gradient of phase travel time $\tau(w,\vec{r})$, and $\Delta = \frac{\partial^2}{\partial x^2} + \frac{\partial^2}{\partial y^2}$ denotes the Laplacian of the spectral amplitude of surface waves $A(w,\vec{r})$. The equation 4.3 reduces to the Eikonal equation by neglecting the second term under the high-frequency approximation :

$$\frac{1}{c(w,\vec{r})^2} = |\nabla\tau(w,\vec{r})|. \tag{4.4}$$

The Eikonal equation implies that the phase velocities and directions of wave propagation can be directly derived from the gradient of phase traveltime fields, and this equation is the essential theory of Eikonal tomography. Here, we choose to neglect the second term because : (1) the amplitude of surface waves measured from the cross-correlation of ambient seismic noise is poorly reliable because of its high sensitivity to the anisotropic noise source distribution and medium heterogeneity ; (2) in the Eikonal tomographic study of the western USA conducted by Lin et al. (2009) and Lin and Ritzwoller (2011b), they showed that the influence of the second term is limited. For instance, the difference in the Rayleigh wave isotropic phase velocity maps at 60 s derived from Eikonal tomography (equation 4.4) and Helmholtz tomography (equation 4.3) is less than 20 m/s in most areas in their studied region.

Eikonal tomography shows its advantages to traditional surface wave tomography in several aspects. It is a simple method to implement without inversion procedure, and there is no explicit regularization applied. The method accounts for bending rays, rather than assuming the great-circle of ray path. The misfit of phase velocity estimate can be easily calculated from the statistics of the ensemble of phase velocity estimates in each cell, while the misfit estimate in traditional methods is always complicated. It naturally provides the direction of phase velocity estimate, that can be used to analyze the azimuthal anisotropy.

However, Eikonal tomography requires large-aperture dense seismic array, so that the phase traveltime fields can be well constructed. Indeed, this strong requirement is the main obstacle limiting its applications. The quick increase of the number of seismic stations in the Alpine region, in particular with the AlpArray Seismic Network (AASN), provides us a unique chance to perform the Eikonal tomography in this region.

In this study, we apply Eikonal tomography using cross-correlations of ambient seismic noise from 483 stations in the alpine region. It mainly consists of three steps. In the first step, we compute the phase traveltime map for a given station selected as source station. Following Mordret et al. (2013), we interpolate phase traveltime measurements associated to the source station using a spline-in-tension interpolation scheme on a regular grid made of cells of 0.15°. We notice that these phase traveltime measurements are already selected by applying criteria like SNR and symmetry (see section 4.2). In the second step, we calculate the gradient of phase traveltime map. In each cell, the local phase velocity is approximated by the inverse of gradient, and the direction of phase velocity estimate (propagation direction of Rayleigh waves) is given by the direction of gradient. We discard cells with distances shorter than 4 wavelengths to the source station, as well as areas out of the convex of receiver station distribution, because of poor data coverage. As an example, Fig. 4.4 shows the first two steps performed for station FIESA. Step 1 and step 2 are iterated for each station, so we finally obtain an ensemble of directional phase velocity estimates for each cell. In the third step, we reject phase velocity estimates deviating more than two standard deviations from the mean value in each cell. The kept phase velocity estimates are averaged to form the final isotropic phase velocity map. The kept phase velocity estimates, combined with the corresponding directions, are used to

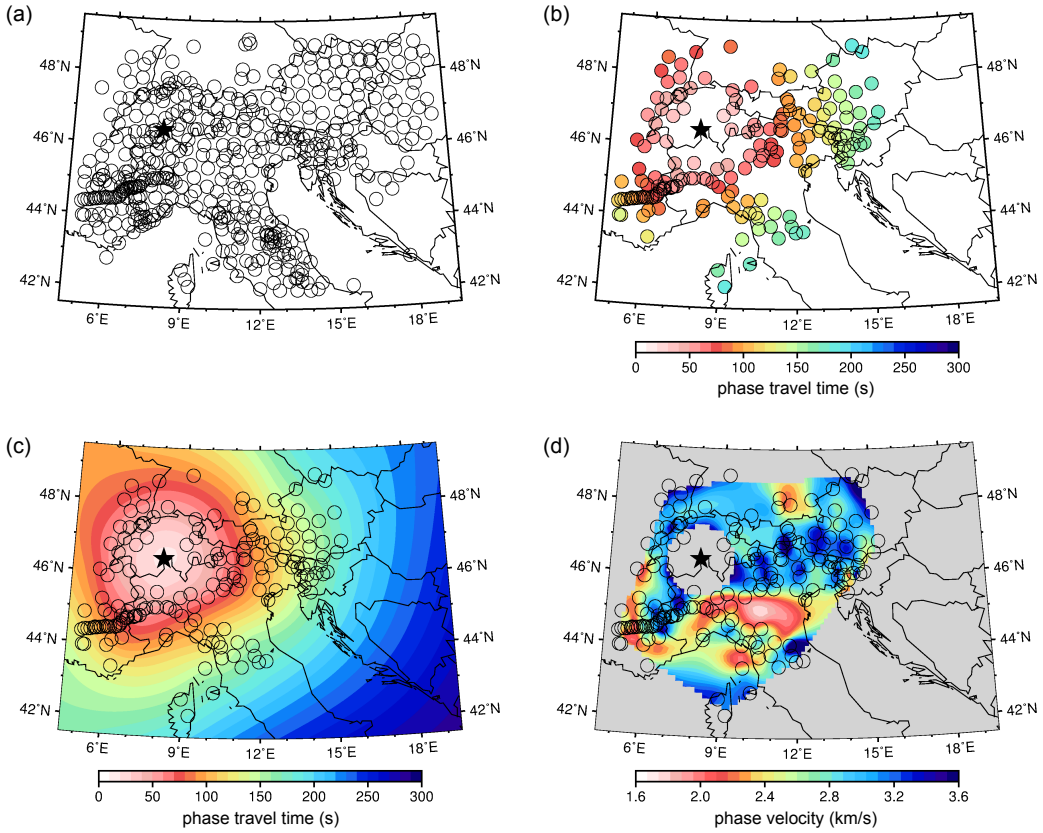

FIGURE 4.4 – Eikonal tomography method, example for a given source station FIESA at 7 s. (a) Location map for the source station FIESA (star) and 482 receiver stations (circles) ; (b) Available phase travel time measurements of Rayleigh waves between FIESA and receiver stations ; (c) Interpolated phase traveltime map ; (d) Phase velocities estimated as the inverse of the gradient of phase traveltime map. We discard cells with distances shorter than 4 wavelengths to the source station, as well as areas out of the convex of receiver station distribution. We observe low velocity anomalies in the Po plain and high velocity anomalies in the Alps.

derive the phase velocity azimuthal anisotropy maps.

4.4.2 Isotropic phase velocity maps

In Fig. 4.5, we show the final isotropic phase velocity maps derived from the Eikonal tomography at representative periods 7, 12, 18 and 25 s. We only display cells with more than 100 individual phase velocity estimates. The phase velocities at the four periods are mostly sensitive to depths ∼7, 13, 20 and 28 km, respectively. At 7 s, we observe

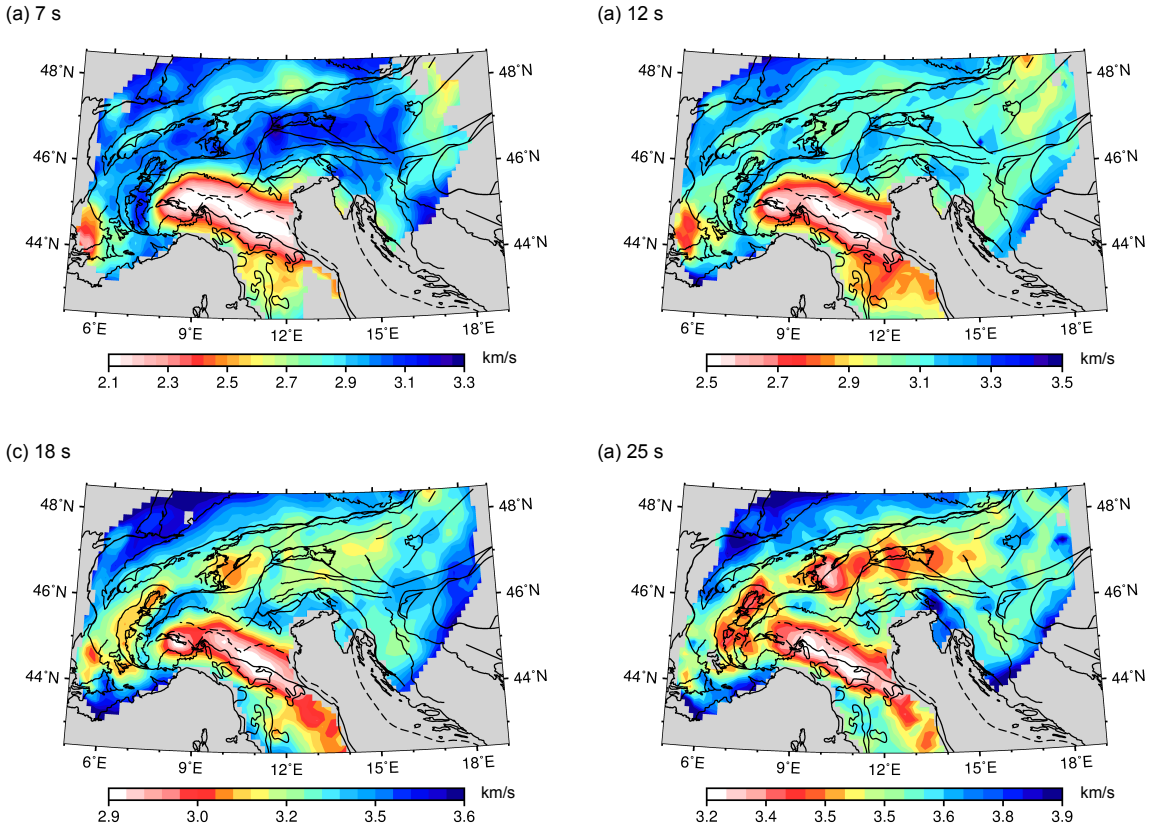

FIGURE 4.5 – Isotropic phase velocity at representative periods 7, 12, 18 and 25 s. We only plot cells with more than 100 individual phase velocity estimates on land. The black lines correspond to the geological and tectonic boundaries in the generalized tectonic map of the Alps shown in Fig. 4.8a.

high velocity anomalies induced by the Alps, and low velocity anomalies induced by the Po plain and the French South-East basin. At 12 s, we still see strong influence of the two deep sedimentary basins. At 18 and 25 s, the most striking features are low velocity anomalies associated with the thick crust of the Alps and the Apennines.

At each period, we evaluate the uncertainties of each final isotropic phase velocity map by the standard deviations of individual phase velocity estimates in each cell. The phase velocity maps at 7, 12, 18 and 25 s have uncertainties between 0.1-0.2 km/s in most areas (Fig. 4.6). At 7 and 12 s, large uncertainties are observed in the Western Alps and along the boundary of Po plain. A possible reason is that available phase traveltime measurements for interpolating individual phase traveltime maps are not sufficient dense and uniform to sample the areas of strong lateral velocity variation (see example in Fig. 4.4b). At all four periods, we also observe relativly large uncertainties in the Italian Peninsula,

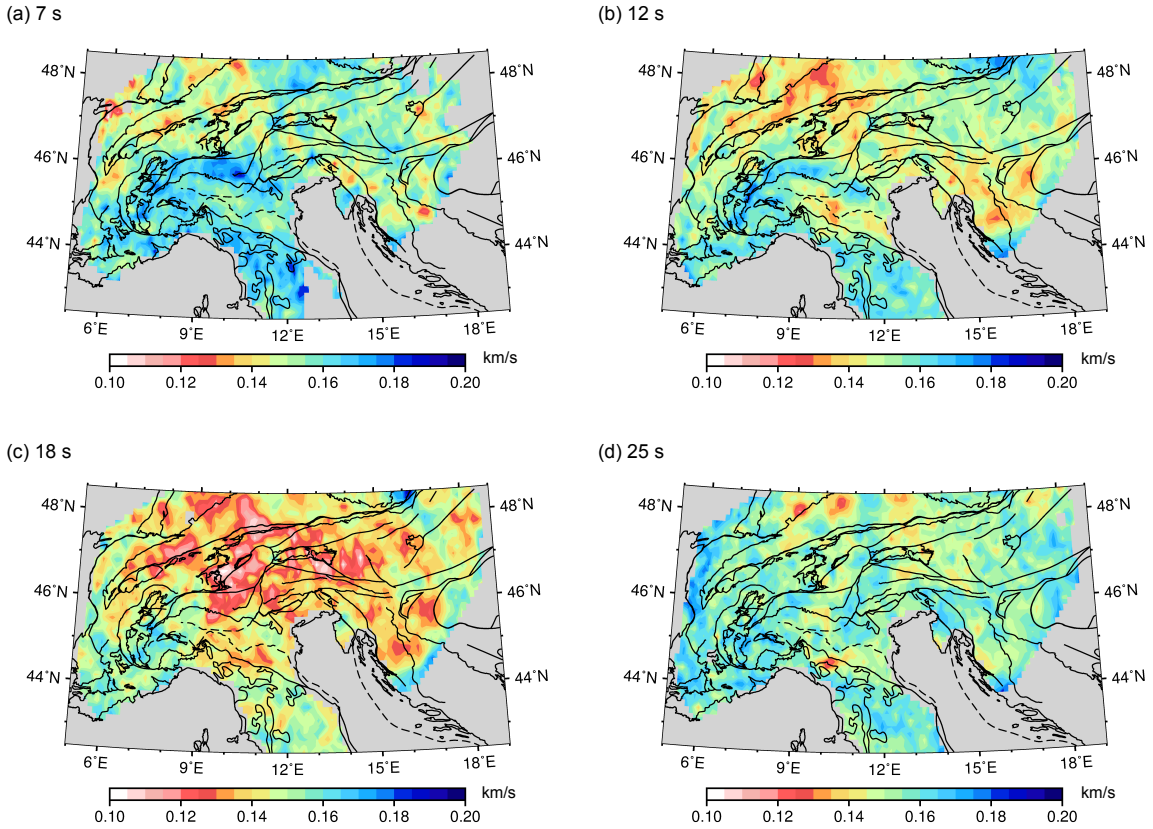

FIGURE 4.6 – Uncertainties of isotropic phase velocity maps at representative periods 7, 12, 18 and 25 s. We plot only cells with more than 100 individual phase velocity estimates on land. The black lines correspond to the geological and tectonic boundaries in the generalized tectonic map of the Alps shown in Fig. 4.8a.

which are due to the gaps of station distribution at sea. We limit our analysis to 25 s due to the increase of uncertainties compared to 18 s. This increase happens because we discard phase traveltime measurements and cells within 4 wavelengths to the source station in the first and second steps of Eikonal tomography (see example in Fig. 4.4b,d). As a consequence, we discard large areas at long periods, and the uncertainties increase accordingly.

In Fig. 4.7, we compare the isotropic phase velocity maps obtained from Eikonal tomography with the results of our phase velocity tomography of the European crust and uppermost mantle in section 4.3. At both periods 7 and 25 s, the isotropic phase velocity maps derived from the two tomographic methods show similar features, and differ in details with absolute velocity differences mostly between ± 0.2 km/s. The Eikonal tomography results in more patchy phase velocity maps, while those derived from the

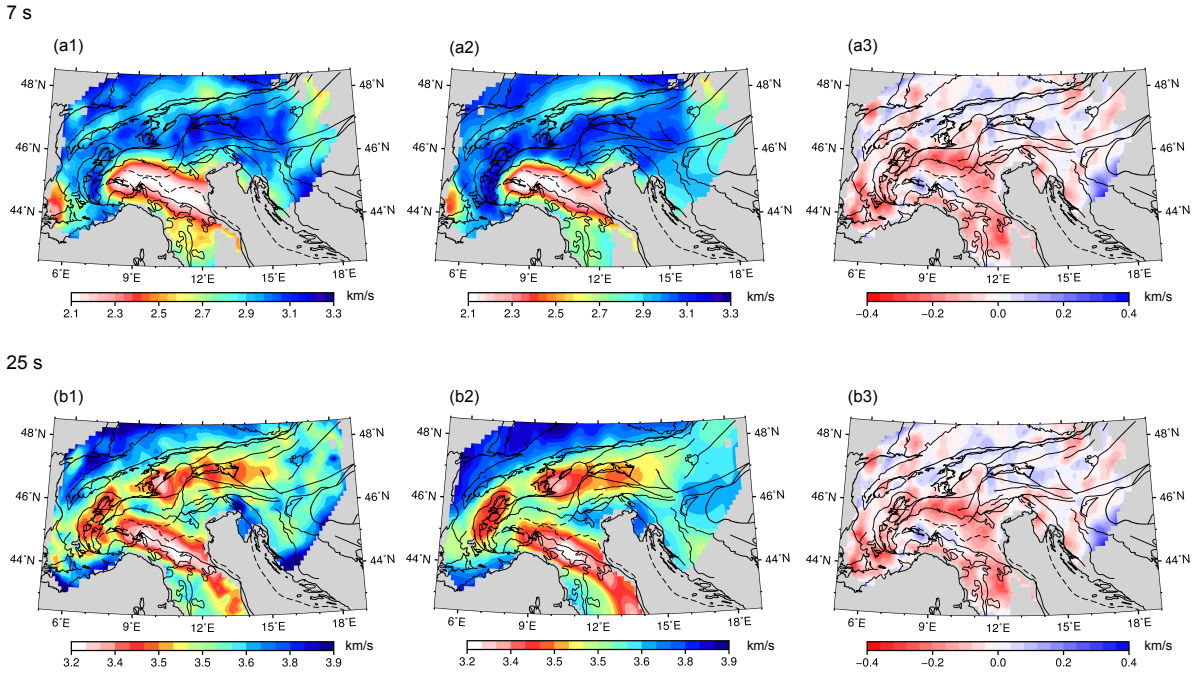

FIGURE 4.7 – Comparison of isotropic phase velocity maps obtained from Eikonal tomography (a1, b1) and our phase velocity tomography of the European crust and uppermost mantle in section 4.3 (a2, b2) at 7 and 25 s. (a3) and (b3) show the absolute differences of phase velocity at the two periods.

traditional phase velocity tomography are more smooth.

4.4.3 Phase velocity azimuthal anisotropy maps

The directions of phase velocity estimates are naturally obtained in Eikonal tomography, so it is convenient to derive maps of phase velocity azimuthal anisotropy. However, it is necessary to first stack our results of neighboring cells for the following reasons : (1) the directional phase velocity estimates have non-negligible uncertainties (Fig. 4.6) ; (2) the directional phase velocity estimates do not have a sufficient azimuthal coverage in each cell. To deal with that, we stack results of all neighboring cells within a distance of 75 km. As a consequence, the resulting phase velocity azimuthal anisotropy maps are more stable and interpretable, but the resolutions of resulting maps are reduced.

To ensure the quality of azimuthal anisotropy analysis, we discard cells with less than 1,000 directional phase velocity estimates. In each cell, the directional phase velocity estimates are averaged over bins of 10°. A binned phase velocity estimation is valid only if there are more than 10 phase velocity estimates in that 10° azimuthal bin. We further

discard cells with azimuthal coverage <270°.

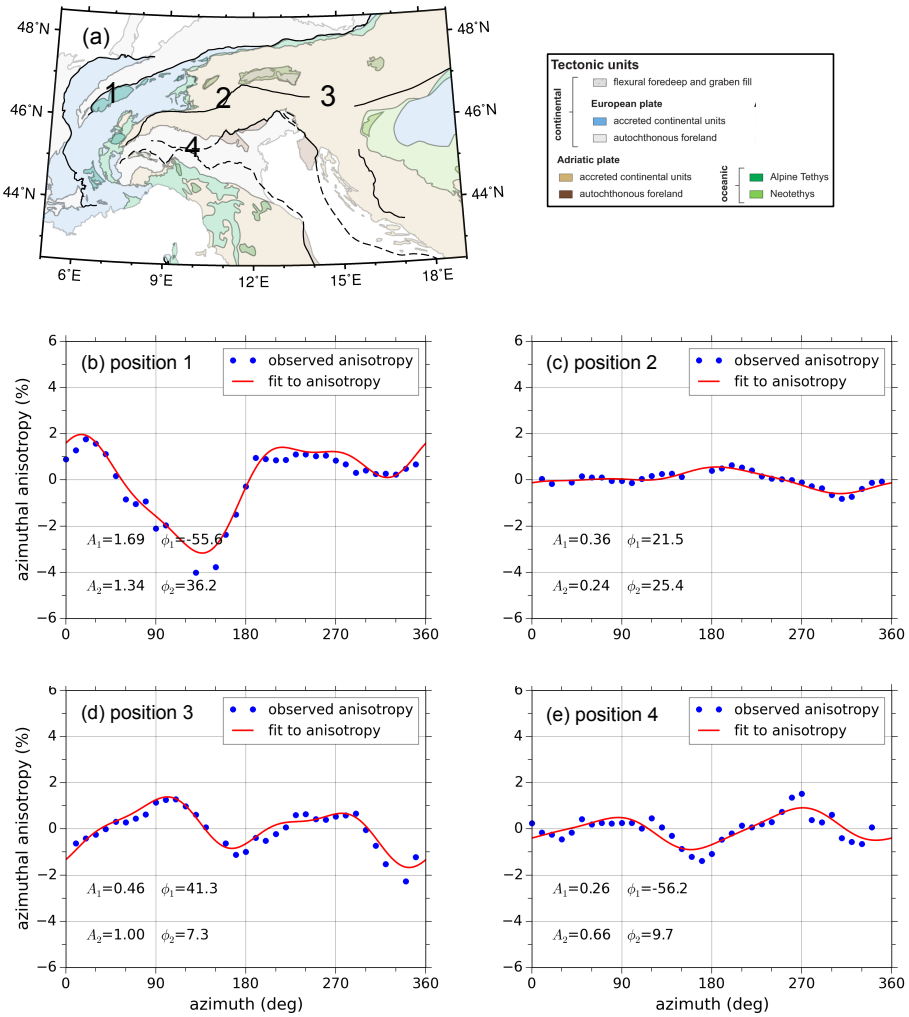

FIGURE 4.8 – Phase velocity azimuthal anisotropy analysis at 18 s. (a) Location map of the four cells and the generalized tectonic map of the Alps (Handy et al., 2010), provided by E. Käestle (http ://www.spp-mountainbuilding.de) ; (b-e) Blue dots display the observed Rayleigh waves phase velocity azimuthal anisotropy, obtained by averaging the directional phase velocity estimates over bins of 10°. Red lines display the fitting curves to the observed phase velocity azimuthal anisotropy using equation 4.6. A_1 and A_2 are the amplitudes of the 2φ and 4φ components of the fitting curves, while ϕ_2 and ϕ_4 are the fast-velocity directions.

According to Smith and Dahlen (1973), in a slightly anisotropic medium, the azimuthal anisotropic phase velocity of Rayleigh waves $c(w, \varphi)$ has the form :

$$c(w,\varphi) = c(w,\varphi)_0 + A_2 cos[2*(\varphi-\phi_2)] + A_4 cos[4*(\varphi-\phi_4)], \tag{4.5}$$

where w is the angular frequency, φ is the azimuth of phase velocity measurement, $c(w,\varphi)_0$ refers to the average phase velocity (isotropic phase velocity), A_2 and A_4 are the amplitudes of the 2φ and 4φ components of the azimuthal anisotropy, while ϕ_2 and ϕ_4 denote the fast-velocity (fast axes) directions for the two components of the azimuthal anisotropy. However, we also find obvious 1φ components in our observations, so we decide to fit the observed azimuthal anisotropy using the following equation :

$$c(w,\varphi) = c(w,\varphi)_0 + A_1 cos[1*(\varphi-\phi_1)] + A_2 cos[2*(\varphi-\phi_2)] + A_4 cos[4*(\varphi-\phi_4)]. \tag{4.6}$$

In Fig. 4.8, we show four examples of the fit at 18 s. We observe non-negligible 1ϕ components of the azimuthal anisotropy. Chen and Tromp (2007) pointed out that there is no physical meaning for the 1ϕ component of the azimuthal anisotropy for surface waves. The 1ϕ component means high velocity in one direction and low velocity in the opposite direction, which is contrary to the reciprocity theorem. Lin and Ritzwoller (2011a) consider the 1ϕ components as isotropic bias in the azimuthal anisotropy measurements, due to neglecting finite frequency effects in Eikonal tomography. We do not discuss the 4ϕ components due to their relatively small amplitudes compared to the 1ϕ and 2ϕ components.

In Fig. 4.9, we display the amplitudes and fast-velocity directions of the 2ϕ components of azimuthal anisotropy at 7, 12, 18 and 25 s. We discard cells with error larger than 0.5% of its average phase velocity (isotropic phase velocity), while the error in each cell is evaluated as the root-mean-square of misfits to the theoretical expression 4.6. Period-dependent azimuthal anisotropy reflects anisotropy property at different depths of the crust. The results at 7 s are mostly related to the anisotropy in the upper crust, those at 12 and 18 s are mostly related to the middle crust, and those at 25 s mainly probe anisotropy in the lower crust. Note that due to strong changes in crustal thickness in the Alpine region, these correspondences are only approximate and valid for an average 35 km crustal thickness.

In general, the azimuthal anisotropy patterns are consistent at the four periods. In the Western Alps, the fast axes directions basically follow the strike of the Alpine orogenic belt, in particular at 12 and 18 s. In the Central Alps, we observe relatively weak azimuthal anisotropy. The fast-velocity directions mostly have North-South orientations in the Eastern Alps, which means they are perpendicular to the strike of the belt, as well as in the Po plain. The average azimuthal anisotropy amplitudes are 0.76%, 0.67%, 0.65% and 0.49% at the four periods.

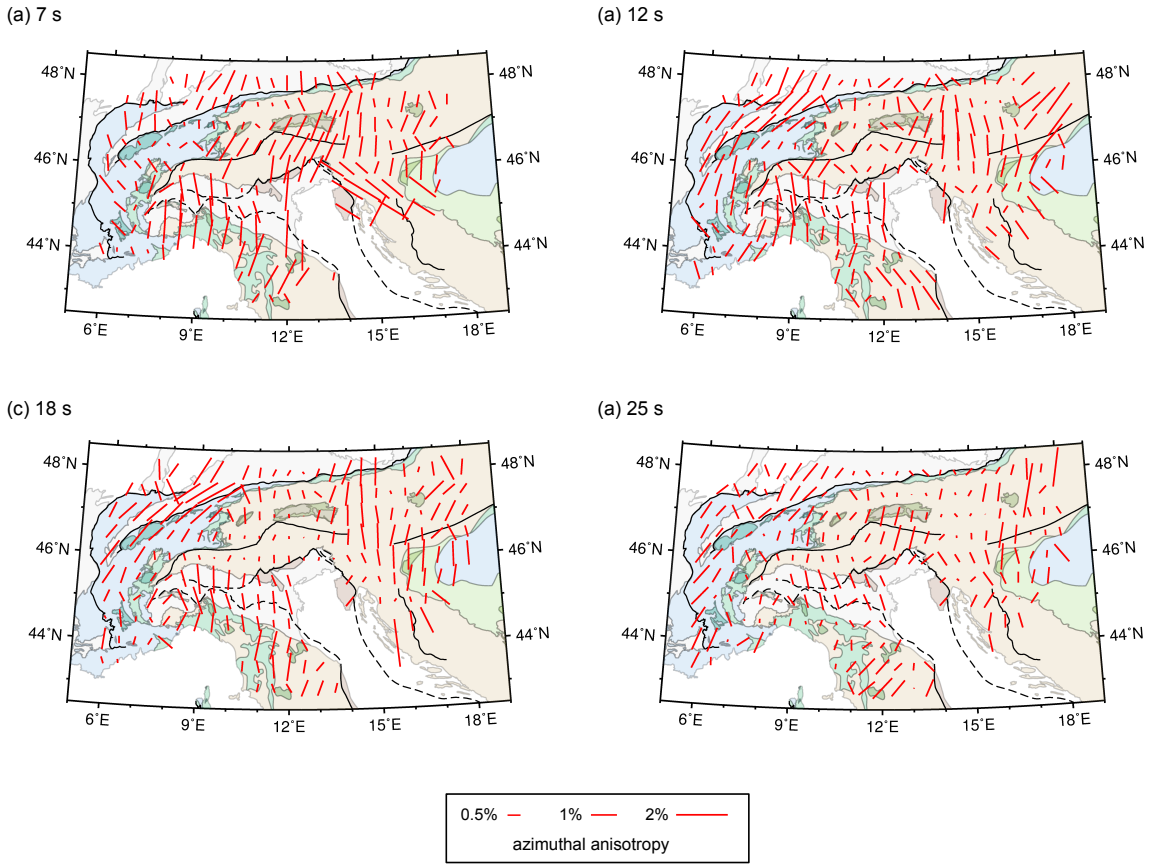

FIGURE 4.9 – 2ϕ components of azimuthal anisotropy for Rayleigh wave phase velocity at 7, 12 ,18 and 25 s. We display the amplitudes and fast-velocity directions of phase velocity azimuthal anisotropy over the generalized tectonic map of the Alps.

4.5 Discussions and perspectives

In the section, we focus on the phase velocity azimuthal anisotropy results. Seismic azimuthal anisotropy is an important indicator of tectonic structure and stress field of the Earth's crust and mantle (Silver, 1996; Savage, 1999). Seismic azimuthal anisotropy is often investigated using shear wave splitting (SWS) analysis. The basic idea is that S waves traversing an anisotropic medium propagate with different velocities for different polarizations. Shear wave splitting analysis using SKS, PKS, or SKKS phases lead to the integral of the anisotropy along the whole ray path from the distant earthquake source. These measurements are usually explained by the anisotropy in the upper mantle as a result of mantle flow induced lattice preferred orientation (LPO) of anisotropic crystals, primarily olivine. The fast-velocity orientation may be interpreted as the mantle flow

direction.

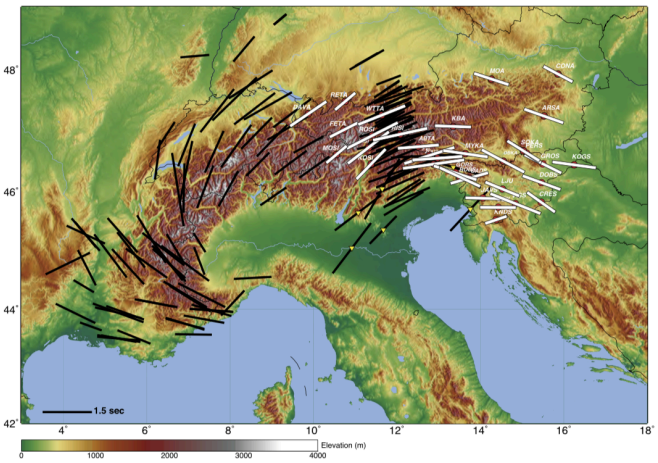

FIGURE 4.10 – Map of SKS splitting measurements in the Alpine region, from Qorbani et al. (2015). White and black lines show measured average fast orientation and splitting delay at each station from studies of Kummerow and Kind (2006), Barruol et al. (2011), Salimbeni et al. (2013) and Bokelmann et al. (2013).

In the Alpine region, many studies have been carried out to analyze the core-phase anisotropy in the mantle using the shear wave splitting analysis (eg. Barruol et al. (2004, 2011); Qorbani et al. (2015); Salimbeni et al. (2018)). The resulting anisotropy patterns are mainly characterized by a continuous trend of fast-velocity directions parallel to the mountain belt (Fig. 4.10). The observed anisotropy is explained by a major counterclockwise asthenospheric mantle flow around the Eurasian slab plunging beneath the inner parts of the Alps (Barruol et al., 2004, 2011).

The resulting crustal anisotropy shows different characteristics to the core-phase anisotropy in the upper mantle. In the Western Alps, our results are rather consistent with fast-velocity directions measured for the upper mantle. In the Central Alps, we observed relatively weak crustal anisotropy. In the Eastern Alps, the crustal anisotropy shows North-South fast-velocity directions, which are perpendicular to the orogenic belt and also to the upper mantle anisotropy orientations.

Studies about seismic azimuthal anisotropy in the crust are less numerous, even though it is also an ubiquitous property as in the mantle. In the upper crust, it is believed that anisotropy is mostly produced by shape-preferred orientation (SPO) of inclusions or cracks, and its fast orientation is parallel to the maximum compression direction (Crampin, 1994). In the mid/lower crust, anisotropy is often related to lattice preferred orientation (LPO) of anisotropic crystals, primarily amphibole and biotite (Tatham et al., 2008).

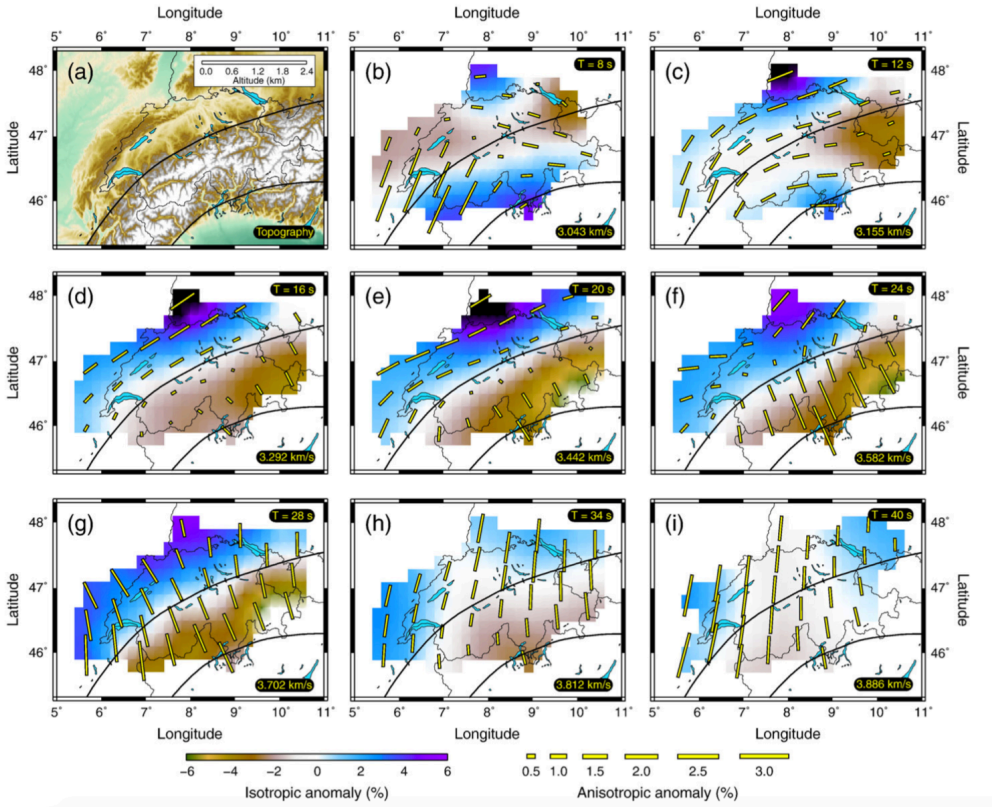

FIGURE 4.11 – 2ϕ components of azimuthal anisotropy for Rayleigh wave phase velocity in the Swiss portion of the Alpine region, from Fry et al. (2010). The first figure shows tomography with 2 black curves representing the Alpine front to the north and Adriatic front to the south. The remaining figures show amplitudes and fast axes directions of the 2ϕ components of azimuthal anisotropy plotted over isotropic phase velocity maps at different periods.

In the Alpine region, the single published paper on crustal azimuthal anisotropy was conducted by Fry et al. (2010), who analyzed the anisotropy in the Swiss portion of the Alpine region using cross-correlations of ambient seismic noise computed from 36 broadband stations. The studied region is parameterized by a grid of triangular with spacing ∼50 km. Period-dependent Rayleigh waves phase velocities measured from the cross-correlations are inverted for 5 parameters, including the four anisotropic coefficients (A_2,A_4,2ϕ,4ϕ) and the isotropic component $c(w,\varphi)_0$ using a linearized inversion algorithm (see expression 4.5 for anisotropic phase velocity). As shown in Fig. 4.11, the results reveal a two-layer azimuthal anisotropy beneath the studied region : a orogen-parallel anisotropy at shorter periods (<20 s) and a strong orogen-perpendicular anisotropy at longer periods. The orogen-parallel anisotropy in the period band 12-16 s is explained by LPO of crustal minerals, while the orogen-perpendicular anisotropy at 28

s and higher periods is explained by the LPO of olivine due to European lithospheric mantle flow.

Our results in the Swiss portion of the Alpine region mainly differ from those of Fry et al. (2010) in the following senses : (1) our azimuthal anisotropy patterns are basically characterized by consistent fast-velocity directions at the four periods, rather than a two-layer anisotropy with different orientations at short and long periods ; (2) the azimuthal anisotropy derived from our study has smaller amplitudes. Nonetheless, the results of Fry et al. (2010) might be more questionable than ours, because : (1) they fit the anisotropy observations using the theoretical expression 4.5 with only 2ϕ and 4ϕ components, while the 1ϕ components are not properly taken into account. As a consequence, the non-physical 1ϕ components might have influenced the inversion results ; (2) the amount of data used in their study is much less than in ours.

We notice that some further works are necessary to complete this study. For instance, we need to perform explicit resolution tests for both the isotropic and azimuthal anisotropic phase velocity maps. The origin of the observed crustal azimuthal anisotropy and of its W-E changes along the belt should be addressed as well.

4.6 Conclusions

In this chapter, we presented two ambient noise phase velocity tomographic studies. Using the cross-correlation dataset compiled in the ambient noise group velocity tomography in chapter 3, we measured Rayleigh waves phase velocities from the spectral domain cross-correlations in the period range 5-150 s.

We first built a 3-D shear wave velocity model for the European crust and uppermost mantle by inverting phase velocity measurements using the same method as in the ambient noise group velocity tomography. The resulting shear wave velocity model underlines similar features to that derived from the group velocity tomography. However, we observed non-negligible differences of absolute velocity values between the two models. In particular, we observed a systematic shift of velocity values at depth.

We also derived isotropic and azimuthal anisotropic phase velocity maps of the Alpine region in the period range 7-25 s using Eikonal tomography. We validated the resulting isotropic phase velocity maps by comparing with those derived from traditional phase velocity tomography. The resulting phase velocity azimuthal anisotropy mainly reveals anisotropy properties of the Alpine crust. The azimuthal anisotropy patterns are consistent in the period range 7-25 s, which is different from the two-layer anisotropy interpretation of Fry et al. (2010). The azimuthal anisotropy pattern shows lateral variations along the Alps, with orogen-parallel fast-velocity directions in the Western Alps, weak anisotropy in the Central Alps, and North-South fast-velocity directions in the Eastern Alps. This observation differs from the well-reorganized continuous orogen-parallel anisotropy in the Alpine upper mantle. We emphasize that our study is the first ambient

noise Eikonal tomography performed in the Alpine region, and the derived phase velocity azimuthal anisotropy maps are the first crustal azimuthal anisotropy results at the scale of the whole Alpine region.

Chapitre 5

Ambient noise wave-equation tomography

Sommaire

s

5.1 Ambient noise wave-equation tomography of the Alpine crust and uppermost mantle

5.1.1 Introduction

Following the pioneering application of Shapiro et al. (2005), surface waves reconstructed from cross-correlations of ambient seismic noise have been widely used to image the crust and upper mantle, giving rise to a class of methods referred to as 'ambient noise tomography'. Traditional ambient noise tomography exploits the dispersive characteristic of surface waves using a two-step inversion approach. In the first step, period-dependent group or phase velocity measurements are inverted to estimate 2-D velocity maps based on ray-theory assumption, which is simplified to the great-circle assumption of ray

path in most cases. In the second step, local dispersion curves extracted from 2-D velocity maps at grid points are inverted to obtain 1-D shear-wave velocity models, which together construct a final pseudo 3-D model.

Traditional ambient noise tomography has been used to image the Alpine region in different studies. For instance, Stehly et al. (2009) constructed a shear-wave velocity model and Moho map for the greater Alpine region using cross-correlation computed from 150 stations in the period band 5-80 s. The most up-to-date study is the one by Lu et al. (2018), who made use of a large cross-correlation dataset across Europe. Continuous vertical-component seismic noise recorded by 1293 broadband stations (from July 2012 to June 2016) are preprocessed using a short-window scheme proposed by Boué et al. (2014b), and the resulting cross-correlations show clear emergence of Rayleigh waves in the period band of 5-150 s. Period-dependent Rayleigh wave group velocity measurements are used to estimate 2-D velocity maps. Then, a Bayesian depth inversion is used to construct the 3-D model LSP_Eucrust1.0 for the European crust and uppermost mantle, including an isotropic shear-wave velocity model and a probabilistic model of interfaces.

In spite of extensive applications of traditional ambient noise tomography, we notice two basic limitations of the two-step inversion approach : (1) as it is not a direct 3-D inversion, the final pseudo 3-D velocity model is not constrained as a whole ; (2) the use of ray theory essentially states that the surface wave traveltime is only sensitive to the structure over the zero-width source-receiver path. It only holds under high-frequency assumption where the scale length of medium heterogeneities is much larger than the seismic wavelength under consideration (e.g. Snieder (1986); Yomogida and Aki (1987); Spetzler et al. (2002); Zhou et al. (2004)). In view of the strong heterogeneity in the Alpine region, these two basic limitations may lead to considerable error in the resulting model, which should be properly accounted for.

However, methodological efforts to improve ambient noise tomography have been mainly dedicated towards improving detailed technical aspects in the same two-step workframe, such as traveltime measurement and correction : e.g. Ekström et al. (2009); Yao and van der Hilst (2009), 2-D Eikonal and Helmholtz tomography : e.g. Lin et al. (2009); Lin and Ritzwoller (2011b), 2-D ray-tracing tomography : e.g. Saygin and Kennett (2012); Nicolson et al. (2012), 2-D Bayesian tomography : e.g. Bodin et al. (2012a); Young et al. (2013) ; 1-D non-linear depth inversion : e.g. Bodin et al. (2012b); Lu et al. (2018).

Following rapid advances in computational facilities and numerical methods, tomography methods based on solving the wave equation became feasible in recent years. These methods consist in minimization of a misfit function defined by traveltime or waveform differences between the observed and synthetic waveforms. The synthetic waveforms are computed from an initial model using full 3-D wavefield modeling techniques, such as the finite-difference method (FD, Graves (1996); Operto et al. (2007)) and spectral-element method (SEM, Komatitsch and Vilotte (1998); Komatitsch and Tromp (1999)). Sensitivity kernels or gradients of the misfit function with respect to physical attributes are usually calculated by the adjoint-state approach, given by the interaction between the forward and adjoint wavefields (Tromp et al., 2004; Liu and Tromp, 2006; Plessix, 2006).

The initial model is iteratively improved using optimization methods, like the conjugate-gradient method (Mora, 1987) or quasi-Newton method (Nocedal, 1980). Depending on the choice of misfit function, these methods roughly fall into two categories : wave-equation tomography (WET) when the misfit function is defined by traveltime difference (Luo and Schuster, 1991), and full waveform inversion (FWI) when the misfit function involves waveform difference (Virieux and Operto, 2009). Here, by 'adjoint tomography' we refer to FWI applied to large scale (regional to global) using the adjoint-state approach for the computation of sensitivity kernels (Liu and Gu, 2012).

Applications of wave-equation based tomographic methods are primarily conducted using earthquake data. These applications take advantages of accurate 3-D wavefield modeling, providing improved images of the Earth beyond those obtained by classical tomographic techniques (e.g. applications at regional and continental scales : Tape et al. (2009); Fichtner et al. (2009); Zhu et al. (2012); Yuan et al. (2014); Fichtner and Villaseñor (2015)).

This naturally leads to inverting ambient noise cross-correlation data using WET, referred to as 'ambient noise wave-equation tomography'. For instance, Chen et al. (2014) applied ambient noise wave-equation tomography to refine the crustal model in southeastern Tibet using ambient noise recorded at 25 stations in the period band 10-40 s. The new method addresses the limitations of traditional ambient noise tomography as it fully accounts for 3-D and finite frequency effects. Unlike the earthquake-based WET, observed waveforms in the ambient noise wave-equation tomography are the Green's function reconstructed from cross-correlations, primarily for the vertical component of Rayleigh waves. Synthetic waveforms are generated by applying a single force on the surface or near-surface with a filtered Dirac as source function. The misfit function can be defined by cross-correlation type traveltime differences as in classical WET (Luo and Schuster, 1991), or frequency-dependent traveltime differences measured from multitaper method (Tape et al., 2009). To avoid any confusion of notation, we combine the two names 'full-wave ambient noise tomography' (Gao and Shen, 2014; Shen and Ritzwoller, 2014) and 'ambient noise adjoint tomography' (Chen et al., 2014; Liu et al., 2017) in 'ambient noise wave-equation tomography', since these methods define the misfit function using traveltime differences as in WET.

Meanwhile, full waveform inversion of ambient noise cross-correlation is still impossible. While the phase (traveltime) of the Green's function can be accurately measured from cross-correlation, the amplitude is poorly estimated due to its high sensitivity to the anisotropic distribution of noise sources, the medium heterogeneity and the preprocessing procedure (Sager et al. (2018), see section 2.3 for numerical tests). Fichtner (2014) stated that the full waveform inversion of ambient noise cross-correlations is not achievable unless the noise source distribution and preprocessing procedure are properly accounted in the inversion. Tromp et al. (2010) attempted to drop the concept of Green function retrieval and to establish cross-correlations as self-consistent observables. The basic idea is to compute the synthetic cross-correlation between a station pair using simulated noise fields in the forward simulation, rather than treating the station pair as a source-receiver

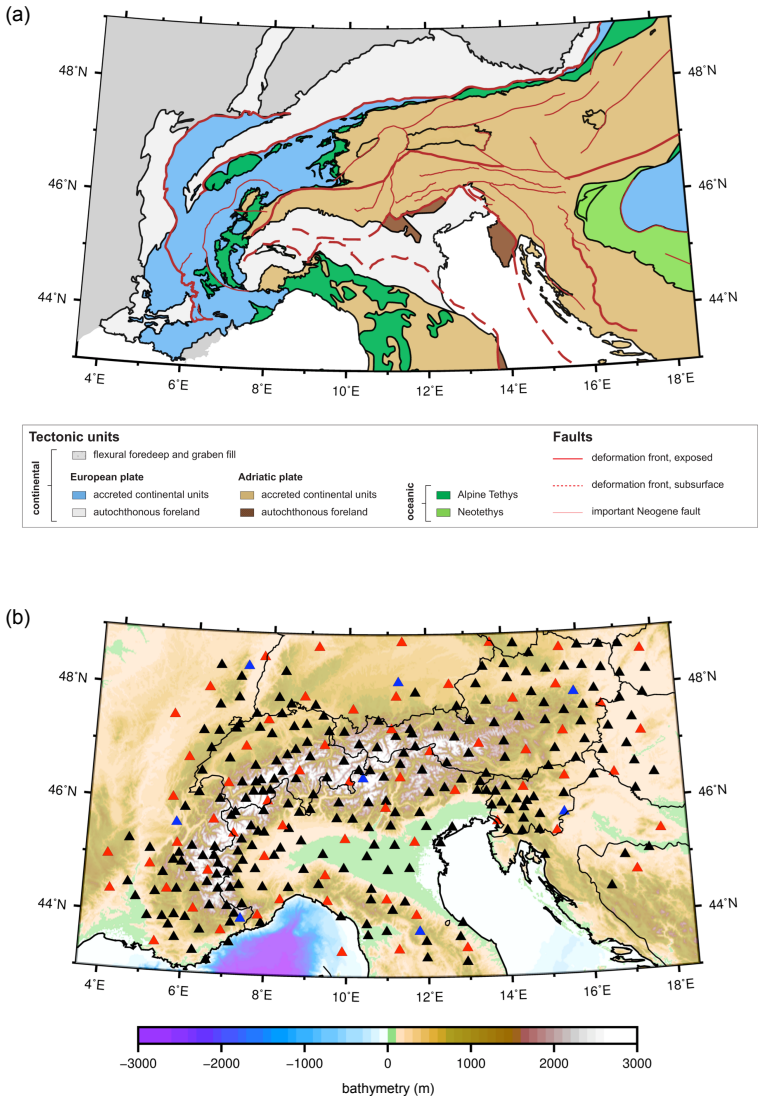

FIGURE 5.1 – Tectonic map and seismic station map of the studied region. (a) Generalized tectonic map of the Alps (Handy et al., 2010), provided by E. Käestle (http ://www.spp-mountainbuilding.de) ; (b) Location of seismic stations (triangles) plotted on topographic map. Red triangles : virtual source stations for inversion ; blue triangles : virtual source stations for validation.

pair. With synthetic data, Sager et al. (2018) showed improved accuracy and resolution of images with respect to those obtained from WET. Nonetheless, the method requires a good estimate of noise source fields, which are temporally and spatially non-stationary in reality. Thus, full waveform inversion of ambient noise cross-correlation has not been

applied in practice so far.

In this study, we apply ambient noise wave-equation tomography to the Alpine region. The primary goal is to refine the shear-wave velocity model *LSP_Eucrust*1.0 for the Alpine crust and uppermost mantle. To that end, we select ∼10,000 high-quality cross-correlations computed from 304 broadband stations (Fig. 5.1b). Following a similar approach as Chen et al. (2014) and Liu et al. (2017), we iteratively improve the initial model *LSP_Eucrust*1.0 by minimizing frequency-dependent multitaper traveltime differences between the observed and synthetic Rayleigh waves in the period range 10-55 s. The inversion is performed using the SEM46 code package developed within the SEISCOPE consortium (Trinh et al. (2019), https ://seiscope2.osug.fr). The SEM46 code package employs spectral-element method for forward simulation, adjoint-state method for misfit kernel computation and the SEISCOPE optimization tool box for model update (Métivier and Brossier, 2016).

The chapter is organized as follows. In section 5.1.2, we present the data and initial model. In section 5.1.3, we introduce our tomographic method. We show the inversion procedure and misfit evolution (total misfit, misfit histograms, misfit spatial distributions) in section 5.1.4. We discuss the results in section 5.1.5, including the resulting shear-wave velocity model, some reference cross-sections and the Moho map.

5.1.2 Data and initial model

This study shares the cross-correlation dataset of Lu et al. (2018). We choose cross-correlations related to 304 stations in the Alpine region (Fig. 5.1). All 304 stations serve as virtual receivers, from which we select 64 as virtual sources to reduce high computational cost of 3-D numerical simulation, providing us with ∼18,000 cross-correlations. We keep only reliable cross-correlations by applying the following criteria in the period band 10-55 s : (1) we choose cross-correlations with signal-to-noise ratio (SNR) greater than 5, while the SNR is defined as the ratio between the envelope maximum of surface waves and the standard deviation of late coda waves ; (2) we require the inter-station distance to be larger than one wavelength for the maximum period considered. Accordingly, we kept ∼10,000 high-quality cross-correlations as inversion dataset.

Besides, we build a validation dataset, which is independent from the inversion dataset. It consists in ∼1,400 high-quality cross-correlations related to 8 stations as virtual sources and selected using the same criteria as for the inversion dataset. The validation dataset is not involved in the inversion procedure, but it is used to avoid the over-interpretation of inversion dataset. The basic concept is that an improved model should provide better fit to both inversion and validation datasets. If not, the inversion procedure starts mapping errors of the inversion dataset into the model, and the iteration should stop.

We choose model LSP_Eucrust1.0 as initial model (Fig. 5.2). On one hand, LSP_Eucrust1.0 is so far the best resolved shear-wave velocity model of the European crust and uppermost

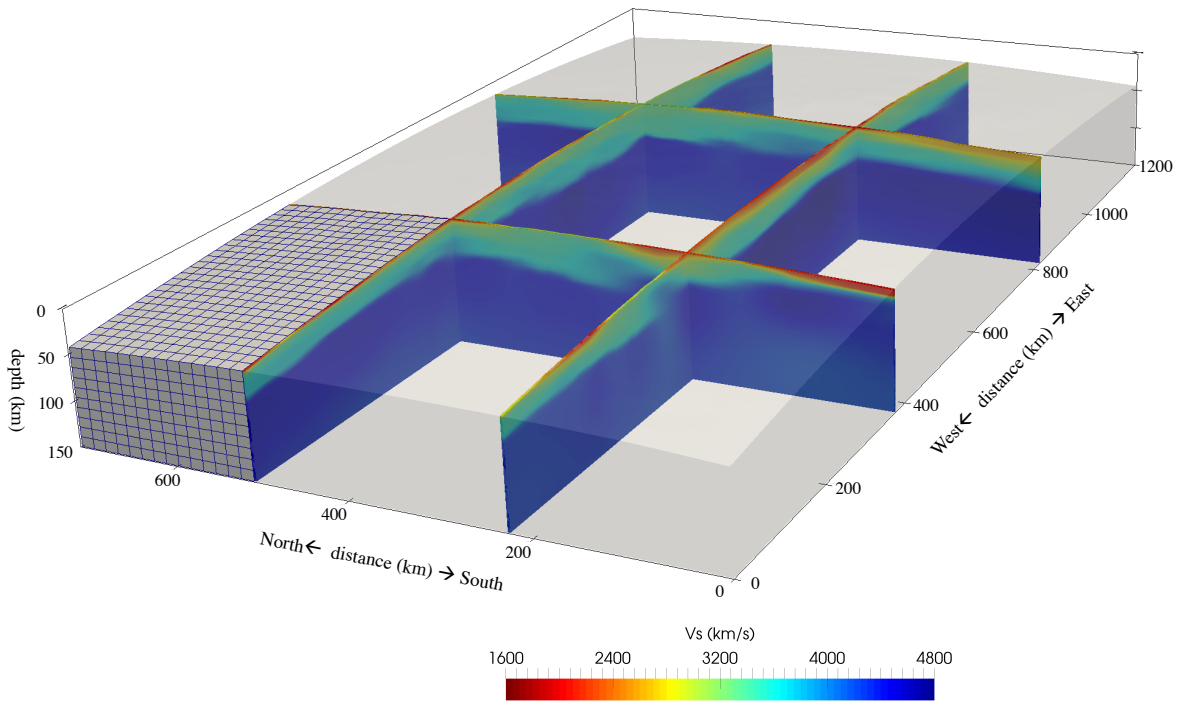

FIGURE 5.2 – Mesh and shear-wave velocity of the initial model. Gray volume indicates the scope of the the initial model. It is centered at 11°E and 46°N with lateral dimensions 1200 km in the East-West direction and 720 km in the North-South direction. We show the shear-wave velocity values of initial model in four representative cross-sections. We show the mesh of the North-West portion of initial model. The topography and curvature of the Earth are accounted by vertically deforming the mesh grid.

mantle. It was validated by comparison with different geophysical studies, in particular controlled source seismic experiments along the Alpine arc. On the other hand, an important goal of the study is to test how ambient noise wave-equation tomography improves traditional ambient noise tomography results.

5.1.3 Method

We present the ambient noise wave-equation tomography method in this section. As discussed in the introduction, the goal is to iteratively minimize frequency-dependent phase traveltime differences between observed and synthetic seismic waveforms. To that end, we follow the workflow shown in Fig. 5.3. The details of the main steps of the workflow are given below.

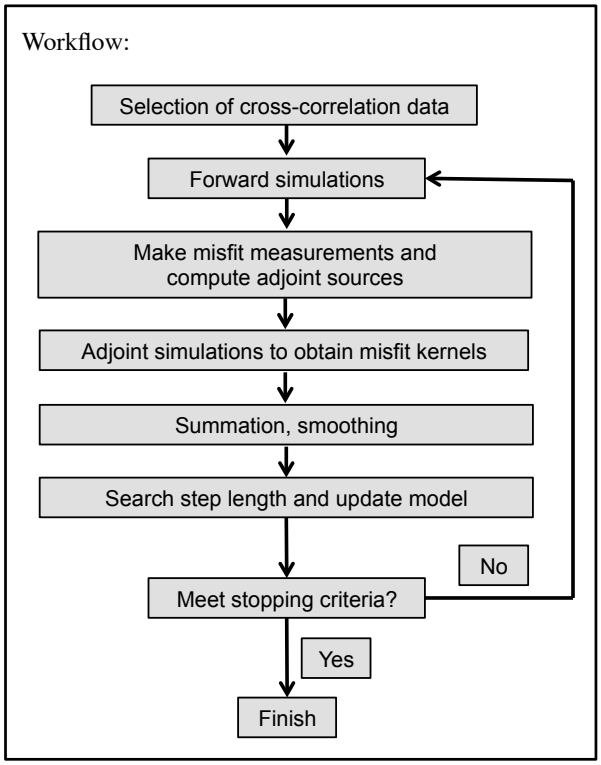

FIGURE 5.3 – General ambient noise wave-equation tomography workflow.

5.1.3.1 Forward simulation

The spectral-element method has proved to be an accurate and efficient method of wavefield simulation in a 3-D heterogeneous medium (Komatitsch and Vilotte, 1998; Komatitsch and Tromp, 1999, 2002a,b). It benefits from the geometrical flexibility of finite-element method (FEM) and the exponential convergence rate of spectral methods. Given these advantages, the spectral-element method is recognized as the most popular forward simulation method in wave-equation based tomographic applications at regional to global scales.

We compute synthetic waveforms using the 3-D elastic wave-equation solver of SEM46 package, which is developed in a classical hexahedra-based spectral-element method frame (Trinh et al., 2017a). Our initial model is discretized using a mesh built in cartesian coordinates (Fig. 5.2). It is centered at 11°E and 46°N with lateral dimensions 1200 km in the East-West direction and 720 km in the North-South direction. We handle the topography and the curvature of the Earth by vertically deforming the mesh. Thus, the verticle dimension ranges approximately from 150 km in the center to 110 km on

the edges due to the vertical compression of mesh. Using Lagrange polynomials of order 4, we choose element size 15 km in horizontal direction, and 10-15 km in vertical direction with respect to the volume condition to ensure accuracy of wavefield simulation (Komatitsch and Tromp, 1999). As a consequence, the average spacing between Gauss-Lobatto-Legendre (GLL) points is around 3.5 km. Since the quality factor (Q) model of the Alpine region is still missing, we ignore the attenuation and parameterize each Gauss-Lobatto-Legendre point of the initial model by isotropic Vs, Vp and ρ. The Vs values of initial model are taken from model LSP_Eucrust1.0, while Vp and ρ are converted from Vs using empirical formulas (Ludwig et al. 1970 ; Brocher 2005).

To simulate the vertical component of Rayleigh waves, we apply a vertical single force at each virtual source position on the free surface, and a Dirac function filtered in the desired period band 10-55 s is used as source function. In this way, the recorded synthetic waveforms u_{syn} at a receiver position for model m is the convolution product between the source function $s(t)$ and the Green's function $G_{syn}(m,t)$ for the source-receiver pair :

$$u_{syn} = \ s(t) \otimes G_{syn}(m,t), \tag{5.1}$$

where $\otimes$ denotes the convolution operator. The time-stepping for the simulation is 0.004 s, meeting the Courant-Friedrichs-Lewy (CFL) stability condition (Komatitsch and Tromp, 1999).

5.1.3.2 Misfit measurements

The Green's function between a station pair can be estimated from the derivative of cross-correlation $C(t)$ of seismic noise recorded at the two stations (Weaver and Lobkis (2001); Lobkis and Weaver (2001); Derode et al. (2003b,a); Snieder (2004); Wapenaar (2004), see mathematical demonstration and numerical illustration in chapter 2) :

$$G_{true}(t) \approx -A\frac{\partial C(t)}{\partial t}. \tag{5.2}$$

where A is the amplitude term related to noise source energy. To compare with synthetic waveforms, we convolve the source function used for simulation with the negative derivative of the cross-correlation :

$$u_{obs} = \ s(t) \otimes -\frac{\partial C(t)}{\partial t} \approx \frac{1}{A} s(t) \otimes G_{true}(t). \tag{5.3}$$

This convolution product serves as observed waveform at each receiver. Both observed and synthetic waveforms are tapered to keep only Rayleigh waves. For this purpose, we

use a time window with $min[D/5, T_{umax} - 55]$ and $max[D/2, T_{umax} + 55]$ as lower and upper limits, where D is the inter-station distance expressed in km and T_{umax} refers to the arrival time for the envelope maximum of synthetic waveforms. $D/5$ and $D/2$ correspond to the range of typical phase arrival times of Rayleigh waves in the 10-55 s period band. $T_{umax} - 55$ and $T_{umax} + 55$ refer to 55 s (one maximum period) before and after the envelope maximum of synthetic waveforms, which are complementary criteria allowing to include the entire surface wave package.

To make full use of the dispersive characteristics of surface waves, we define the misfit function using frequency-dependent phase traveltime differences between the observed and synthetic waveforms (Tape et al., 2009). For model m, the total misfit function is expressed as :

$$F(m) = \frac{1}{2} \sum_i \sum_w \Delta T_i(w, m)^2, \tag{5.4}$$

where w is the frequency, and $\Delta T_i(w, m) = T_i^{syn}(w) - T_i^{obs}(w, m)$ denotes the frequency-dependent phase traveltime difference for ith station pair. Since we only use traveltime (phase) information, the amplitude term A in equation 5.2 can be ignored. The traveltime differences between the observed and synthetic waveforms (u_{obs} and u_{syn}) are indeed differences between the true and synthetic Green's function computed from model m ($G_{true}(t)$ and $G_{syn}(t, m)$).

We measure the phase traveltime differences using multitaper method, which is an efficient method in analyzing phase and spectrum for time-and-band limited signals (Thomson, 1982). The method, taking advantages of a series of prolate spheroidal eigentapers (Slepian and Pollak, 1961), provides independent measurements of phase traveltime differences between the observed and synthetic waveforms. The final measurement is determined as the average of the ensemble of independent measurements.

5.1.3.3 Misfit kernels

We compute misfit kernels (also referred to as Fréchet kernels or misfit gradients) using the adjoint-state approach under Born approximation (Tromp et al., 2004; Liu and Tromp, 2006; Plessix, 2006). Since the phase velocity of Rayleigh waves is sensitive to both Vp and Vs, we express the perturbation of total misfit function for model m by the following linear relation :

$$\delta F(m) = \int_V [K_{Vs}(m, x) \delta ln\mathrm{m_{Vs}(x)} + K_{Vp}(m, x) \delta ln\mathrm{m_{Vp}(x)}] d^3x, \tag{5.5}$$

where $K_{Vs}(m, x)$ and $K_{Vp}(m, x)$ denote the misfit kernels with respect to Vp and Vs at position x, $\delta ln\mathrm{m_{Vs}(x)}$ and $\delta ln\mathrm{m_{Vp}(x)}$ are relative perturbations of Vp and Vs.

The misfit kernels for a single station pair are given by the interaction of the forward and adjoint wavefields. Regarding our choice of misfit function, the adjoint source is related to the derivation of synthetic waveforms weighted by the frequency-dependent phase difference measurements (Tape, 2009). In practice, we use the concept of combined adjoint source to save computational cost. Instead of computing kernels for each single station pair, it is possible to only compute kernels for each source station (event) using the combined adjoint source, which is the sum of adjoint sources for all station pairs related to the source station. To reduce the memory requirement, we recompute the forward wavefield from the stored decimated wavefield in the boundaries, synchronously with the computation of the adjoint wavefield (Yang et al., 2016). Thus, we need 3 simulations for computing kernels of each source station.

We sum kernels computed for all source stations, and we smooth the summed kernels using an approximated Laplace filter to remove artificial high-wavenumber gradient artifacts (Trinh et al., 2017a,b). The filter width decreases with increasing iterations, so that we can progressively resolve smaller size heterogeneities. The filter width decreases from 8 km to 2 km in the horizontal direction and from 4 km to 1 km in the vertical direction.

5.1.3.4 Iterative inversion procedure

The inversion corresponds to a local optimization problem based on the second-order Taylor expansion of misfit function :

$$F(m+\delta m) \approx F(m) + g(m)^T \delta m + \frac{1}{2}\delta m^T H(m) \delta m, \tag{5.6}$$

where δm is the model update, $g(m)$ is the gradient of misfit function, and $H(m)$ is the Hessian as a second-order derivative of misfit function with respect to the model parameters. The misfit $F(m+\delta m)$ can be reduced by updating the model via

$$\delta m = -\alpha H(m)^{-1} g(m), \tag{5.7}$$

where α and $-H(m)^{-1}g(m)$ are the optimal step length and direction of model update. However, this optimum update is usually not available in practice, because accessing the full Hessian matrix is unfeasible. In our case, we address the problem using the limited memory quasi Newton method (l-BFGS-B) because of its simplicity and efficiency (Nocedal, 1980). The method approximates $-H(m)^{-1}g(m)$ as a whole using gradient values of a few previous iterations. It shows faster convergence than the nonlinear conjugate gradient and steepest-descent algorithms in the numerical tests conducted by Métivier and Brossier (2016). A line search strategy is employed to find appropriate step length of model update (Métivier and Brossier, 2016).

5.1.3.5 Implementation

Our implementation consistes in 64 forward simulations for computing synthetic waveforms, and 64 paris of forward and backward simulations for computing misfit gradient in each iteration. The model is divided into 4 subdomains, and 64 simulations were performed simultaneously in parallel using 256 cores. In each iteration, the computational cost is approximately 1,000 core hours on Froggy architecture (Intel Sandy Bridge EP E5-2670, 8c/2.6 GHz/20M/8 GT/s, https ://ciment.ujf-grenoble.fr/wiki).

5.1.4 Misfit reduction

5.1.4.1 Total Misfit

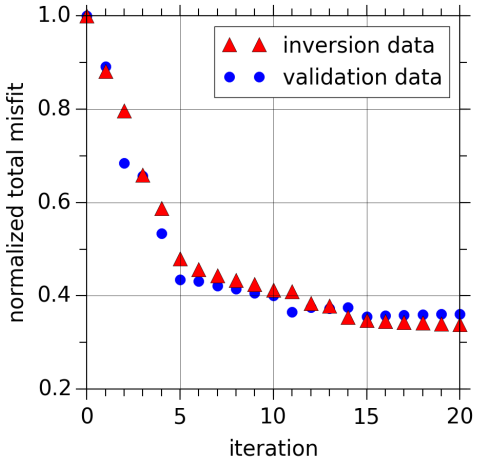

FIGURE 5.4 – Total misfit reduction over iterations. Red triangles and blue dots represent the evolution of normalized total misfit for the inversion and validation datasets.

Fig. 5.4 shows the reduction of total misfit over iterations (0-20) for the inversion and validation datasets. The total misfit of inversion dataset shows a quick drop in the first five iterations and a gradual decrease in the following iterations. In general, the total misfit of validation dataset has similar evolution as that of the inversion dataset, except for a slight increase after 15 iterations. As we mentioned in section 5.1.2, an improved model should provide better fits to both inversion and validation datasets. The increase of validation dataset misfit after 15 iterations indicates that the inversion procedure begins to over-interpret the data. Thus, we choose the model of 15th iteration as the final model. For convenience, we name the updated model according to the iteration number, with m00 the initial model and m15 the final model. The final model (m15)

shows a significant reduction of misfit with respect to the initial model (m00), which amounts to $\sim 65\%$ for both inversion and validation datasets.

5.1.4.2 Histograms of misfit

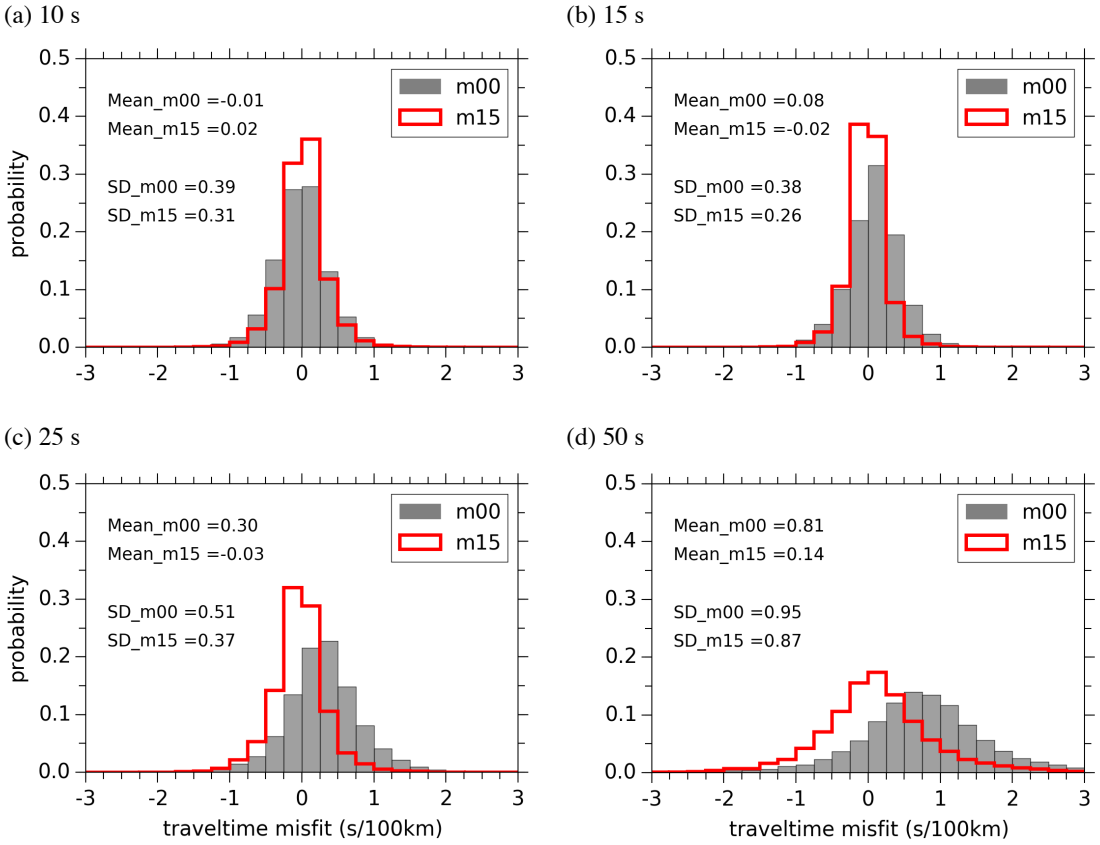

FIGURE 5.5 – Comparison of misfit histograms (inversion dataset) for the initial (m00) and final models (m15) at 10, 15, 25 and 50 s. The misfit refers to the traveltime misfit for waves propagating 100 km. Mean refers to the mean misfit, and SD refers to the standard deviation.

In Fig. 5.5, we compare histograms of traveltime misfit (inversion dataset) for the initial (m00) and final models (m15) at 10, 15, 25 and 50 s. The traveltime misfits vary according to inter-station distance, as for instance, station pairs of large inter-station distance naturally have large misfits. Thus, in this and the following sections, we express misfit using a distance weighted traveltime misfit $\delta T_i(w,m)/D * 100$, which corresponds to the traveltime misfit for waves propagating 100 km.

The misfit of the initial model shows two main characteristics : (1) the standard deviation misfit basically increases with period ; (2) the mean value of misfit is mostly >0 and it also increases with period. The positive shift means that the velocity values in the initial model are lower than those of the true model.

The final model is an improvement of the initial model in terms of both the standard deviation and mean value of misfits. The misfits of final model are centered around zero with more concentrated distribution. For example, at 25 s, the misfits of initial model are mostly in the range 0.30 ± 1.02 s/100km (considering two standard deviations), while those of the final model are mostly in the range -0.03 ± 0.74 s/100km. Assuming an average Vs value of 3.8 km/s at this period, we can roughly estimate the Vs misfits to -0.00 ± 0.10 km/s for the final model.

5.1.4.3 Spatial distribution of misfit

Fig. 5.6 compares the spatial distributions of misfit for the initial model (m00) and final model (m15) at representative periods. At each period, we discretize the studied region with a mesh of square cells of size 0.5°. For each cell, we calculate the mean value of misfit for all paths crossing the cell assuming ray paths are great-circles. We only display cells crossed by more than 10 paths.

While most studies display misfits using histograms as in Fig. 5.5, we find that the map of spatial distribution is also useful representation of misfits. Using the misfit map combined with the misfit histogram, we can distinguish the contributions of different origins of misfit. The misfits due to isotropic velocity values are expected to show misfit anomaly patters coinciding with geological structures. The misfits due to azimuthal anisotropy or data errors are presented in the misfit histogram, but they are not obvious in the misfit map since we average all paths from different azimuths in each cell.

The most striking features in the misfit maps of initial model are low misfit anomalies along the Western Alps and high anomalies in the North Apennines and the North Adriatic sea. The correspondence of misfit anomaly patters with geological structures indicates that these misfits are due to the imperfect isotropic velocity values in the initial model. Since we do not consider anisotropy in our inversion, these misfits are indeed the target to minimize.

In the misfit maps of final model, the regional patterns observed for the initial model have disappeared. Large misfits mostly locate along the boundary of studied region, where the data coverage is poor. The other misfits as shown in Fig. 5.5(red) are mainly related to anisotropy or data errors (see section 4.4.3 for analysis of azimuthal anisotropy of the Alpine region). Besides, as we have mentioned above, a positive misfit shift increasing with period is observed for the initial model, which is corrected in the final model.

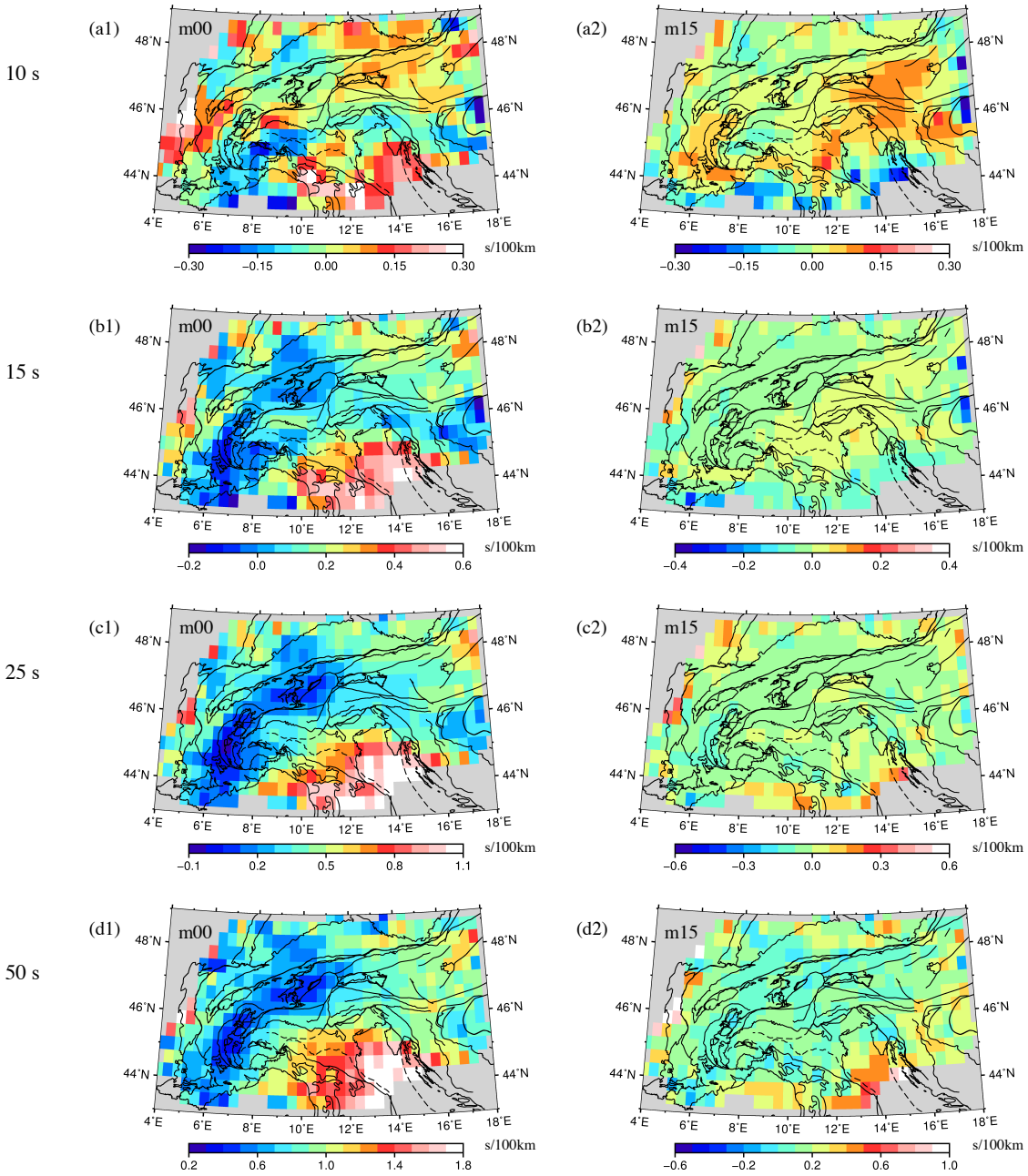

FIGURE 5.6 – Comparison of spatial distributions of misfit for the initial model (m00) and final model (m15) at 10, 15, 25 and 50 s. We only display cells crossed by more than 10 paths. The black lines in each map correspond to the geological and tectonic boundaries in the generalized tectonic map of the Alps shown in Fig. 5.1(a).

5.1.5 Results

In this section, we display the final model (m15) using shear-wave velocity depth slices, depth sections and Moho depth map (shear-wave isovelocity 4.0 km/s). We focus on the comparison of the final model with the initial model.

5.1.5.1 Shear-wave velocity depth slices

In Fig. 5.7, we show the comparison of depth slices at 10, 30 and 50 km in the initial and final models. At 10 km, the strong low velocity anomaly is related to the deep sedimentary basin of the Po plain, and the high velocity anomaly along the alpine belt is due to the crystalline basement in the Alps. At this depth, the final model shows obvious improvements to the initial model. Firstly, the final model displays detailed velocity anomalies, while the initial model depicts general patterns of main velocity anomalies. Some new features emerge in the final model, as for instance, we observe the high velocity anomaly related to the Ivrea body (IB) extending towards North-East until the Central Alps. Secondly, the final model shows much stronger velocity contrasts. For instance, the low velocity anomaly beneath the Po plain is 10% lower in the final model than in the initial model.

At 30 km, the most striking features are low velocity anomalies related to the deep crustal roots of the Alps and the Apennines. At this depth, the final model improves the initial models in several aspects. As in the 10 km depth slices, the final model shows higher resolution and stronger velocity contrasts with respect to the initial model. Besides, we observe an important shift of mean Vs values. Moreover, the final model shows an evident correction of the shape of the Alpine and Apennines crustal roots, which are much narrower than those in the initial model.

At 50 km, the final model shows similar patterns as the initial model, and the most important improvement in the final model is the velocity shift. In general, the final model has higher resolution and much stronger velocity contrasts than the initial model at upper crustal and Moho depths (10 and 30 km). The final model displays new features and corrects existing features in the initial model. At Moho and Mantle depths (30 and 50 km), the final model corrects the velocity shift mentioned in section 5.1.4.2 and Fig. 5.5.

5.1.5.2 Shear-wave velocity depth-sections along reference profiles (Cifalps, ECORS-CROP, Transalp)

We compare depth-sections in the initial and final models along three representative profiles across the Alps (Fig. 5.8). In Fig. 5.9, we show depth-sections along Cifalps, which is a seismic profile traversing the southwestern Alps. Compared to the initial model, we observe a much thicker sedimentary basin (reaching $\sim$15 km) of the Po plain in the final model. Besides, the western boundary of the Ivrea body is less steep in the final model. We also compare our results to those of the receiver function analysis by Zhao

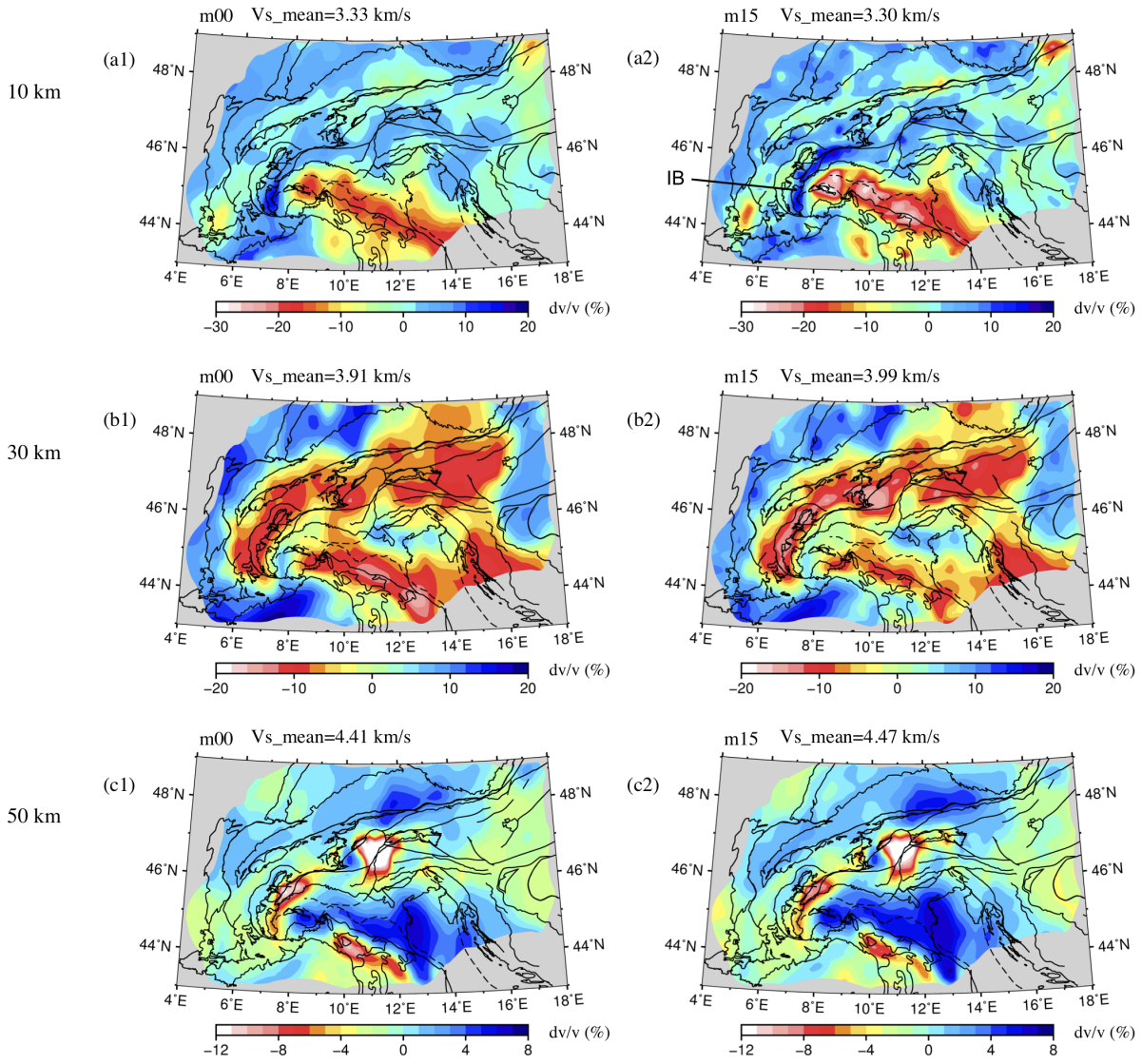

FIGURE 5.7 – Comparison of depth slices at 10, 30 and 50 km in the initial model (m00) and final model (m15). The relative variations of velocity to the average velocity of each slice are displayed to emphasize the changes in the shape and amplitudes of anomalies. As in Fig. 5.6, we discard areas with poor data coverage. The black lines in each map correspond to the geological and tectonic boundaries in the generalized tectonic map of the Alps shown in Fig. 5.1(a). IB : Ivrea body.

et al. (2015). Both the initial and final models, as results of traditional ambient noise and wave-equation tomography, show a ∼5 km shallower European Moho (abscissae < 230 km) than that estimated from the receiver function analysis (black dashed lines).

Fig. 5.10 displays depth sections in the initial and final models along the ECORS-

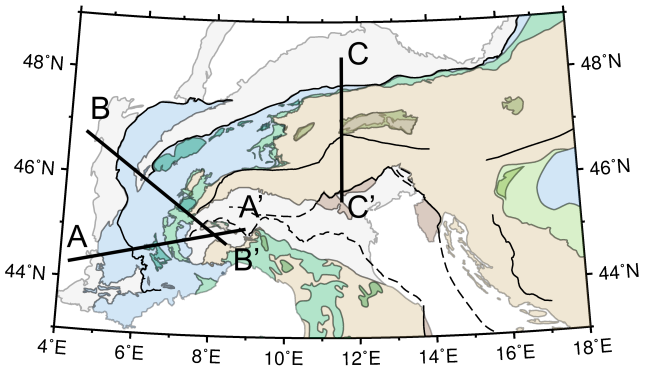

FIGURE 5.8 – Location map of three representative profiles across the Alpine mountain range : Cifalps (AA'), ECORS-CROP (BB') and Transalp (CC').

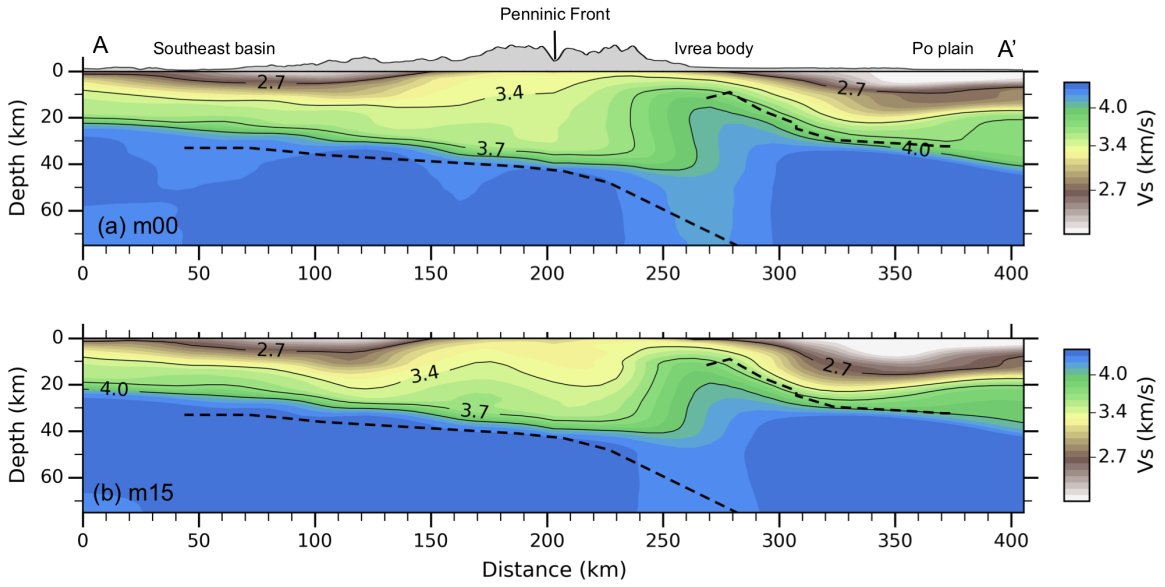

FIGURE 5.9 – Depth-sections along the Cifalps seismic profile in the initial (a) and final models (b). In both (a) and (b), the black dashed lines refer to the European Moho, the top of the Ivrea body and the Adriatic Moho estimated from receiver function analysis by Zhao et al. (2015). The 2.7, 3.4, 3.7 and 4.0 km/s velocity contours roughly depict the bottoms of sedimentary basin, upper crust, middle and lower crust (Moho).

CROP profile (Thouvenot et al., 1990; Sénéchal and Thouvenot, 1991). As in the depth sections along Cifalps, the sedimentary basin of the Po plain is much thicker in the final

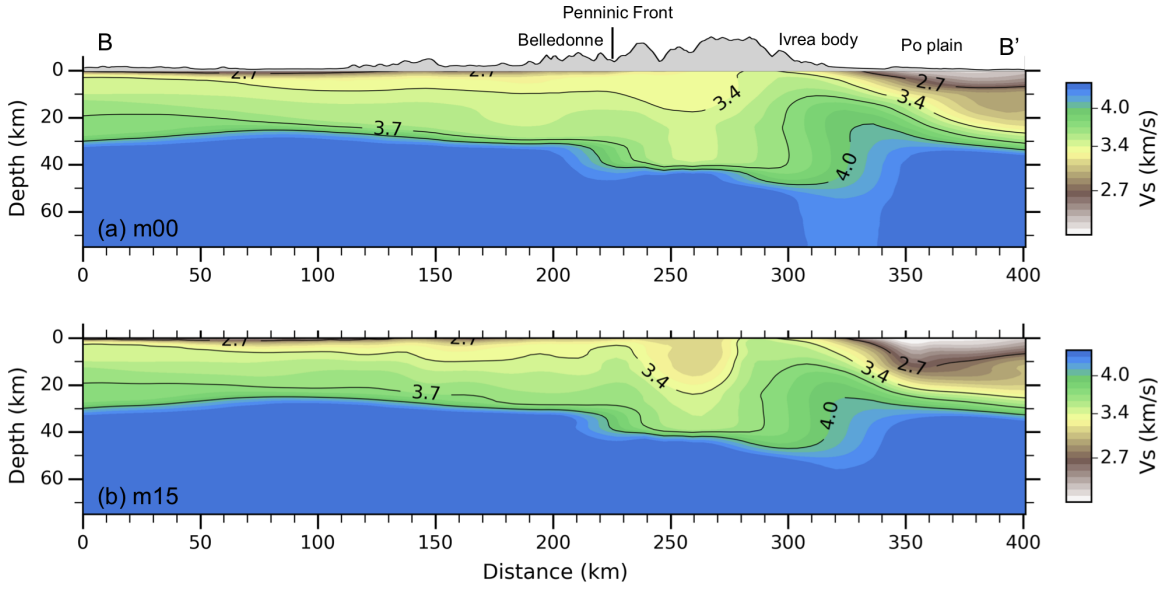

FIGURE 5.10 – Depth-sections along the ECORS-CROP seismic profile in the initial (a) and final models (b). The 2.7, 3.4, 3.7 and 4.0 km/s velocity contours roughly depict the bottoms of sedimentary basin, upper crust, middle and lower crust (Moho).

model than in the initial model. Another striking difference from the initial model is much lower Vs values in the upper crust of the internal zones (230-280 km). The final model confirms the ∼8 km Moho jump beneath the inner boarder of the Belledonne Massif (210-230 km).

In Fig. 5.11, we show depth-sections along the Transalp seismic profile traversing the eastern Alps (Transalp Working Group 2002). Along this profile, we observe considerable differences between the initial and final models. First, a clear uplift of the Adriatic Moho (4.0 km/s isovelocity, 180-230 km) reaching a depth of 25 km emerges in the final model. In the northern boundary of the Moho bump, we even find a vertically reversed velocity contrast. Second, the final model shows much lower velocity beneath the Tauern window. Third, the final model has a thicker lower crust of the European plate than the initial model.

5.1.5.3 Moho map

We display the comparison of Moho depth maps derived from the initial and final models in Fig. 5.12 and Fig. 5.13. We determine the Moho depth using shear-wave isovelocity 4 km/s. The main features in both maps are deep Moho of the Alps, Apennines and Dinarides, and shallow Moho on top of the Ivrea body and in the oceanic region.

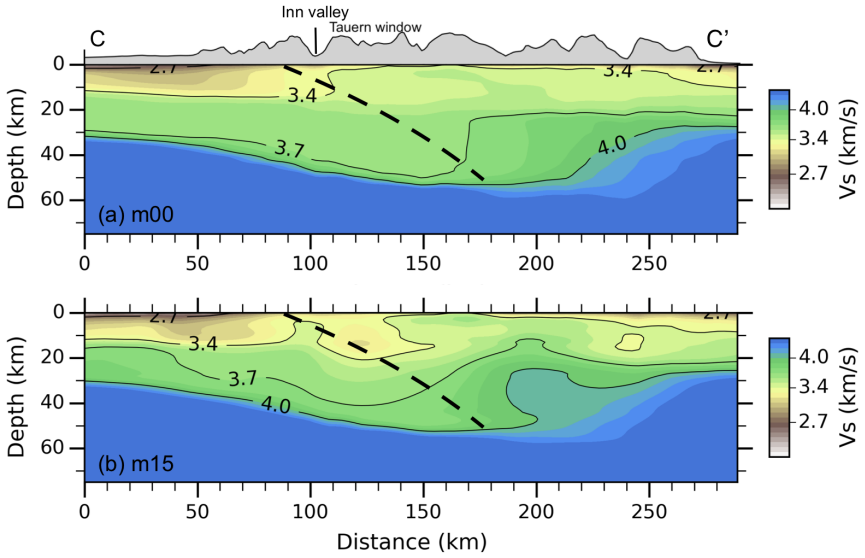

FIGURE 5.11 – Depth-sections along the Transalp seismic profile in the initial (a) and final models (b). The thick black dashed line indicates the Sub-Tauern ramp, which is a south dipping interface between the European (North) and Adriatic plates (South) imaged by deep seismic reflection profiling (Lüschen et al., 2004). The 2.7, 3.4, 3.7 and 4.0 km/s velocity contours roughly depict the bottoms of sedimentary basin, upper crust, middle and lower crust (Moho).

Nonetheless, the shallow Moho related to Ivrea body shows a clear extension towards the Central Alps for the final model. Moreover, the final model presents several Moho bumps those are not shown in the initial model.

M. Malusà (University Milano-Bicocca) provided a preliminary interpretation of the Moho map (Fig. 5.14, based on isovelocity 3.95 km/s). The Moho break (jump) in the NW Alps is very clear. It is less and less marked moving towards the SW.

The Ivrea body (IB) is well imaged. It is disconnected from the Dora-Maira part to the south and bounded to the east by a sharp Moho jump corresponding at the surface with the Val Colla Shear Zone (VCsz) (M. Malusà personal communication). The two blue bumps in the Southern Alps, to the west (VT) and east (AT) of the Giudicarie Line, match with the two main provinces of Permian magmatism : Val Trompia - Val Caffaro (VT) and the Athesian Volcanic Group (AT) (M. Malusà personal communication). The blue bump south of Milano (MB) corresponds to the Monza-Battuda Permian volcanic rocks beneath the Po Plain. (M. Malusà personal communication) A fourth bump is imaged in the northern Adriatic sea. According to M. Malusà, this is the so-called Istria swell (IS) of the Friuli-Dalmatian platform. In general, the Lombardian Basin seems to have a deeper Moho compared to the adjoining Trento Plateau and Monte Generoso

area (MGB). The eastern boundary of this deeper region has a NNE-SSW trend parallel to the Giudicarie Fault, in agreement with stratigraphic data (M. Malusà personal communication).

M. Malusà notice that, in the Northern Apennines, the map images the Ottone-Levanto Fault (OLF) at the boundary between the Apenninic accretionary wedge, to the east, and the tilted strata of the Tertiary Piedmont Basin, to the west. And there is also a Moho jump that marks the boundary between the metamorphic core complexes of the Alpi Apuane (AA) -Monti Pisani (MP), to the north, and a system of NW-SE trending grabens related to the rollback of the Apenninic slab (the Viareggio basin - VB, the Val d'Elsa Graben - GVdE, and the Val di Chiana Graben - GVdC).

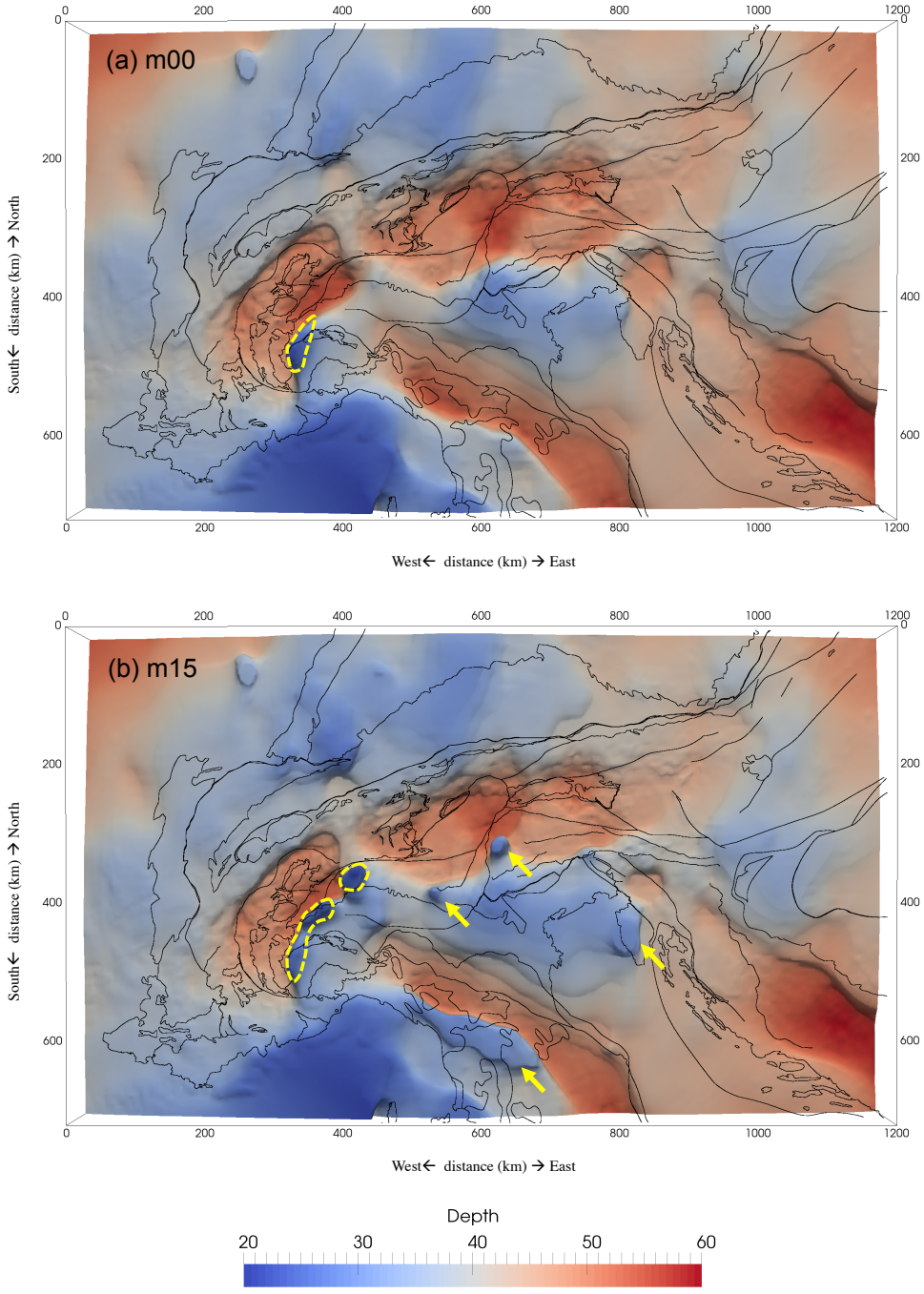

FIGURE 5.12 – Moho depth maps (isovelocity 4 km/s) derived from the initial (a) and final models (b). Yellow dashed lines roughly enclose the Ivrea body, and yellow arrows indicate the Moho bumps.

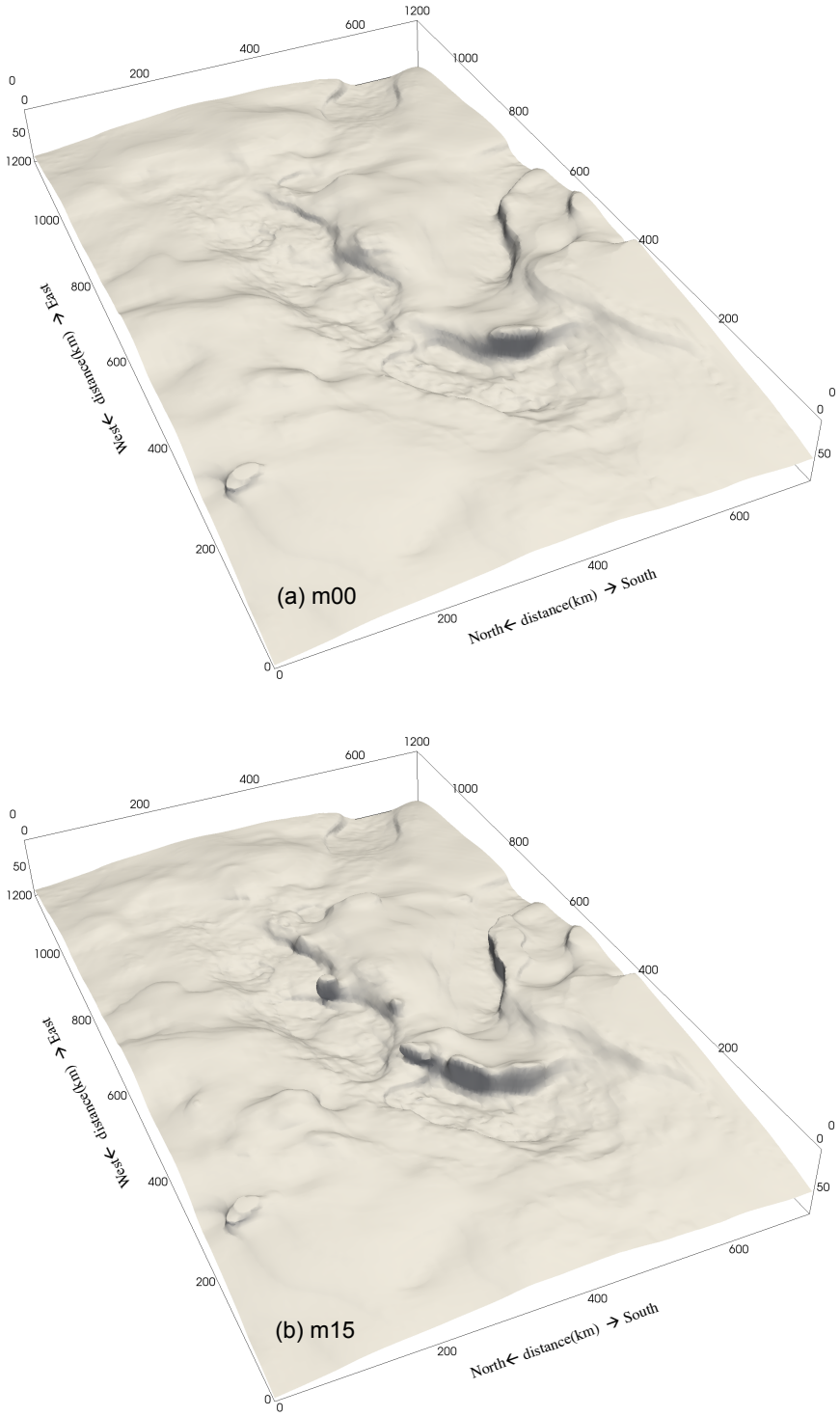

FIGURE 5.13 – 3-D views of the shaded Moho depth maps (isovelocity 4 km/s) derived from the initial (a) and final models (b).

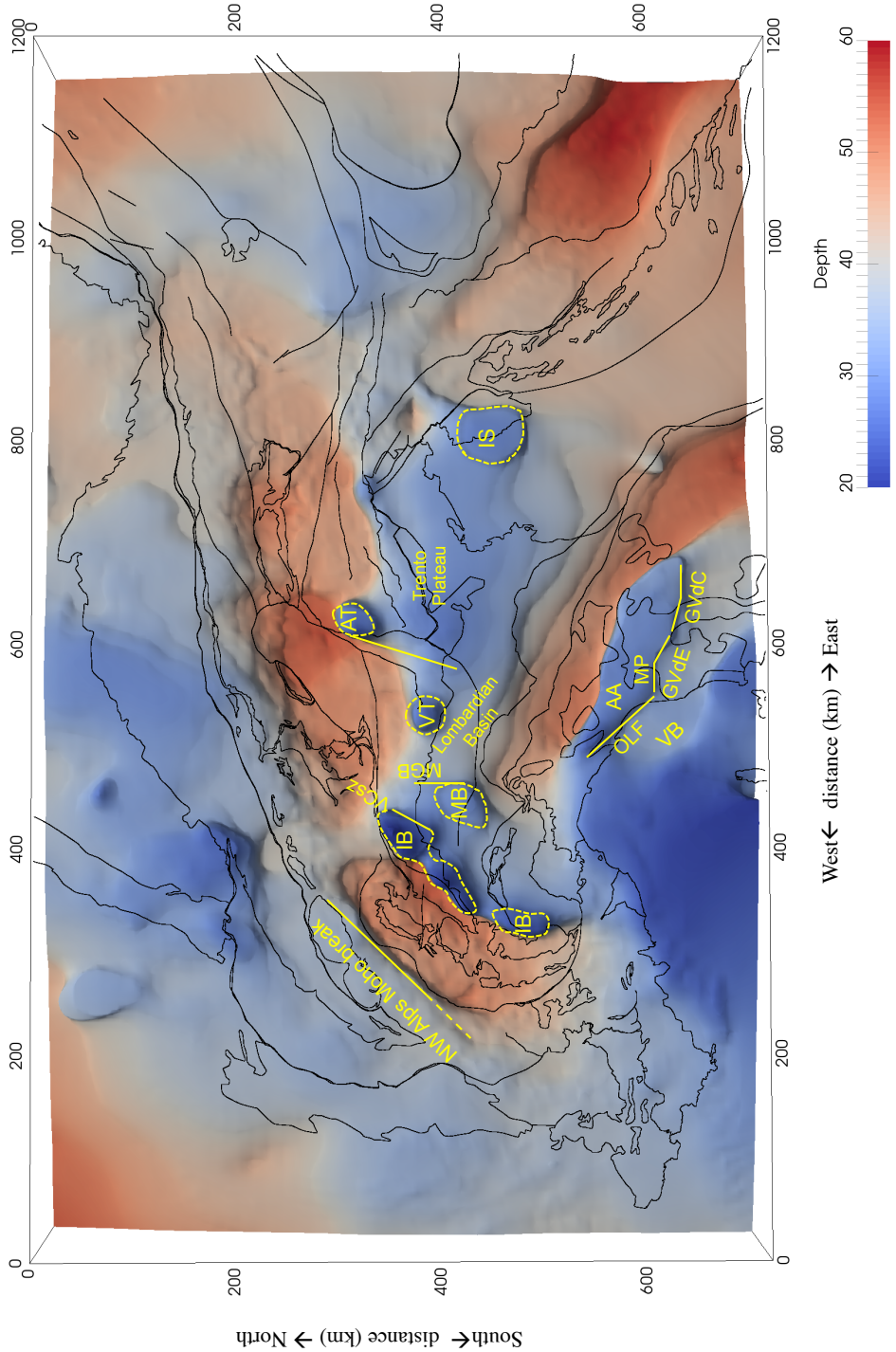

FIGURE 5.14 – 3-D views of the Moho depth map (isovelocity 3.95 km/s) derived from the final model (m15). AA : the Alpi Apuane, AT : the Athesian Volcanic Group, GVdE : the Val d'Elsa Graben, GVdC : the Val di Chiana Graben, IB : the Ivrea body ,IS : the Istria swell, MB : the Monza-Battuda, MGB : the Monte Generoso boundary, MP : the Monti Pisani, OLF : the Ottone-Levanto Fault, VCsz : the Val Colla Shear Zone, VB : the Viareggio basin (interpretation drawn by M. Malusà).

5.1.6 Conclusions

We presented a pioneering application of ambient noise wave-equation tomography of the Alpine crust and uppermost mantle. The so-called 'ambient noise wave-equation tomography' is a new methodology for inverting ambient noise data using 3-D elastic wave-equation based tomography, which fully accounts for 3-D and finite frequency effects. We used cross-correlations of up to four years of continuous vertical-component ambient seismic noise recordings from 304 high-quality broadband stations in the Alpine region. With the initial model *LSP_Eucrust*1.0 derived from traditional ambient noise tomography, we iteratively improved the initial model by minimizing frequency-dependent multitaper traveltime differences between observed and synthetic waveforms in the period range 10-55 s. The synthetic waveforms are calculated with the spectral-element method (SEM), while the gradient of the misfit function is computed with the adjoint-state approach, and the model is updated using the Quasi-Newton l-LBFGS optimization method.

We obtained the final model after 15 iterations with ∼65% of total misfit reduction compared to the initial model. At longer periods (25 and 50 s), the inversion corrected an obvious positive shift of the misfit histograms of initial model. The misfit histograms of final model are symmetric around zero with more concentrated distributions. We confirmed the validity of inversion mainly in the following two aspects : (1) we used a validation dataset to avoid the over-interpretation of data noise ; (2) by analyzing the misfit spatial distribution for the initial and final model, we confirmed that the reduced misfits are primarily isotropic-velocity induced misfits, rather than other factors (for instance, seismic anisotropy and data error).

The resulting crustal and uppermost mantle model reveals several new features. In particular at Moho depth, several Moho localized uplifts related to the Adriatic plate emerged in the final model. Meanwhile, the final model confirmed the Moho jump in the NW Alps. Besides, the final model shows stronger velocity contrasts than the initial model. For instance, at 10 km depth, the velocity contrast between Po plain and Ivrea body is 15-20 % stronger in the final model than that in the initial model.

We believe that this study is important in several senses. First, the resulting model is up-to-now the highest resolution shear-wave velocity model at the Alpine scale. It may be of great use in geological and tectonic studies. Second, while the traditional ambient noise tomography becomes a standard imaging tool nowadays, we prove that the ambient noise wave-equation tomography is an important complementary step to refine the final Vs model. It benefits from the accurate 3-D numerical simulation of seismic wavefields, overcoming the main limitations in the two-step inversion approach employed by traditional ambient noise tomography. Third, our ambient wave-equation noise tomography well imaged the Moho interface in the complex Alpine region using surface waves, which are generally supposed to be not sensitive to interfaces.

As we have mentioned, full waveform inversion of ambient noise correlation data requires a good estimation of noise sources, which is very difficult as the noise sources are

non-stationary in time and space. According to my understanding, further improvements of the study should be dedicated to the following two aspects. First, the ambient noise wave-equation tomography should take into account seismic anisotropy, since we observed obvious azimuthal anisotropy in the Alpine crust from the Eikonal phase velocity tomography study. Second, the use of ambient noise correlations, in combination with earthquake records (in particular P-waves), should better constrain the resulting model.

Chapitre 6

Conclusions and perspectives

With this dissertation, we presented a series of ambient noise tomographic applications in the European region, with a focus on the Alpine crust and uppermost mantle, as well as the Moho interface. The model *LSP_Eucrust*1.0, derived from our ambient noise group velocity tomography, is so far the highest resolution crustal shear-wave velocity model at European scale. Moreover, *LSP_Eucrust*1.0 provides the probability of interfaces, which is of great use in geological interpretation. Using ambient noise Eikonal tomography, we have derived the crustal azimuthal anisotropy maps of the Alpine region, which is the first estimate of crustal anisotropy at the whole Alpine scale. We have also derived the first application of ambient noise wave-equation tomography in the Alpine region. The resulting model showed several new features and stronger velocity contrasts than the initial model *LSP_Eucrust*1.0. It is up-to-now the best-resolved shear-wave velocity model for the Alpine crust and uppermost mantle.

Our study results in a series of models of the Alpine crust and uppermost mantle containing information about shear-wave velocity, Moho depth and azimuthal anisotropy. It provides new available input to better understand the nature of the geodynamic processes of the Alpine orogen. On one hand, the models themselves are self-consistent observations for geological and tectonic interpretation. On the other hand, these models provide reliable initial crustal models for deeper mantle imaging.

With regard to methodology, we proved that the ambient noise wave-equation tomography successfully refined the model obtained from traditional ambient noise tomography using the two-step inversion approach. As full waveform inversion of noise cross-correlations is still far from possible, ambient noise wave-equation tomography might be an important complementary step to widely applied traditional ambient noise tomography. A possible improvement of our ambient noise wave-equation tomography might be taking into account the non-negligible anisotropy, as shown by the Eikonal tomography study. A natural extension of current ambient noise wave-equation tomography is to incorporate earthquake data, since there is no gap between ambient noise and earthquake based WET from a technical point of view, except that FWI (including amplitudes) can be applied to earthquake data as sources are rather well known.

However, the traditional ambient noise tomography is still a necessary and robust method. It is a relative simple method to obtain preliminary results or build initial model for the following ambient noise wave-equation tomography. It is in particular useful for applications at large scale, where ambient noise wave-equation tomography can not be done due to the computational cost. The method can be further enhanced by the joint inversion of surface waves and receiver functions, since surface waves are more sensitive to medium velocity, while receiver functions provide better constrains on medium interfaces.

Origin of data

Waveform data used in this study belong to the permanent networks with codes AC, BA, BE (Royal Observatory of Belgium, 1985), BN, BS, BW (Department of Earth and Environmental Sciences, Geophysical Observatory, University of Munchen, 2001), CA (Institut Cartogràfic i Geològic de Catalunya-Institut d'Estudis Catalans, 1996), CH (Swiss Seismological Service (SED) at ETH Zürich, 1983), CL (Corinth Rift Laboratory Team And RESIF Datacenter, 2013), CQ (Geological Survey Department Cyprus, 2013), CR, CZ (Institute of Geophysics, Academy of Sciences of the Czech Republic, 1973), DK, DZ, EB, EE, EI (INSN, 1993), ES, FN, FR (RESIF, 1995), G (Institut De Physique Du Globe De Paris (IPGP), & Ecole Et Observatoire Des Sciences De La Terre De Strasbourg (EOST), 1982), GB, GE (GEOFON Data Centre, 1993), GR, GU (University of Genova, 1967), HC (Technological Educational Institute of Crete, 2006), HE, HL (National Observatory of Athens, Institute of Geodynamics, Athens, 1997), HP (University of Patras, Geology Department, Seismological Laboratory, 2000), HT (Aristotle University of Thessaloniki Seismological Network, 1981), HU (Kövesligethy Radó Seismological Observatory, 1992), IB (Institute Earth Sciences "Jaume Almera" CSIC (ICTJA Spain), 2007), II (Scripps Institution of Oceanography, 1986), IP, IS, IU (Albuquerque Seismological Laboratory (ASL)/USGS, 1988), IV (INGV Seismological Data Centre, 2006), IX, KO (Bogazici University Kandilli Observatory And Earthquake Research Institute, 2001), LC, LX, MD, MN (MedNet Project Partner Institutions, 1990), MT, NI (OGS (Istituto Nazionale di Oceanografia e di Geofisica Sperimentale) and University of Trieste, 2002), NL (KNMI, 1993), NO, NS, OE, PL, PM, RD, RO (National Institute for Earth Physics (NIEP Romania), 1994), SI, SJ, SK (ESI SAS (Earth Science Institute Of The Slovak Academy Of Sciences), 2004), SL (Slovenian Environment Agency, 2001), SS, ST (Geological Survey-Provincia Autonoma di Trento, 1981), SX (Leipzig University, 2001), TH, TT, TU, UP (SNSN, 1904), WM (San Fernando Royal Naval Observatory (ROA), Universidad Complutense De Madrid (UCM), Helmholtz-Zentrum Potsdam Deutsches

GeoForschungsZentrum (GFZ), Universidade De Evora (UEVORA, Portugal), & Institute Scientifique of RABAT (ISRABAT, Morocco), 1996). We also used data of temporary experiments, namely AlpArray (network code Z3_2015 ; AlpArray Seismic Network, 2015), CIFALPS (network code YP_2012 ; Zhao et al., 2016), PYROPE (network code X7_2010 ; Chevrot et al., 2017).

Bibliographie

Aki, K. (1957). Space and time spectra of stationary stochastic waves with special reference to microtremors. *Bull. Earthq. Res. Inst.*, 35 :415–456.

Barruol, G., Bonnin, M., Pedersen, H., Bokelmann, G. H., and Tiberi, C. (2011). Belt-parallel mantle flow beneath a halted continental collision : The Western Alps. *Earth Planet. Sci. Lett.*, 302(3-4) :429–438.

Barruol, G., Deschamps, A., and Coutant, O. (2004). Mapping upper mantle anisotropy beneath SE France by SKS splitting indicates Neogene asthenospheric flow induced by Apenninic slab roll-back and deflected by the deep Alpine roots. *Tectonophysics*, 394(1-2) :125–138.

Bensen, G. D., Ritzwoller, M. H., Barmin, M. P., Levshin, A. L., Lin, F., Moschetti, M. P., Shapiro, N. M., and Yang, Y. (2007). Processing seismic ambient noise data to obtain reliable broad-band surface wave dispersion measurements. *Geophys. J. Int.*, 169(3) :1239–1260.

Bensen, G. D., Ritzwoller, M. H., and Yang, Y. (2009). A 3-D shear velocity model of the crust and uppermost mantle beneath the United States from ambient seismic noise. *Geophys. J. Int.*, 177(3) :1177–1196.

Birch, F. (1961). The velocity of compressional waves in rocks to 10 kilobars : 2. *J. Geophys. Res.*, 66(7) :2199–2224.

Bloch, S. and Hales, A. (1968). New techniques for the determination of surface wave phase velocities. *Bull. Seismol. Soc. Am.*, 58(3) :1021–1034.

Bodin, T., Sambridge, M., Rawlinson, N., and Arroucau, P. (2012a). Transdimensional tomography with unknown data noise. *Geophys. J. Int.*, 189(3) :1536–1556.

Bodin, T., Sambridge, M., Tkalčić, H., Arroucau, P., Gallagher, K., and Rawlinson, N. (2012b). Transdimensional inversion of receiver functions and surface wave dispersion. *J. Geophys. Res. Solid Earth*, 117(B2) :B02301.

Bokelmann, G., Qorbani, E., and Bianchi, I. (2013). Seismic anisotropy and large-scale deformation of the Eastern Alps. *Earth Planet. Sci. Lett.*, 383 :1–6.

Boschi, L. and Dziewonski, A. M. (1999). High- and low-resolution images of the Earth's mantle : Implications of different approaches to tomographic modeling. *J. Geophys. Res.*, 104(B11) :25567–25594.

Boschi, L., Fry, B., Ekström, G., and Giardini, D. (2009). The European Upper Mantle as Seen by Surface Waves. *Surv. Geophys.*, 30(4-5) :463–501.

Boschi, L., Weemstra, C., Verbeke, J., Ekström, G., Zunino, A., and Giardini, D. (2013). On measuring surface wave phase velocity from station–station cross-correlation of ambient signal. *Geophys. J. Int.*, 192(1) :346–358.

Boué, P., Poli, P., Campillo, M., Pedersen, H., Briand, X., and Roux, P. (2013). Teleseismic correlations of ambient seismic noise for deep global imaging of the Earth. *Geophys. J. Int.*, 194(2) :844–848.

Boué, P., Poli, P., Campillo, M., and Roux, P. (2014a). Reverberations, coda waves and ambient noise : Correlations at the global scale and retrieval of the deep phases. *Earth Planet. Sci. Lett.*, 391 :137–145.

Boué, P., Roux, P., Campillo, M., and Briand, X. (2014b). Phase velocity tomography of surface waves using ambient noise cross correlation and array processing. *J. Geophys. Res. Solid Earth*, 119(1) :519–529.

Brenguier, F., Campillo, M., Hadziioannou, C., Shapiro, N. M., Nadeau, R. M., and Larose, E. (2008a). Postseismic Relaxation Along the San Andreas Fault at Parkfield from Continuous Seismological Observations. *Science (80-.).*, 321(5895) :1478–1481.

Brenguier, F., Shapiro, N. M., Campillo, M., Ferrazzini, V., Duputel, Z., Coutant, O., and Nercessian, A. (2008b). Towards forecasting volcanic eruptions using seismic noise. *Nat. Geosci.*, 1(2) :126–130.

Brenguier, F., Shapiro, N. M., Campillo, M., Nercessian, A., and Ferrazzini, V. (2007). 3-D surface wave tomography of the Piton de la Fournaise volcano using seismic noise correlations. *Geophys. Res. Lett.*, 34(2) :L02305.

Brocher, T. M. (2005). Empirical Relations between Elastic Wavespeeds and Density in the Earth's Crust. *Bull. Seismol. Soc. Am.*, 95(6) :2081–2092.

Campillo, M. (2006). Phase and correlation in 'random' seismic fields and the reconstruction of the green function. *Pure Appl. Geophys.*, 163(2-3) :475–502.

Campillo, M. and Paul, A. (2003). Long-Range Correlations in the Diffuse Seismic Coda. *Science (80-.).*, 299(5606) :547–549.

Campillo, M. and Roux, P. (2015). Crust and Lithospheric Structure - Seismic Imaging and Monitoring with Ambient Noise Correlations. In *Treatise Geophys.*, pages 391–417. Elsevier.

Chen, M., Huang, H., Yao, H., van der Hilst, R., and Niu, F. (2014). Low wave speed zones in the crust beneath SE Tibet revealed by ambient noise adjoint tomography. *Geophys. Res. Lett.*, 41(2) :334–340.

Chen, M. and Tromp, J. (2007). Theoretical and numerical investigations of global and regional seismic wave propagation in weakly anisotropic earth models. *Geophys. J. Int.*, 168(3) :1130–1152.

Claerbout, J. F. (1968). Synthesis of a layered medium from its acoustic transmission response. *GEOPHYSICS*, 33(2) :264–269.

Closs, H. and Labrouste, Y. (1963). *Recherches séismologiques dans les Alpes occidentales au moyen de grandes explosions en 1956, 1958 et 1960, mémoire collectif du Groupe d'études des explosions alpines.* Centre national de la recherche scientifique, Paris.

Cox, H. (1973). Spatial correlation in arbitrary noise fields with application to ambient sea noise. *J. Acoust. Soc. Am.*, 54(5) :1289–1301.

Crampin, S. (1994). The fracture criticality of crustal rocks. *Geophys. J. Int.*, 118(2) :428–438.

Cupillard, P., Delavaud, E., Burgos, G., Festa, G., Vilotte, J. P., Capdeville, Y., and Montagner, J. P. (2012). RegSEM : A versatile code based on the spectral element

method to compute seismic wave propagation at the regional scale. *Geophys. J. Int.*, 188(3) :1203–1220.

Derode, A., Larose, E., Campillo, M., and Fink, M. (2003a). How to estimate the Green's function of a heterogeneous medium between two passive sensors ? Application to acoustic waves. *Appl. Phys. Lett.*, 83(15) :3054–3056.

Derode, A., Larose, E., Tanter, M., de Rosny, J., Tourin, A., Campillo, M., and Fink, M. (2003b). Recovering the Green's function from field-field correlations in an open scattering medium (L). *J. Acoust. Soc. Am.*, 113(6) :2973.

Dèzes, P., Schmid, S., and Ziegler, P. (2004). Evolution of the European Cenozoic Rift System : interaction of the Alpine and Pyrenean orogens with their foreland lithosphere. *Tectonophysics*, 389(1-2) :1–33.

Diehl, T., Husen, S., Kissling, E., and Deichmann, N. (2009). High-resolution 3-D P -wave model of the Alpine crust. *Geophys. J. Int.*, 179(2) :1133–1147.

Draganov, D., Campman, X., Thorbecke, J., Verdel, A., and Wapenaar, K. (2009). Reflection images from ambient seismic noise. *GEOPHYSICS*, 74(5) :A63–A67.

Dziewonski, a., Bloch, S., and Landisman, M. (1969). A technique for the analysis of transient seismic signals. *Bull. Seismol. Soc. Am.*, 59(1) :427–444.

Dziewonski, A. M. and Anderson, D. L. (1981). Preliminary reference Earth model. *Phys. Earth Planet. Inter.*, 25(4) :297–356.

Ekström, G., Abers, G. A., and Webb, S. C. (2009). Determination of surface-wave phase velocities across USArray from noise and Aki's spectral formulation. *Geophys. Res. Lett.*, 36(18) :L18301.

Fichtner, A. (2014). Source and processing effects on noise correlations. *Geophys. J. Int.*, 197(3) :1527–1531.

Fichtner, A., Kennett, B. L. N., Igel, H., and Bunge, H.-P. (2009). Full seismic waveform tomography for upper-mantle structure in the Australasian region using adjoint methods. *Geophys. J. Int.*, 179(3) :1703–1725.

Fichtner, A. and Villaseñor, A. (2015). Crust and upper mantle of the western Mediterranean – Constraints from full-waveform inversion. *Earth Planet. Sci. Lett.*, 428 :52–62.

Friederich, W., Hunzinger, S., and Wielandt, E. (2000). A note on the interpretation of seismic surface waves over three - dimensional structures. *Geophys. J. Int.*, 143(2) :335–339.

Froment, B., Campillo, M., Chen, J., and Liu, Q. (2013). Deformation at depth associated with the 12 May 2008 MW 7.9 Wenchuan earthquake from seismic ambient noise monitoring. *Geophys. Res. Lett.*, 40(1) :78–82.

Froment, B., Campillo, M., Roux, P., Gouédard, P., Verdel, A., and Weaver, R. L. (2010). Estimation of the effect of nonisotropically distributed energy on the apparent arrival time in correlations. *GEOPHYSICS*, 75(5) :SA85–SA93.

Fry, B., Deschamps, F., Kissling, E., Stehly, L., and Giardini, D. (2010). Layered azimuthal anisotropy of Rayleigh wave phase velocities in the European Alpine lithosphere inferred from ambient noise. *Earth Planet. Sci. Lett.*, 297(1-2) :95–102.

Gao, H. and Shen, Y. (2014). Upper mantle structure of the Cascades from full-wave ambient noise tomography : Evidence for 3D mantle upwelling in the back-arc. *Earth Planet. Sci. Lett.*, 390 :222–233.

Grad, M. and Tiira, T. (2009). The Moho depth map of the European Plate. *Geophys. J. Int.*, 176(1) :279–292.

Graves, R. W. (1996). Simulating seismic wave propagation in 3D elastic media using staggered-grid finite differences. *Bull. Seismol. Soc. Am.*, 86(4) :1091–1106.

Gung, Y. and Romanowicz, B. (2004). Q tomography of the upper mantle using three-component long-period waveforms. *Geophys. J. Int.*, 157(2) :813–830.

Handy, M. R., M. Schmid, S., Bousquet, R., Kissling, E., and Bernoulli, D. (2010). Reconciling plate-tectonic reconstructions of Alpine Tethys with the geological–geophysical record of spreading and subduction in the Alps. *Earth-Science Rev.*, 102(3-4) :121–158.

Haned, A., Stutzmann, E., Schimmel, M., Kiselev, S., Davaille, A., and Yelles-Chaouche, A. (2016). Global tomography using seismic hum. *Geophys. J. Int.*, 204(2) :1222–1236.

Hansen, P. (2001). The L-curve and its use in the numerical treatment of inverse problems. In Johnston, P., editor, *Comput. Inverse Probl. Electrocardiogr.*, volume 5, pages 119–142. WIT Press, Southampton.

Hasselmann, K. (1963). A statistical analysis of the generation of microseisms. *Rev. Geophys.*, 1(2) :177.

Herrmann, R. B. (1973). Some aspects of band-pass filtering of surface waves. *Bull. Seismol. Soc. Am.*, 63(2) :663–671.

Herrmann, R. B. (2013). Computer Programs in Seismology : An Evolving Tool for Instruction and Research. *Seismol. Res. Lett.*, 84(6) :1081–1088.

Hetényi, G., Molinari, I., Clinton, J., Bokelmann, G., Bondár, I., Crawford, W. C., Dessa, J.-X., Doubre, C., Friederich, W., Fuchs, F., Giardini, D., Gráczer, Z., Handy, M. R., Herak, M., Jia, Y., Kissling, E., Kopp, H., Korn, M., Margheriti, L., Meier, T., Mucciarelli, M., Paul, A., Pesaresi, D., Piromallo, C., Plenefisch, T., Plomerová, J., Ritter, J., Rümpker, G., Šipka, V., Spallarossa, D., Thomas, C., Tilmann, F., Wassermann, J., Weber, M., Wéber, Z., Wesztergom, V., and Živčić, M. (2018). The AlpArray Seismic Network : A Large-Scale European Experiment to Image the Alpine Orogen. *Surv. Geophys.*, 39(5) :1009–1033.

Hillers, G., Ben-Zion, Y., Campillo, M., and Zigone, D. (2015a). Seasonal variations of seismic velocities in the San Jacinto fault area observed with ambient seismic noise. *Geophys. J. Int.*, 202(2) :920–932.

Hillers, G., Graham, N., Campillo, M., Kedar, S., Landés, M., and Shapiro, N. (2012). Global oceanic microseism sources as seen by seismic arrays and predicted by wave action models. *Geochemistry, Geophys. Geosystems*, 13(1).

Hillers, G., Retailleau, L., Campillo, M., Inbal, A., Ampuero, J.-P., and Nishimura, T. (2015b). In situ observations of velocity changes in response to tidal deformation from analysis of the high-frequency ambient wavefield. *J. Geophys. Res. Solid Earth*, 120(1) :210–225.

Huang, H.-H., Lin, F.-C., Tsai, V. C., and Koper, K. D. (2015). High-resolution probing of inner core structure with seismic interferometry. *Geophys. Res. Lett.*, 42(24) :10,622–10,630.

Kedar, S., Longuet-Higgins, M., Webb, F., Graham, N., Clayton, R., and Jones, C. (2008). The origin of deep ocean microseisms in the North Atlantic Ocean. *Proc. R. Soc. A Math. Phys. Eng. Sci.*, 464(2091) :777–793.

Komatitsch, D. and Tromp, J. (1999). Introduction to the spectral element method for three-dimensional seismic wave propagation. *Geophys. J. Int.*, 139(3) :806–822.

Komatitsch, D. and Tromp, J. (2002a). Spectral-element simulations of global seismic wave propagation-I. Validation. *Geophys. J. Int.*, 149(2) :390–412.

Komatitsch, D. and Tromp, J. (2002b). Spectral-element simulations of global seismic wave propagation-II. Three-dimensional models, oceans, rotation and self-gravitation. *Geophys. J. Int.*, 150(1) :303–318.

Komatitsch, D. and Vilotte, J. P. (1998). The spectral element method : An efficient tool to simulate the seismic response of 2D and 3D geological structures. *Bull. Seismol. Soc. Am.*, 88(2) :368–392.

Kummerow, J. and Kind, R. (2006). Shear wave splitting in the Eastern Alps observed at the TRANSALP network. *Tectonophysics*, 414(1-4) :117–125.

Kummerow, J., Kind, R., Oncken, O., Giese, P., Ryberg, T., Wylegalla, K., and Scherbaum, F. (2004). A natural and controlled source seismic profile through the Eastern Alps : TRANSALP. *Earth Planet. Sci. Lett.*, 225(1-2) :115–129.

Landisman, M., Dziewonski, A., and Satô, Y. (1969). Recent Improvements in the Analysis of Surface Wave Observations. *Geophys. J. Int.*, 17(4) :369–403.

Larose, E., Margerin, L., Derode, A., van Tiggelen, B., Campillo, M., Shapiro, N., Paul, A., Stehly, L., and Tanter, M. (2006). Correlation of random wavefields : An interdisciplinary review. *Geophysics*, 71(4) :SI11–SI21.

Laske, G., Masters, G., Ma, Z., and Pasyanos, M. (2013). Update on CRUST1.0 -A 1-degree Global Model of Earth's Crust. In *Geophys. Res. Abstr. EGU Gen. Assem.*, volume 15, pages 2013–2658. Abstract EGU2013-2658.

Legendre, C. P., Meier, T., Lebedev, S., Friederich, W., and Viereck-Götte, L. (2012). A shear wave velocity model of the European upper mantle from automated inversion of seismic shear and surface waveforms. *Geophys. J. Int.*, 191(1) :282–304.

Levshin, A. L., Yanovskaya, T. B., Lander, A. V., Bukchin, B. G., Barmin, M. P., Ratnikova, L. I., and Its, E. N. (1989). *Seismic Surface Waves in a Laterally Inhomogeneous Earth*, volume 9 of *Modern Approaches in Geophysics*. Springer Netherlands, Dordrecht.

Li, H., Bernardi, F., and Michelini, A. (2010). Surface wave dispersion measurements from ambient seismic noise analysis in Italy. *Geophys. J. Int.*, 180(3) :1242–1252.

Lin, F.-C. and Ritzwoller, M. H. (2011a). Apparent anisotropy in inhomogeneous isotropic media. *Geophys. J. Int.*, 186(3) :1205–1219.

Lin, F.-C. and Ritzwoller, M. H. (2011b). Helmholtz surface wave tomography for isotropic and azimuthally anisotropic structure. *Geophys. J. Int.*, 186(3) :1104–1120.

Lin, F.-C., Ritzwoller, M. H., and Snieder, R. (2009). Eikonal tomography : surface wave tomography by phase front tracking across a regional broad-band seismic array. *Geophys. J. Int.*, 177(3) :1091–1110.

Lin, F.-C., Tsai, V. C., Schmandt, B., Duputel, Z., and Zhan, Z. (2013). Extracting seismic core phases with array interferometry. *Geophys. Res. Lett.*, 40(6) :1049–1053.

Lippitsch, R. (2003). Upper mantle structure beneath the Alpine orogen from high-resolution teleseismic tomography. *J. Geophys. Res.*, 108(B8) :2376.

Liu, Q. and Gu, Y. (2012). Seismic imaging : From classical to adjoint tomography. *Tectonophysics*, 566-567 :31–66.

Liu, Q. and Tromp, J. (2006). Finite-Frequency Kernels Based on Adjoint Methods. *Bull. Seismol. Soc. Am.*, 96(6) :2383–2397.

Liu, Y., Niu, F., Chen, M., and Yang, W. (2017). 3-D crustal and uppermost mantle structure beneath NE China revealed by ambient noise adjoint tomography. *Earth Planet. Sci. Lett.*, 461 :20–29.

Lobkis, O. I. and Weaver, R. L. (2001). On the emergence of the Green's function in the correlations of a diffuse field. *J. Acoust. Soc. Am.*, 110(6) :3011–3017.

Lobkis, O. I. and Weaver, R. L. (2003). Coda-Wave Interferometry in Finite Solids : Recovery of P-to-S Conversion Rates in an Elastodynamic Billiard. *Phys. Rev. Lett.*, 90(25) :254302.

Longuet-Higgins, M. S. (1950). A Theory of the Origin of Microseisms. *Philos. Trans. R. Soc. A Math. Phys. Eng. Sci.*, 243(857) :1–35.

Lu, Y., Stehly, L., and Paul, A. (2018). High-resolution surface wave tomography of the European crust and uppermost mantle from ambient seismic noise. *Geophys. J. Int.*, 214(2) :1136–1150.

Ludwig, W., Nafe, J., and Drake, C. (1970). Seismic refraction. In *Sea*, volume 4, pages 53–84. Wiley-Interscience.

Luo, Y. and Schuster, G. T. (1991). Wave equation traveltime inversion. *GEOPHYSICS*, 56(5) :645–653.

Lüschen, E., Lammerer, B., Gebrande, H., Millahn, K., and Nicolich, R. (2004). Orogenic structure of the Eastern Alps, Europe, from TRANSALP deep seismic reflection profiling. *Tectonophysics*, 388(1-4) :85–102.

Macquet, M., Paul, A., Pedersen, H. A., Villaseñor, A., Chevrot, S., Sylvander, M., and Wolyniec, D. (2014). Ambient noise tomography of the Pyrenees and the surrounding regions : inversion for a 3-D Vs model in the presence of a very heterogeneous crust. *Geophys. J. Int.*, 199(1) :402–415.

Métivier, L. and Brossier, R. (2016). The SEISCOPE optimization toolbox : A large-scale nonlinear optimization library based on reverse communication. *GEOPHYSICS*, 81(2) :F1–F15.

Molinari, I. and Morelli, A. (2011). EPcrust : a reference crustal model for the European Plate. *Geophys. J. Int.*, 185(1) :352–364.

Molinari, I., Verbeke, J., Boschi, L., Kissling, E., and Morelli, A. (2015). Italian and Alpine three-dimensional crustal structure imaged by ambient-noise surface-wave dispersion. *Geochemistry, Geophys. Geosystems*, 16(12) :4405–4421.

Mora, P. (1987). Nonlinear two dimensional elastic inversion of multioffset seismic data. *GEOPHYSICS*, 52(9) :1211–1228.

Mordret, A., Shapiro, N. M., Singh, S. S., Roux, P., and Barkved, O. I. (2013). Helmholtz tomography of ambient noise surface wave data to estimate Scholte wave phase velocity at Valhall Life of the Field. *GEOPHYSICS*, 78(2) :WA99–WA109.

Nakata, N., Chang, J. P., Lawrence, J. F., and Boué, P. (2015). Body wave extraction and tomography at Long Beach, California, with ambient-noise interferometry. *J. Geophys. Res. Solid Earth*, 120(2) :1159–1173.

Nicolas, A., Hirn, A., Nicolich, R., and Polino, R. (1990). Lithospheric wedging in the western Alps inferred from the ECORS-CROP traverse. *Geology*, 18(7) :587.

Nicolson, H., Curtis, A., Baptie, B., and Galetti, E. (2012). Seismic interferometry and ambient noise tomography in the British Isles. *Proc. Geol. Assoc.*, 123(1) :74–86.

Nishida, K. (2013). Global propagation of body waves revealed by cross-correlation analysis of seismic hum. *Geophys. Res. Lett.*, 40(9) :1691–1696.

Nishida, K., Montagner, J.-P., and Kawakatsu, H. (2009). Global Surface Wave Tomography Using Seismic Hum. *Science (80-.).*, 326(5949) :112–112.

Nocedal, J. (1980). Updating Quasi-Newton Matrices with Limited Storage. *Math. Comput.*, 35(151) :773.

O'Connell, R. J. and Budiansky, B. (1974). Seismic velocities in dry and saturated cracked solids. *J. Geophys. Res.*, 79(35) :5412–5426.

Operto, S., Virieux, J., Amestoy, P., L'Excellent, J.-Y., Giraud, L., and Ali, H. B. H. (2007). 3D finite-difference frequency-domain modeling of visco-acoustic wave propagation using a massively parallel direct solver : A feasibility study. *GEOPHYSICS*, 72(5) :SM195–SM211.

Paige, C. C. and Saunders, M. A. (1982). LSQR : An Algorithm for Sparse Linear Equations and Sparse Least Squares. *ACM Trans. Math. Softw.*, 8(1) :43–71.

Paul, A., Cattaneo, M., Thouvenot, F., Spallarossa, D., Béthoux, N., and Fréchet, J. (2001). A three-dimensional crustal velocity model of the southwestern Alps from local earthquake tomography. *J. Geophys. Res. Solid Earth*, 106(B9) :19367–19389.

Pedersen, H. A. and Krüger, F. (2007). Influence of the seismic noise characteristics on noise correlations in the Baltic shield. *Geophys. J. Int.*, 168(1) :197–210.

Pfiffner, O. A., Lehner, P., Heitzmann, P., Mueller, S., and Steck, A. (1997). *Deep structure of the Swiss Alps : results of NRP 20*. Birkhäuser, Basel, Switzerland.

Pharaoh, T. (1999). Palaeozoic terranes and their lithospheric boundaries within the Trans-European Suture Zone (TESZ) : a review. *Tectonophysics*, 314(1-3) :17–41.

Piana Agostinetti, N. and Amato, A. (2009). Moho depth and V p / V s ratio in peninsular Italy from teleseismic receiver functions. *J. Geophys. Res.*, 114(B6) :B06303.

Picozzi, M., Parolai, S., Bindi, D., and Strollo, A. (2009). Characterization of shallow geology by high-frequency seismic noise tomography. *Geophys. J. Int.*, 176(1) :164–174.

Piromallo, C. and Faccenna, C. (2004). How deep can we find the traces of Alpine subduction ? *Geophys. Res. Lett.*, 31(6) :n/a–n/a.

Platt, J. (2007). From orogenic hinterlands to Mediterranean-style back-arc basins : a comparative analysis. *J. Geol. Soc. London.*, 164(2) :297–311.

Plessix, R.-E. (2006). A review of the adjoint-state method for computing the gradient of a functional with geophysical applications. *Geophys. J. Int.*, 167(2) :495–503.

Poli, P., Campillo, M., and Pedersen, H. (2012). Body-Wave Imaging of Earth's Mantle Discontinuities from Ambient Seismic Noise. *Science (80-.).*, 338(6110) :1063–1065.

Poli, P., Thomas, C., Campillo, M., and Pedersen, H. A. (2015). Imaging the D″ reflector with noise correlations. *Geophys. Res. Lett.*, 42(1) :60–65.

Poupinet, G., Ellsworth, W. L., and Frechet, J. (1984). Monitoring velocity variations in the crust using earthquake doublets : An application to the Calaveras Fault, California. *J. Geophys. Res. Solid Earth*, 89(B7) :5719–5731.

Qorbani, E., Bianchi, I., and Bokelmann, G. (2015). Slab detachment under the Eastern Alps seen by seismic anisotropy. *Earth Planet. Sci. Lett.*, 409 :96–108.

Rawlinson, N., Fichtner, A., Sambridge, M., and Young, M. K. (2014). Seismic Tomography and the Assessment of Uncertainty. *Adv. Geophys.*, 55 :1–76.

Reasenberg, P. and Aki, K. (1974). A precise, continuous measurement of seismic velocity for monitoring in situ stress. *J. Geophys. Res.*, 79(2) :399–406.

Roux, P., Sabra, K. G., Gerstoft, P., Kuperman, W. A., and Fehler, M. C. (2005). P-waves from cross-correlation of seismic noise. *Geophys. Res. Lett.*, 32(19) :L19303.

Sager, K., Ermert, L., Boehm, C., and Fichtner, A. (2018). Towards full waveform ambient noise inversion. *Geophys. J. Int.*, 212(1) :566–590.

Salimbeni, S., Malusà, M. G., Zhao, L., Guillot, S., Pondrelli, S., Margheriti, L., Paul, A., Solarino, S., Aubert, C., Dumont, T., Schwartz, S., Wang, Q., Xu, X., Zheng,

T., and Zhu, R. (2018). Active and fossil mantle flows in the western Alpine region unravelled by seismic anisotropy analysis and high-resolution P wave tomography. *Tectonophysics*, 731-732 :35–47.

Salimbeni, S., Pondrelli, S., and Margheriti, L. (2013). Hints on the deformation penetration induced by subductions and collision processes : Seismic anisotropy beneath the Adria region (Central Mediterranean). *J. Geophys. Res. Solid Earth*, 118(11) :5814–5826.

Sánchez-Sesma, F. J., Pérez-Ruiz, J. A., Campillo, M., and Luzón, F. (2006). Elastodynamic 2D Green function retrieval from cross-correlation : Canonical inclusion problem. *Geophys. Res. Lett.*, 33(13) :L13305.

Savage, M. K. (1999). Seismic anisotropy and mantle deformation : What have we learned from shear wave splitting ? *Rev. Geophys.*, 37(1) :65–106.

Saygin, E. and Kennett, B. L. N. (2012). Crustal structure of Australia from ambient seismic noise tomography. *J. Geophys. Res. Solid Earth*, 117(B1) :n/a–n/a.

Schaefer, J. F., Boschi, L., and Kissling, E. (2011). Adaptively parametrized surface wave tomography : Methodology and a new model of the European upper mantle. *Geophys. J. Int.*, 186(3) :1431–1453.

Schivardi, R. and Morelli, A. (2011). EPmantle : a 3-D transversely isotropic model of the upper mantle under the European Plate. *Geophys. J. Int.*, 185(1) :469–484.

Sénéchal, G. and Thouvenot, F. (1991). Geometrical migration of line-drawings : A simplified method applied to ECORS data. In *Cont. Lithosph. Deep Seism. Reflections*, volume 2, pages 401–407.

Sens-Schönfelder, C. and Wegler, U. (2006). Passive image interferometry and seasonal variations of seismic velocities at Merapi Volcano, Indonesia. *Geophys. Res. Lett.*, 33(21) :L21302.

Shapiro, N. M. and Campillo, M. (2004). Emergence of broadband Rayleigh waves from correlations of the ambient seismic noise. *Geophys. Res. Lett.*, 31(7) :n/a–n/a.

Shapiro, N. M., Campillo, M., Stehly, L., and Ritzwoller, M. H. (2005). High-Resolution Surface-Wave Tomography from Ambient Seismic Noise. *Science (80-.).*, 307(5715) :1615–1618.

Shen, W., Ritzwoller, M. H., Schulte-Pelkum, V., and Lin, F. C. (2013). Joint inversion of surface wave dispersion and receiver functions : A Bayesian Monte-Carlo approach. *Geophys. J. Int.*, 192(2) :807–836.

Shen, W. S. and Ritzwoller, M. H. (2014). *Baysian Monte Carlo inversion of multiple data sets to image the crust and uppermost mantle structure beneath the continental United States*. PhD thesis.

Silver, P. G. (1996). SEISMIC ANISOTROPY BENEATH THE CONTINENTS : Probing the Depths of Geology. *Annu. Rev. Earth Planet. Sci.*, 24(1) :385–432.

Slepian, D. and Pollak, H. O. (1961). Prolate Spheroidal Wave Functions, Fourier Analysis and Uncertainty — I. *Bell Syst. Tech. J.*

Smith, M. L. and Dahlen, F. A. (1973). The azimuthal dependence of Love and Rayleigh wave propagation in a slightly anisotropic medium. *J. Geophys. Res.*, 78(17) :3321–3333.

Snieder, R. (1986). 3D linearized scattering of surface waves and a formalism for surface wave holography. *Geophys. J. Int.*, 84(3) :581–605.

Snieder, R. (2004). Extracting the Green's function from the correlation of coda waves : A derivation based on stationary phase. *Phys. Rev. E*, 69(4) :046610.

Snieder, R. and Larose, E. (2013). Extracting Earth's Elastic Wave Response from Noise Measurements. *Annu. Rev. Earth Planet. Sci.*, 41(1) :183–206.

Solarino, S., Malusà, M. G., Eva, E., Guillot, S., Paul, A., Schwartz, S., Zhao, L., Aubert, C., Dumont, T., Pondrelli, S., Salimbeni, S., Wang, Q., Xu, X., Zheng, T., and Zhu, R. (2018). Mantle wedge exhumation beneath the Dora-Maira (U)HP dome unravelled by local earthquake tomography (Western Alps). *Lithos*, 296-299 :623–636.

Spada, M., Bianchi, I., Kissling, E., Agostinetti, N. P., and Wiemer, S. (2013). Combining controlled-source seismology and receiver function information to derive 3-D moho topography for italy. *Geophys. J. Int.*, 194(2) :1050–1068.

Spakman, W. and Wortel, R. (2004). A Tomographic View on Western Mediterranean Geodynamics. In *TRANSMED Atlas. Mediterr. Reg. from Crust to Mantle*, pages 31–52. Springer Berlin Heidelberg, Berlin, Heidelberg.

Spetzler, J., Trampert, J., and Snieder, R. (2002). The effect of scattering in surface wave tomography. *Geophys. J. Int.*, 149(3) :755–767.

Stehly, L., Campillo, M., and Shapiro, N. M. (2006). A study of the seismic noise from its long-range correlation properties. *J. Geophys. Res.*, 111(B10) :B10306.

Stehly, L., Fry, B., Campillo, M., Shapiro, N. M., Guilbert, J., Boschi, L., and Giardini, D. (2009). Tomography of the Alpine region from observations of seismic ambient noise. *Geophys. J. Int.*, 178(1) :338–350.

Tape, C. (2009). Seismic tomography of southern California using adjoint methods. *PhD Thesis*.

Tape, C., Liu, Q., Maggi, A., and Tromp, J. (2009). Adjoint Tomography of the Southern California Crust. *Science (80-.).*, 325(5943) :988–992.

Tatham, D., Lloyd, G., Butler, R., and Casey, M. (2008). Amphibole and lower crustal seismic properties. *Earth Planet. Sci. Lett.*, 267(1-2) :118–128.

Tesauro, M., Kaban, M. K., and Cloetingh, S. A. P. L. (2008). EuCRUST-07 : A new reference model for the European crust. *Geophys. Res. Lett.*, 35(5) :L05313.

Thomson, D. J. (1982). Spectrum Estimation and Harmonic Analysis. *Proc. IEEE*.

Thouvenot, F., Paul, A., Sénéchal, G., HIRN, A., and NICOLICH, R. (1990). ECORS-CROP wide-angle reflection seismics : constraints on deep interfaces beneath the Alps. *Mém. Soc. géol. Fr.*, 156 :97–106.

Tian, Y. and Ritzwoller, M. H. (2015). Directionality of ambient noise on the Juan de Fuca plate : implications for source locations of the primary and secondary microseisms. *Geophys. J. Int.*, 201(1) :429–443.

Tibuleac, I. M. and von Seggern, D. (2012). Crust-mantle boundary reflectors in Nevada from ambient seismic noise autocorrelations. *Geophys. J. Int.*, 189(1) :493–500.

Toksoz, M. N. and Lacoss, R. T. (1968). Microseisms : Mode Structure and Sources. *Science (80-.).*, 159(3817) :872–873.

Trinh, P.-T., Brossier, R., Métivier, L., Tavard, L., and Virieux, J. (2019). Efficient time-domain 3D elastic and viscoelastic full-waveform inversion using a spectral-element method on flexible Cartesian-based mesh. *GEOPHYSICS*, 84(1) :R61–R83.

Trinh, P. T., Brossier, R., Métivier, L., Virieux, J., and Wellington, P. (2017a). Bessel smoothing filter for spectral element mesh. *Geophys. J. Int.*, 209(3) :1489–1512.

Trinh, P. T., Brossier, R., Métivier, L., Virieux, J., and Wellington, P. (2017b). Structure-smoothing Bessel filter for finite element mesh : Application on 3D elastic FWI. In *79th EAGE Conf. Exhib. 2017*.

Tromp, J., Luo, Y., Hanasoge, S., and Peter, D. (2010). Noise cross-correlation sensitivity kernels. *Geophys. J. Int.*, 183(2) :791–819.

Tromp, J., Tape, C., and Liu, Q. (2004). Seismic tomography, adjoint methods, time reversal and banana-doughnut kernels. *Geophys. J. Int.*, 160(1) :195–216.

Tsai, V. C. (2009). On establishing the accuracy of noise tomography travel-time measurements in a realistic medium. *Geophys. J. Int.*, 178(3) :1555–1564.

Verbeke, J., Boschi, L., Stehly, L., Kissling, E., and Michelini, A. (2012). High-resolution Rayleigh-wave velocity maps of central Europe from a dense ambient-noise data set. *Geophys. J. Int.*, 188(3) :1173–1187.

Virieux, J. and Operto, S. (2009). An overview of full-waveform inversion in exploration geophysics. *GEOPHYSICS*, 74(6) :WCC1–WCC26.

Waldhauser*, F., Kissling, E., Ansorge, J., and Mueller, S. (1998). Three-dimensional interface modelling with two-dimensional seismic data : the Alpine crust-mantle boundary. *Geophys. J. Int.*, 135(1) :264–278.

Wang, Q.-Y., Brenguier, F., Campillo, M., Lecointre, A., Takeda, T., and Aoki, Y. (2017). Seasonal Crustal Seismic Velocity Changes Throughout Japan. *J. Geophys. Res. Solid Earth*, 122(10) :7987–8002.

Wang, T., Song, X., and Xia, H. H. (2015). Equatorial anisotropy in the inner part of Earth's inner core from autocorrelation of earthquake coda. *Nat. Geosci.*, 8(3) :224–227.

Wapenaar, K. (2004). Retrieving the elastodynamic Green's function of an arbitrary inhomogeneous medium by cross correlation. *Phys. Rev. Lett.*, 93(25) :1–4.

Wapenaar, K., Draganov, D., Snieder, R., Campman, X., and Verdel, A. (2010a). Tutorial on seismic interferometry : Part 1 — Basic principles and applications. *GEOPHYSICS*, 75(5) :75A195–75A209.

Wapenaar, K., Slob, E., Snieder, R., and Curtis, A. (2010b). Tutorial on seismic interferometry : Part 2 — Underlying theory and new advances. *GEOPHYSICS*, 75(5) :75A211–75A227.

Weaver, R., Froment, B., and Campillo, M. (2009). On the correlation of non-isotropically distributed ballistic scalar diffuse waves. *J. Acoust. Soc. Am.*, 126(4) :1817.

Weaver, R. L. and Lobkis, O. I. (2001). Ultrasonics without a Source : Thermal Fluctuation Correlations at MHz Frequencies. *Phys. Rev. Lett.*, 87(13) :134301.

Weaver, R. L. and Lobkis, O. I. (2002). On the emergence of the Green's function in the correlations of a diffuse field : pulse-echo using thermal phonons. *Ultrasonics*, 40(1-8) :435–439.

Wegler, U. and Sens-Schönfelder, C. (2007). Fault zone monitoring with passive image interferometry. *Geophys. J. Int.*, 168(3) :1029–1033.

Yamamura, K., Sano, O., Utada, H., Takei, Y., Nakao, S., and Fukao, Y. (2003). Long-term observation of in situ seismic velocity and attenuation. *J. Geophys. Res. Solid Earth*, 108(B6).

Yang, P., Brossier, R., and Virieux, J. (2016). Wavefield reconstruction by interpolating significantly decimated boundaries. *GEOPHYSICS*, 81(5) :T197–T209.

Yang, Y. and Ritzwoller, M. H. (2008). Characteristics of ambient seismic noise as a source for surface wave tomography. *Geochemistry, Geophys. Geosystems*, 9(2) :Q02008.

Yang, Y., Ritzwoller, M. H., Levshin, A. L., and Shapiro, N. M. (2007). Ambient noise Rayleigh wave tomography across Europe. *Geophys. J. Int.*, 168(1) :259–274.

Yao, H., Beghein, C., and van der Hilst, R. D. (2008). Surface wave array tomography in SE Tibet from ambient seismic noise and two-station analysis - II. Crustal and upper-mantle structure. *Geophys. J. Int.*, 173(1) :205–219.

Yao, H. and van der Hilst, R. D. (2009). Analysis of ambient noise energy distribution and phase velocity bias in ambient noise tomography, with application to SE Tibet. *Geophys. J. Int.*, 179(2) :1113–1132.

Yomogida, K. and Aki, K. (1987). Amplitude and phase data inversions for phase velocity anomalies in the Pacific Ocean basin. *Geophys. J. Int.*, 88(1) :161–204.

Young, M. K., Rawlinson, N., and Bodin, T. (2013). Transdimensional inversion of ambient seismic noise for 3D shear velocity structure of the Tasmanian crust. *GEOPHYSICS*, 78(3) :WB49–WB62.

Yuan, H., French, S., Cupillard, P., and Romanowicz, B. (2014). Lithospheric expression of geological units in central and eastern North America from full waveform tomography. *Earth Planet. Sci. Lett.*, 402 :176–186.

Zhan, Z., Ni, S., Helmberger, D. V., and Clayton, R. W. (2010). Retrieval of Moho-reflected shear wave arrivals from ambient seismic noise. *Geophys. J. Int.*, 182 :408–420.

Zhao, L., Paul, A., Guillot, S., Solarino, S., Malusà, M. G., Zheng, T., Aubert, C., Salimbeni, S., Dumont, T., Schwartz, S., Zhu, R., and Wang, Q. (2015). First seismic evidence for continental subduction beneath the Western Alps. *Geology*, 43(9) :815–818.

Zhao, L., Paul, A., Malusà, M. G., Xu, X., Zheng, T., Solarino, S., Guillot, S., Schwartz, S., Dumont, T., Salimbeni, S., Aubert, C., Pondrelli, S., Wang, Q., and Zhu, R. (2016). Continuity of the Alpine slab unraveled by high-resolution P wave tomography. *J. Geophys. Res. Solid Earth*, 121(12) :8720–8737.

Zhou, Y., Dahlen, F. A., and Nolet, G. (2004). Three-dimensional sensitivity kernels for surface wave observables. *Geophys. J. Int.*, 158(1) :142–168.

Zhu, H., Bozdağ, E., Peter, D., and Tromp, J. (2012). Structure of the European upper mantle revealed by adjoint tomography. *Nat. Geosci.*, 5(7) :493–498.

Zhu, H., Bozdağ, E., and Tromp, J. (2015). Seismic structure of the European upper mantle based on adjoint tomography. *Geophys. J. Int.*, 201(1) :18–52.